

**MAGNETIC RESONANCE IMAGE-BASED NUMERICAL
MODELING OF CEREBROSPINAL FLUID DYNAMICS:
APPLICATION TO FILTRATION AND INTRATHECAL
DRUG DELIVERY**

A Dissertation

Presented in Partial Fulfillment of the Requirements for the

Degree of Doctor of Philosophy

with a

Major in Biological Engineering

in the

College of Graduate Studies

University of Idaho

by

Mohammadreza Khani

Major Professor: Bryn A. Martin, Ph.D.

Committee Members: Tao Xing, Ph.D., Russ Qualls, Ph.D., Ralph Budwig, Ph.D., Brian He, Ph.D.

Department Administrator: Ching-An Peng, Ph.D.

December 2019

Authorization to Submit Dissertation

This dissertation of Mohammadreza Khani, submitted for the degree of Doctor of Philosophy with a Major in Biological Engineering and titled "MAGNETIC RESONANCE IMAGE-BASED NUMERICAL MODELING OF CEREBROSPINAL FLUID DYNAMICS: APPLICATION TO CSF FILTRATION AND INTRATHECAL DRUG DELIVERY" has been reviewed in final form.

Permission, as indicated by the signatures and dates below, is now granted to submit final copies to the College of Graduate Studies for approval.

Major Professor: _____ Date: _____
Bryn A. Martin, Ph.D.

Committee Members: _____ Date: _____
Tao Xing, Ph.D.

_____ Date: _____
Russel Qualls, Ph.D.

_____ Date: _____
Ralph Budwig, Ph.D.

_____ Date: _____
Brian He, Ph.D.

Department Administrator: _____ Date: _____
Ching-An Peng, Ph.D.

Abstract

Cerebrospinal fluid (CSF) plays a vital role in the immunological support, structural protection and metabolic homeostasis of the central nervous system (CNS). The CSF is a promising route with many potentially important roles for CNS therapeutics such as: a) direct delivery of large drug molecules to the CNS tissue that is not possible via blood injection due to the blood brain barrier and b) CSF filtration, termed Neurapheresis therapy, to remove unwanted solutes in CNS diseases such as Alzheimer's disease, meningitis, subarachnoid hemorrhage and leptomeningeal metastasis. While many studies have shown increasing importance of the role of CSF in CNS system homeostasis, there is a need to understand the impact of realistic geometry on CSF flow patterns. An anatomically accurate and validated CFD model will allow testing and optimization of CNS biomedical technologies such as CSF filtration devices. Such a simulator could reduce cost of non-human primate studies and lead to more rapid application of these technologies for clinical use. In this dissertation, CSF dynamics in monkeys and humans was investigated in four stages as following:

First, a magnetic resonance imaging (MRI) protocol was developed and applied to quantify subject-specific CSF space geometry and flow and define the CFD domain and boundary conditions in non-human primates. An algorithm was implemented to reproduce the axial distribution of unsteady CSF flow by non-uniform deformation of the dura surface. Results showed that maximum difference between the MRI measurements and CFD simulation of CSF flow rates was <3.6%. CSF flow along the entire spine was laminar with a peak Reynold's number of ~150 and average Womersley number of ~5.4. Maximum CSF flow rate was present at the C4-C5 vertebral level. Deformation of the dura ranged up to a maximum of 134 μm . Geometric analysis indicated that total spinal CSF space volume was ~8.7 ml. Average hydraulic diameter, wetted perimeter and SAS area was 2.9 mm, 37.3 mm and 27.24 mm², respectively. CSF pulse wave velocity along the spine was quantified to be 1.2 m/s.

Second, a geometric and hydrodynamic characterization of CSF in eight cynomolgus monkeys (*Macaca fascicularis*) was presented at baseline and two-week follow-up. Results showed that CSF flow along the entire spine was laminar with a Reynolds number ranging up to 80 and average Womersley number ranging from 4.1-7.7. Maximum CSF flow rate occurred ~25 mm caudal to the foramen magnum. Peak CSF flow rate ranged from 0.3-0.6 ml/s at the C3-C4 level. Geometric analysis indicated that average intrathecal CSF volume below the foramen magnum was 7.4 ml. The average surface area of the spinal cord and dura was 44.7 and 66.7 cm² respectively. Subarachnoid space cross-sectional area and hydraulic diameter ranged from 7-75 mm² and 2-3.7 mm, respectively. Stroke volume had the greatest value of 0.14 ml at an axial location corresponding to C3-C4.

The third objective of this dissertation was to investigate the impact of spinal cord nerve roots (NR) on CSF dynamics. A subject-specific computational fluid dynamics (CFD) model of the complete spinal subarachnoid space (SSS) with and without anatomically realistic NR and non-uniform moving dura wall deformation was constructed. This CFD model allowed detailed investigation of the impact of NR on CSF velocities that is not possible in vivo using MRI or other non-invasive imaging methods. Results showed that NR altered CSF dynamics in terms of velocity field, steady-streaming and vortical structures. Vortices occurred in the cervical spine around NR during CSF flow reversal. The magnitude of steady-streaming CSF flow increased with NR, in particular within the cervical spine. This increase was located axially upstream and downstream of NR due to the interface of adjacent vortices that formed around NR. Average value for steady streaming velocity was 0.11 ± 0.12 and 0.05 ± 0.04 mm/s (mean \pm stdev) for the model with versus without NR (120% greater with NR). The region of greatest difference in steady streaming velocity values was the cervical spine that had up to 5X larger value of steady streaming velocity with NR compared to without.

In fourth step, we formulated a subject-specific computational fluid dynamics (CFD) model to parametrically investigate the impact of a novel dual-lumen catheter-based CSF filtration system, the Neurapheresis therapy system (Minnetronix Neuro, Inc., St. Paul, MN), on intrathecal CSF dynamics. The operating principle of this system is to remove CSF from one location along the spine (aspiration port), externally filter the CSF routing the retentate to a waste bag, and return permeate (uncontaminated CSF) to another location along the spine (return port). The CFD model allowed parametric simulation of how the Neurapheresis system impacts intrathecal CSF velocities and steady-steady streaming under various Neurapheresis flow settings ranging from 0.5 to 2.0 ml/min and with a constant retentate removal rate of 0.2 ml/min. simulation of the Neurapheresis system were compared to a lumbar drain simulation with a typical CSF removal rate setting of 0.2 ml/min. Results showed that the Neurapheresis system at a maximum flow of 2.0 ml/min increased average steady-streaming CSF velocity 2X in comparison to lumbar drain (0.190 ± 0.133 versus 0.093 ± 0.107 mm/s, respectively). This affect was localized to the region within the Neurapheresis flow-loop. The mean velocities introduced by the flow-loop were relatively small in comparison to normal cardiac-induced CSF velocities.

Finally, a subject-specific multiphase CFD model was constructed based on high-resolution anatomic MRI. The dual-lumen Neurapheresis catheter geometry was added to the model within the posterior spinal subarachnoid space (SAS). Neurapheresis flow aspiration and return rate was 2.0 and 1.8 (mL/min), versus 0.2 (mL/min) drainage for lumbar drain. An in vitro CSF model was constructed with an identical fluid domain geometry. A detailed comparison of numerical and in vitro results was performed by the Bland-Altman correlation analysis. Neurapheresis therapy was found to have a larger

impact on steady streaming in comparison to lumbar drain. Steady-streaming in the cranial SAS was ~50X smaller than in the spinal SAS for both cases. Results showed that 85% of the spinal SAS was cleared within one hour with the Neurapheresis flow loop in comparison to 50% clearance after 24-hour with lumbar drain. Clearance was maximized between the aspiration and the return ports with the Neurapheresis therapy. However, intracranial clearance for the Neurapheresis therapy was similar to lumbar drain (66% clearance). Quantitative comparison of Neurapheresis therapy results showed that the speed of clearance match with less than 4% error after 24-hour (50% CFD vs 46% in vitro).

Acknowledgements

I must first acknowledge with sincere gratitude the guiding mind of Dr. Bryn Martin whose knowledge, curiosity and perseverance led to the development and completion of this research. His knowledge of the cerebrospinal fluid and computational fluid dynamics (CFD) gave me the skills to produce the valuable results in this field and writing papers. Directing and guiding through the process of completion of this important achievement in my life, he was able to help facilitate strides through the process.

I also recognize the help and counsel I have received from Dr. Tao Xing, Dr. Keith Sharp, Dr. Shivanand Lad, Aaron McCabe, Laura Zitella Verbick, Haiming Wu who with great savvy and competence are able to see outside the box, continuing the evolution and applicability of contemporary and future CFD.

Others that were involved in the work and deserve recognition include Lucas Sass, Gabryel Conley Natividad, Goutham Kumar Reddy Burla, Austin Sass, Braden Lawrence and also thank many others including friends and family unnamed here.

Dedication

This dissertation is dedicated to my mother, who first taught me the value of education and critical thought. I also dedicate this work to my sisters for their encouragement, moral support, personal attention and care.

Table of Contents

Authorization to Submit Dissertation	ii
Abstract	iii
Acknowledgements	vi
Dedication	vii
Table of Contents	viii
List of Tables	xi
List of Figures	xii
Statement of Contribution	xvii
Chapter 1: Background.....	1
Motivation for Cerebrospinal Fluid Research	1
Biological Function of CSF.....	2
CSF Circulation.....	2
CSF Pulsation	4
CSF Filtration	5
Intrathecal Drug Delivery	5
Magnetic Resonance Imaging	6
Computational Fluid Dynamics.....	8
Chapter 2: Research Objectives.....	12
Aim 1: CFD Simulation of CSF Dynamics in Non-human Primates	12
Aim 2: Characterization of CSF Dynamics and Geometry in Non-human Primates	12
Aim 3: CFD Simulation of CSF Dynamics in Human	12
Aim 4: Numerical Investigation of Filtration System Impact on CSF Dynamics	13
Aim 5: CFD simulation of Intrathecal Drug Delivery.....	13
Project Sustainability.....	13
Deliverables.....	14
Wider Impact.....	15

Future Work	15
Chapter 3: Non-uniform Moving Boundary Method for Computational Fluid Dynamics Simulation of Intrathecal Cerebrospinal Flow Distribution in a Cynomolgus Monkey.....	18
Abstract	18
Introduction	18
Methods and Materials	19
Results	31
Discussion	39
Conclusion.....	43
Chapter 4: Characterization of intrathecal cerebrospinal fluid geometry and dynamics in cynomolgus monkeys (macaca fascicularis) by magnetic resonance imaging	45
Abstract	45
Introduction	45
Methods and Materials	47
Results	54
Discussion	64
Conclusion.....	68
Chapter 5: Anthropomorphic Model of Intrathecal Cerebrospinal Fluid Dynamics within the Spinal Subarachnoid Space: Spinal Cord Nerve Roots Increase Steady-Streaming	69
Abstract	69
Introduction	69
Methods and Materials	72
Results	83
Discussion	93
Conclusion.....	97
Chapter 6: Impact of Neurapheresis system on intrathecal cerebrospinal fluid dynamics: a computational fluid dynamics study.....	98
Abstract	98

Introduction	98
Methods and Materials	102
Results	107
Discussion	112
Conclusion.....	116
Chapter 7: Conclusion.....	117
References	119

List of Tables

Table 3.1. Anatomic and CSF flow MRI scan protocol parameters.....	22
Table 3.2. Verification of results by numerical independence studies— values show the maximum relative error for velocity in the z-direction for the three axial planes analyzed (Figure 4).....	28
Table 3.3. Reference chart for vertebral disk location with respect to axial distance from the foramen magnum.....	32
Table 3.4. Summary of hydrodynamic and geometric results from the numerical simulation. Average, maximum and minimum values for each parameter are computed based on the full SAS length.....	33
Table 3.5. Comparison of hydrodynamic CFD peak values with in vivo PCMRI measurements.	35
Table 4.1. Anatomic (T2-VISTA) and CSF flow (phase-contrast MRI) scan protocol parameters used for imaging cynomolgus monkeys.	48
Table 4.2. Reference chart for vertebral disk location with respect to axial distance from the foramen magnum in cynomolgus monkeys.	52
Table 4.3. Summary of geometric and hydrodynamic results. Mean values correspond to the average along the entire spine for all 16 NHPs (except for total surface area, volume, and PWV). Local maximum and minimum values are computed based the average for all 16 NHPs (solid lines in Fig 6).	55
Table 5.1. Summary of previous spinal CSF dynamics numerical studies with key information on the numerical method, anatomic / physiologic feature investigated and the feature impact on CSF dynamics.....	71
Table 5.2. Numerical sensitivity studies — values show the maximum relative error for velocity in the z-direction for the three axial planes analyzed (Figure 2).	80
Table 5.3. Verification of results by factor of safety method — values show the global error for velocity in the z-direction for the three axial planes analyzed (Figure 2).	81
Table 6.1. Summary of clinical studies focused on clearance of blood from the CSF post-subarachnoid hemorrhage.....	100
Table 6.2. Average steady-streaming velocity magnitude, $U_{ss}(z)$, and non-dimensional fraction of flow rate amplitude, $Q_{ss}(z)$, for the simulations analyzed.....	105
Table 6.3. Specification of flow rates at the Neurapheresis catheter aspiration and return port.	110

List of Figures

Figure 1.1. 3D representation of the CSF system surrounding the brain and CNS.(Figure from [35])	3
Figure 1.2. Intracranial CSF 3D model and distinct compartments (Figure courtesy of Gabryel Conley Natividad)	4
Figure 1.3. Visualization of drug delivery to the brain and CNS in a non-human primate using fused CT and PET imaging (Figure from [40]).	6
Figure 3.1. (a) T2-weighted MR image of the entire spine for the cynomolgus monkey analyzed. Axial location and slice orientation (lines) of the phase-contrast MRI scans obtained in the study. Slice axial distance from foramen magnum indicated by dotted lines (b) The CSF flow rate based on in vivo PCMRI measurement at FM, C2-C3, T4-T5, T10-T11, and L2-L3. (c) sagittal view of the SAS segmentation based on T2-weighted MRI.	21
Figure 3.2. (a) Three-dimensional CFD model of the SAS. (b) Zoom of the upper cervical spine mesh showing the model inlet (top). (c) Volumetric mesh visualization in the axial and sagittal planes within the cervical SAS.	23
Figure 3.3. (a) Dynamic mesh motion flow chart used for the CFD simulation. Recursive arrows indicate repetition of steps. (b) A 2D axial cross-section with relevant variables and key equation used to compute radial deformation of the dura.	26
Figure 3.4. (a) 3D geometry of the independence study and axial plane positions (b) line location along each plane (c) Peak systolic w-velocity component visualized along each line for the three grids (coarse, medium and fine).	29
Figure 3.5. Hydrodynamic parameter distribution for the dura, spinal cord and subarachnoid space computed along the spine for a cynomolgus monkey in terms of: (a) perimeter, (b) cross-sectional area, (c) hydraulic diameter, (d) Reynold's number, Re and Womersley number, α . Comparison of CFD simulation (continuous line) and PCMRI measurements (dots) in terms of: (e) peak systolic and diastolic CSF velocity and (f) mean CSF velocity at peak systolic and diastolic flow.	34
Figure 3.6. (a) CSF flow waveforms measured by PCMRI at five axial locations along the spine. Dots indicate experimental data and lines denote CFD results. Note: negative, or peak systolic, CSF flow is in the caudal direction. (b) Spatial-temporal distribution of the interpolated CSF flow rate along the spine. Dotted line indicates peak CSF flow rate at each axial level used to compute CSF pulse wave velocity (PWV). (c) Radial displacement of the dura surface at 100 ms intervals over the CSF flow cycle. (d) Spatial-temporal distribution of the dura radial displacement along the spine. Dotted line indicates the three locations along the spine with zero radial motion of the dura.	36
Figure 3.7. Peak-systolic thru-plane CSF velocity profiles simulated by CFD and measured by PCMRI for a cynomolgus monkey. (a) Overall view of the CFD model and slice locations. Note:	

different velocity scales are used at each slice location. (b) CSF velocity profiles at each slice location. (c) PCMRI visualization of CSF velocity profiles. (d) PCMRI gray scale images used to compute CSF flow waveforms. \uparrow symbols highlight nearby regions with PCMRI signal that are not within the CSF space ROI (epidural venous flow at L2-L3, and vertebral artery flow at the FM)..... 38

Figure 4.1. Manual segmentation of the spinal subarachnoid space using a T2-weighted MR image for a cynomolgus monkey analyzed in this study. (A) Visualization of SAS area manually selected around the spinal cord at multiple axial levels. (B) Mid-sagittal high-resolution T2-weighted MRI. (C) Sagittal visualization of segmented SAS around the spinal cord. (D) 3D visualization of entire SAS geometry. The same methods were applied to all MR images obtained for all NHPs..... 49

Figure 4.2. Axial PC-MRI and CSF velocity profiles at corresponding vertebral levels for a cynomolgus monkey in this study. (A) PC-MRI axial cross-sections for a given case at each respective vertebral level. (B) T2-weighted MR image of a cynomolgus monkey in the study with corresponding PC-MRI axial locations and slice orientation (solid green lines) at FM, C2-C3, C5-C6, T4-T5, T11-T12, and L3-L4. (C) 3D visualization of peak systolic CSF velocity profiles based on in vivo PC-MRI measurements at each vertebral level. 51

Figure 4.3. Geometric parameters distribution computed along the spine for cynomolgus monkeys. (A) Area of dura, (B) Area of spinal cord, (C) Area of subarachnoid space, (D) Perimeter of dura, (B) Perimeter of spinal cord, (C) Perimeter of subarachnoid space. Mean value for all 16 NHPs corresponds to the solid line. Dotted lines correspond to ± 1 standard deviation for all 16 NHPs analyzed..... 56

Figure 4.4. CSF flow waveforms for all 16 cases measured by PC-MRI at six axial locations along the spine. Error bars correspond to ± 1 standard deviation of flow rates obtained for all 16 NHPs. Note: negative, or peak systolic, CSF flow is in the caudal direction. 58

Figure 4.5. Mean CSF flow waveforms and Spatial-temporal distribution of CSF flow rate (A) Mean CSF flow waveforms for all 16 cases measured by PC-MRI at six axial locations along the spine. Note: negative, or peak systolic, CSF flow is in the caudal direction. (B) Spatial-temporal distribution of the interpolated CSF flow rate along the spine. Dotted line indicates peak CSF flow rate at each axial level used to compute CSF pulse wave velocity (PWV). 59

Figure 4.6. Hydrodynamic parameter distribution computed along the spine for cynomolgus monkeys. (A) Reynolds number, Re , (B) Flow rate amplitude, Q_a , (C) Stroke Volume, SV , (D) left axis, Hydraulic diameter, D_h , right axis, Womersley number, α , (E) mean peak systolic, \bar{U}_{sys} ,

and diastolic, \bar{U}_{dia} , CSF velocity. Mean value for all 16 NHPs corresponds to the solid line. Dotted lines correspond to ± 1 standard deviation for all 16 NHPs analyzed.	60
Figure 4.7. Scatter plots of geometric parameters. (A) Area of dura, (B) Area of spinal cord, (C) Area of subarachnoid space, (D) Perimeter of dura, (E) Perimeter of spinal cord, (F) Perimeter of subarachnoid space. Dot color represents distance from the FM (blue is near the FM and red is near the SAS termination).	62
Figure 4.8. Scatter plots of hydrodynamic parameter distribution computed along the spine. (A) Reynolds number, Re , (B) flow rate amplitude, Q_a , (C) stroke volume, SV , (D) hydraulic diameter, D_h , (E) Womersley number, α , and, (F) mean peak systolic, \bar{U}_{sys} , and diastolic, \bar{U}_{dia} , CSF velocity. Dot color represents distance from the FM (blue is near the FM and red is near the SAS termination).	63
Figure 5.1. Summary of numerical modeling approach based on subject specific MRI measurements. (a) T2-weighted MR image of the entire spine for the human analyzed (open-source 3D geometry from Sass et al.[150]). Axial location and slice orientation (lines) of the phase-contrast MRI scans obtained in the study. Slice axial distance indicated by dotted lines (b) The CSF flow rate based on in vivo PCMRI measurement at C2-C3, C7-T1, T10-T11. (c) Three-dimensional CFD model of the SSS. (d) Volumetric and surface mesh visualization with zoom of the upper cervical spine (top).	74
Figure 5.2. Numerical sensitivity study for velocity and cyclic mean velocity results. (a) 3D geometry of the sensitivity study and axial plane positions, (b) line location along each plane, (c) simulated peak systolic z-velocity component along each line for the four grids (coarse, medium, fine and X-fine), and (d) simulated cross-sectional mean velocity, U_{z-mean} , along each line for the four grids.	77
Figure 5.3. Comparison of numerical model axial flow rate distribution with subject specific PCMRI measurements. (a) CSF flow waveforms measured by PCMRI at three axial locations along the spine. Dots indicate experimental data and lines denote CFD results. Note: negative, or peak systolic, CSF flow is in the caudal direction. (b) Spatial-temporal distribution of the average dura radial displacement along the spine.	84
Figure 5.4. Hydrodynamic parameter distribution computed along the spine in terms of: (a) peak CSF velocity, (b) cross-sectional area (c) hydraulic diameter and Womersley number, α , (d) Reynolds number, for internal flow within a tube, Re , (e) Stokes-Reynolds number based on Stokes-layer thickness, Re_δ , (f) Reynolds number for external flow over a NR, Re_{NR}	85

Figure 5.5. Thru-plane CSF velocity profiles simulated by CFD at T=90 ms for three different views: (a) coronal, (b) sagittal and (c) axial at six slice locations. Note: peak systolic timing was obtained for CSF flow at C2-C3. The axial distribution of peak CSF velocities over the entire cardiac cycle is shown in Figure 4a. Also, to help visualize the entire spine, z-scaling of the geometry is set at 0.5 with respect to x and y-dimensions. Thus, spine curvature appears greater than without scaling. 87

Figure 5.6. Vortices form around spinal cord NR in the cervical spine at time-points corresponding to CSF flow reversal. (a) CSF flow rate at C2-C3 section, (b) velocity contour for C2-C3 section and (c) streamlines showing vortices that form around NR pairs (FM-C1, C1-C2, C2-C3 and C3-C4) at four different time steps. The interfaces of these vortices are located upstream and downstream of NR pairs. Note: velocity scales are different for each time point. 88

Figure 5.7. Presence of spinal cord NR result in a complex distribution of cyclic mean CSF velocities within the SSS. Cyclic mean CSF velocity profiles, U_{z-mean} , simulated by CFD for three different views: (a) coronal, (b) sagittal, (c) axial at six slice locations. Note: Cyclic mean CSF velocity is calculated based on one complete CSF flow cycle..... 90

Figure 5.8. Cyclic mean CSF velocities decrease and change profiles without NR present in the numerical model. CSF cyclic mean velocity profiles, U_{z-mean} , for the case without spinal cord nerve roots at three different views: (a) coronal, (b) sagittal, (c) axial at six slice locations. Compare profiles to Figure 7 to see impact of NR. 91

Figure 5.9. Steady-streaming velocity magnitude, U_{ss} , and non-dimensional fraction of flow rate amplitude, Q_{ss} , increases with NR compared to without NR. Dotted lines indicate that maximum U_{ss} occurs upstream / downstream of NRs in the cervical spine at the interface of adjacent vortices (see vortices in Figure 6c)..... 92

Figure 6.1. Schematic of the neurapheresis filtration system. CSF is removed from the lumbar spine at the aspiration port of a dual lumen intrathecal catheter. Blood is then removed from the CSF by the external filtration system. The filtered fluid is then returned to the CSF system in the upper thoracic spine via the dual lumen catheter. Note: the flow rate of fluid returned to the system is slightly less than that aspirated due to the loss of volume removed by the filtration system. The loss in fluid is compensated for by production of CSF within the ventricles. 101

Figure 6.2. (a) overview of three-dimensional CFD model of the subarachnoid space with inserted Neurapheresis catheter. (a1–a4) Details of computational meshes for the Neurapheresis catheter: (a1) Magnified view of the return port with arrows indicating flow direction. (a2) Magnified view of the surface mesh near the return port catheter tip. (a3) Magnified view of the aspiration port with arrows indicating flow direction. (a4) Magnified view of the surface mesh near the aspiration port. (b) Volumetric and surface mesh visualization with zoom of the upper cervical spine. (c) Subject-specific

CSF flow rates imposed by the computational model based on in vivo phase-contrast MRI measurements obtained at C2-C3, C7-T1, and T10-T11 vertebral levels.	102
Figure 6.3. (a) Reynolds number distribution computed along the spine for the Maximum Flow simulation. (b) Visualization of sagittal velocity magnitude profiles simulated by CFD at 0.06s time-point (Figure 2c). (b1) Magnified coronal view of the return port. (b2) Magnified transverse view of the CSF flow field near the return port showing diffusivity of the returned flow near the first hole (b3) Magnified view of the aspiration port. (b4) Magnified transverse view of the CSF flow field near the aspiration port. Note: To help visualize the entire spine, z-scaling of the geometry is set at 0.5 with respect to x and y-dimensions. Thus, spine curvature appears greater than without scaling.	108
Figure 6.4. Visualization of mid-sagittal steady-streaming CSF velocity profiles for all cases analyzed (Table 2). Steady-streaming CSF velocities, U_{z-mean} , increase with Neurapheresis therapy (Maximum Flow, Low Flow, Reverse Flow, and Dynamic Mesh Off) compared to lumbar drain (Lumbar Drain) and with Neurapheresis therapy off (No Flow). Placement of return and the aspiration ports shown with dotted lines for reference. Note: To help visualize the entire spine, z-scaling of the geometry is set at 0.5 with respect to x and y-dimensions. Thus, spine curvature appears greater than without scaling.	109
Figure 6.5. (a) Steady-streaming velocity magnitude, U_{ss} , and (b) non-dimensional fraction of flow rate amplitude, Q_{ss} , increases with Neurapheresis Therapy compared to lumbar drain only between the return and the aspiration ports. Dotted lines indicate that maximum U_{ss} occurs close to the aspiration and the return ports and at the cervical spine near the intersection of spinal cord nerve roots into the dura.	111

Statement of Contribution

Bryn Martin conceived of the presented idea and secured research funding for the work. Mohammadreza Khani, Tao Xing and Bryn Martin developed the theory. Mohammadreza Khani performed the numerical simulations. Mohammadreza Khani completed the data analysis and visualization. Mohammadreza Khani and Lucas Sass verified the computational methods with in vitro model experiments. All in vitro studies were performed by Lucas Sass. Mohammadreza Khani drafted manuscripts and figures. Bryn Martin supervised the project and was in charge of overall project direction and planning. Tao Xing advised with numerical model verification. Keith Sharp contributed to theoretical interpretation of results. All other authors provided critical feedback and commented on the manuscript.

Authors:

Mohammadreza Khani: Department of Biological Engineering, University of Idaho, Moscow, ID, USA

Bryn A. Martin: Department of Biological Engineering, University of Idaho, Moscow, ID, USA

Lucas R. Sass: Department of Biological Engineering, University of Idaho, Moscow, ID, USA

Tao Xing: Department of Mechanical Engineering, University of Idaho, Moscow, ID, USA

Michael Keith Sharp: Department of Mechanical Engineering, University of Louisville, Louisville, KY, USA

Aaron R. McCabe: Minnetronix Neuro, Inc., St. Paul, MN, USA

Laura M Zitella Verbick: Minnetronix Neuro, Inc., St. Paul, MN, USA

Shivanand P. Lad: Department of Neurosurgery, Duke University School of Medicine, Durham, NC, USA

Olivier Balédent: Bioflow Image, Amiens Cedex 1, France

Christina Gibbs: Department of Mechanical Engineering, University of Idaho, Moscow ID, USA

John N Oshinski: Department of Radiology, Emory University, Atlanta, GA, USA

Gregory R Stewart: Alchemy Neuroscience, Hanover, MA, USA

Jillynne R Zeller: Northern Biomedical Research, Spring Lake, MI, USA

Joshua J Pluid: Department of Mechanical Engineering, University of Idaho, Moscow, ID, USA

Gabryel Connely Natividad: Department of Biological Engineering, University of Idaho, Moscow ID, USA

Chapter 1: Background

Motivation for Cerebrospinal Fluid Research

Cerebrospinal fluid (CSF) acts as an immunological support and protecting the structures of the central nervous system (CNS). CSF has many potential roles for CNS therapeutics such as: a) direct delivery of large drug molecules to the CNS tissue that is not possible via blood injection due to the blood brain barrier, b) CSF filtration, termed neuropheresis¹ therapy, to remove unwanted toxins in diseases such as meningitis. c) CSF cooling, termed CSF hypothermia, to slow down traumatic brain and spinal cord (SC) injury following severe accidents.

CSF-based brain therapeutics are gaining interest because they allow direct pharmaceutical targeting of the CNS that can help minimize some side effects associated with conventional oral and intravenous based pharmacotherapies and allows delivery of larger molecule sizes to the CNS that may not normally be able to cross the blood-brain-barrier. A detailed understanding of CSF dynamics could improve treatment of CSF-related CNS diseases and lead to novel CSF-based therapeutics. The importance of CSF dynamics has been investigated in several CNS diseases that include Alzheimer's disease [1, 2], syringomyelia [3, 4], Chiari malformation [5, 6], astronaut vision impairment due to space flight [7] and hydrocephalus [8]. CSF-based therapeutics are presently under development for brain hypothermia [9], CSF filtration [10-13] and control of intracranial CSF pressure oscillations [14].

The efficacy of many of these treatments depends, in part, on transport within the spinal subarachnoid space (SSS). Among the least studied factors is the effect of structures within the SSS on flow and transport, yet the structures appear to strongly affect transport. For example, Stockman found that simplified nerve roots (NR) increased longitudinal transport by five to ten times compared the same channel without structure [15, 16]. Tangen et al. found that simplified microstructure increased vorticity and rostral transport of intrathecal drugs [17] and Tangen et al. noted mixing of subarachnoid hemorrhage around NR [18, 19].

While many studies have shown increasing importance of the role of CSF in CNS system homeostasis, there is a paucity of information on CSF biofluid mechanics. This section presents a brief description of CSF functions in the CNS and the physiological aspects of its pulsation and circulation throughout the cranial and spinal SSS.

¹ Trademark of Minnetronix, Inc.

Biological Function of CSF

CSF plays significant roles in CNS like functional support for the brain and performs as a mechanical damper during high impacts on the head. An average weight for the brain is about 1.5 kg for a healthy adult human but it decreases down to ~50 gr when it is floating in the CSF [20]. CSF also controls the intracranial pressure (ICP) if venous outflow obstruction happened based on any small changes in the brain volume due to hemorrhage. Hemorrhage impacts the intracranial CSF volume to keep the ICP in the standard range.

Another significant biological function of the CSF is removing the toxic products from the CNS and delivering nutrients to the neural and glial cells because of the oscillatory motion [21]. CSF circulation also assists sinking of neurotoxic waste and washing out the brain [22, 23]. The CSF system is acting like a pathway to wash out the neurotoxic waste products from the CNS that can cause Alzheimer's disease progression [24].

CSF Circulation

The entire CSF space volume is about 250-400 ml in a healthy human [25]. CSF system divided in to three connected compartments: 1- the cranial subarachnoid space 2- the spinal subarachnoid space and 3- ventricular system (**Figure 1**). The ventricular system includes two lateral, third and fourth ventricles (**Figure 2**). The CSF production rate in humans is estimated to be approximately 500 cc per day (10 ml/hr) [26].

The main source of CSF production is in ventricles by the choroid plexus. CSF flows along ventricles, cisterns and the subarachnoid space, then it will be reabsorbed at the arachnoid granulations of the superior sagittal sinus [27-29]. CSF is produced by the epithelial cells of the choroid plexus inside the ventricles. It flows from the lateral ventricles through the foramen of Munro, to the third ventricle and then to the aqueduct of Sylvius into the fourth ventricle. It flows through the median foramen of Magendie and the two lateral apertures of Luschka to exit the ventricles. After that, CSF enters the cisterns surrounding the cerebellum in the inferior cranial subarachnoid space and flows superiorly and inferiorly to the cranial and spinal SSS. CSF production and absorption can be different for other species. For example, sheep are thought to have alternative CSF outflow pathways located at the cribriform plate and dural sheaths in the spine.

An MRI study by Yamada et al. [30] showed that CSF moves from the sites of production to sites of absorption as a bidirectional flow between lateral and third ventricles. Milhorat et al. [31-33] showed there is no change in CSF formation rate and the chemical composition after choroid

plexectomy (removal) in animal. New findings revealed that CSF is constantly produced and absorbed throughout the whole CSF system. CSF volume is regulated by the hydrostatic and osmotic forces between CSF and these tissues. The CNS capillaries are the main spots for CSF reabsorption, due to the large surface area. The arachnoid granulations and paraneural sheaths of the spinal nerves are accessory pathways for CSF absorption [34].

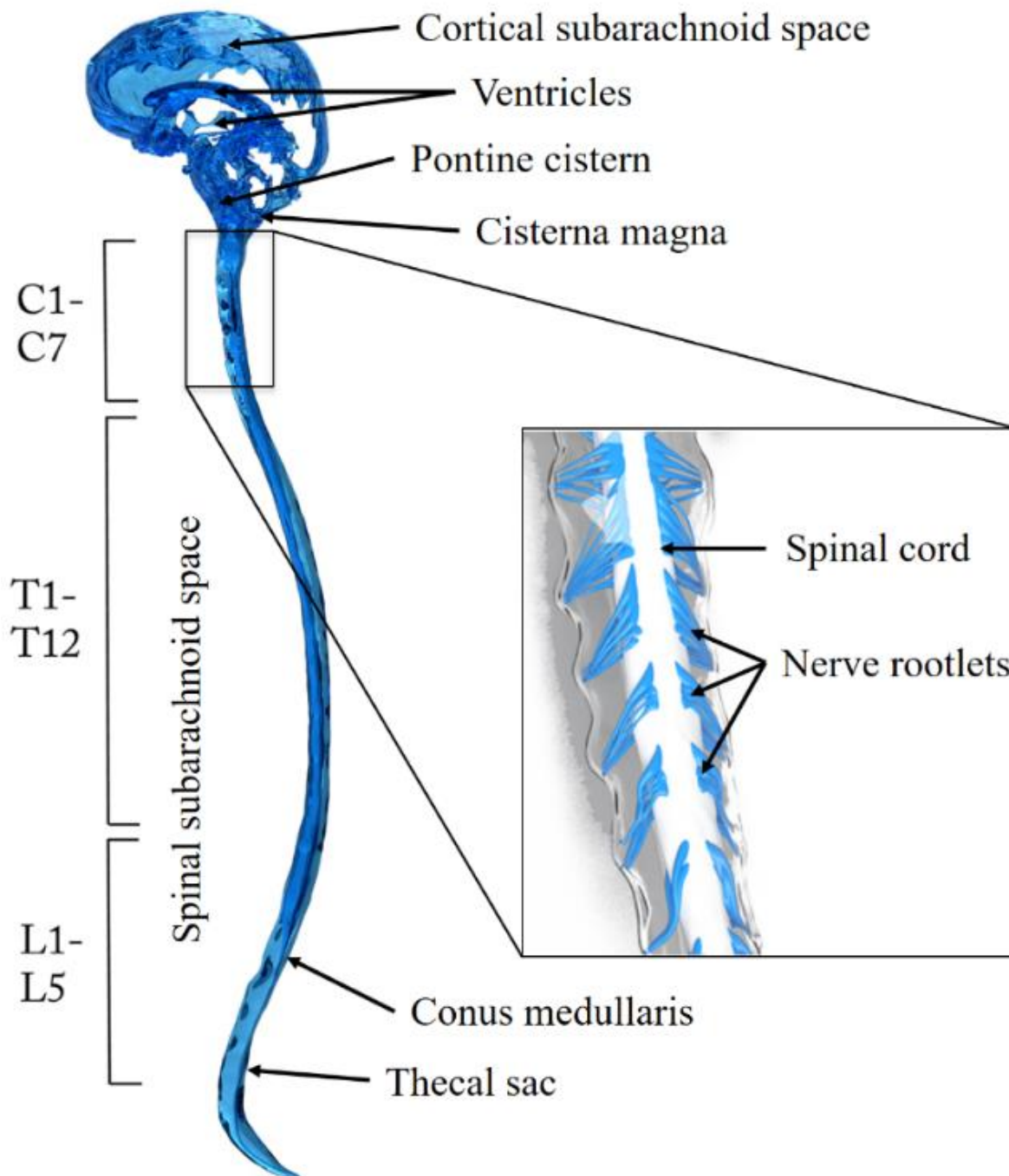


Figure 1.1. 3D representation of the CSF system surrounding the brain and CNS.(Figure from [35])

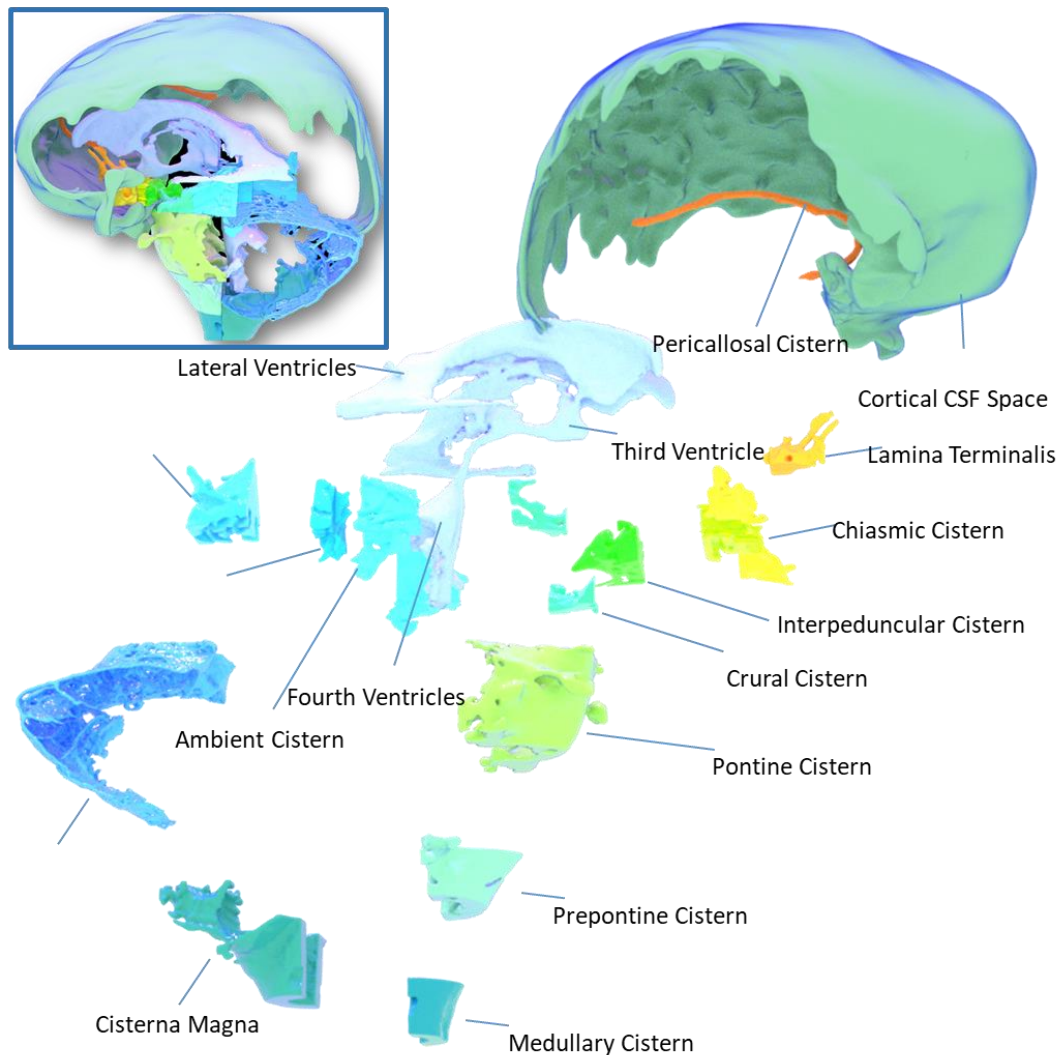


Figure 1.2. Intracranial CSF 3D model and distinct compartments (Figure courtesy of Gabryel Conley Natividad)

CSF Pulsation

The main reason for CSF pulsation is due to the changes in the brain volume and cerebral blood with each heartbeat. This is resulting from the phase changes between the inflow of the arterial blood and outflow of the venous blood from the cranium [36-38]. These changes in the brain volume is identical to the CSF flow quantity that flows between cranial and spinal subarachnoid space (~1-2 ml/Cardiac cycle). Thus, any small changes in the cranial blood volume will affect the CSF flow pulsation.

Respiration is the second driving factor for CSF pulsation. This effect on the CSF pulsation was first shown by Williams et al. [39] using invasive monometer recordings. The effect of deep inhalation/exhalation on the CSF pulsation was found to have a greater effect on the CSF pulsation rather than cardiac related pulsations. Recently, respiration effect was measured by real-time phase-contrast MRI.

CSF Filtration

CSF Filtration Therapeutics is gaining interest since this method allows direct removal of toxic metabolites and waste products produced by the CNS when in various disease states. These substances include blood accumulation after hemorrhage, cancer cells present in the CSF in leptomeningeal cancer, tau protein in Alzheimer's disease and inflammatory cytokines in multiple sclerosis and spinal cord injury². Researchers have conjectured that removal of these toxins could improve patient prognosis.

While CSF filtration therapeutics is gaining interest, an experimental or theoretical platform is lacking to understand the fluid mechanics involved in catheter systems for CSF filtration. At present, CSF filtration procedures are based on empirical observations and lack guidelines for best practice based on the physics.

Intrathecal Drug Delivery

Another focus of this thesis work is intrathecal drug delivery, or delivery of drugs into the CSF by a catheter or needle inserted in the spinal SAS. Herein, a brief review is provided on this therapy. CSF-based brain therapeutics are rapidly gaining interest because they allow direct pharmaceutical targeting of the CNS that can help minimize some side effects associated with conventional oral and intravenous based pharmacotherapies and allows delivery of larger molecule sizes to the CNS that may not normally be able to cross the blood-brain-barrier (**Figure 3**). The delivery of therapeutic agents to the CNS tissue by the CSF is dependent on the following four stages: (1) pulsation-dependent mixing of the CSF, (2) arterial pulsation assisted transport along the perivascular spaces, (3) absorption from the perivascular space to the CNS tissue and (4) extracellular transport and uptake into the neurons and along axons [40]. Each of these aspects must be understood to optimize CSF-based therapeutics.

CSF dynamics plays a critical role by limiting the overall medication spread over the neural tissue. If the medication does not spread within the CSF to be in direct contact with the region of the

² See US Patent Application US 20160051801 A1

brain/CNS needing the medication then steps (2) through (4) will have little relevance. In fact, at present CSF-based brain therapeutic procedures are likely based on empirical observations [41, 42] and lack guidelines for best practice based on the physics of CSF dynamics and geometry. The overarching goal of the proposed study is to develop and validate a numerical simulator for brain therapeutic development.

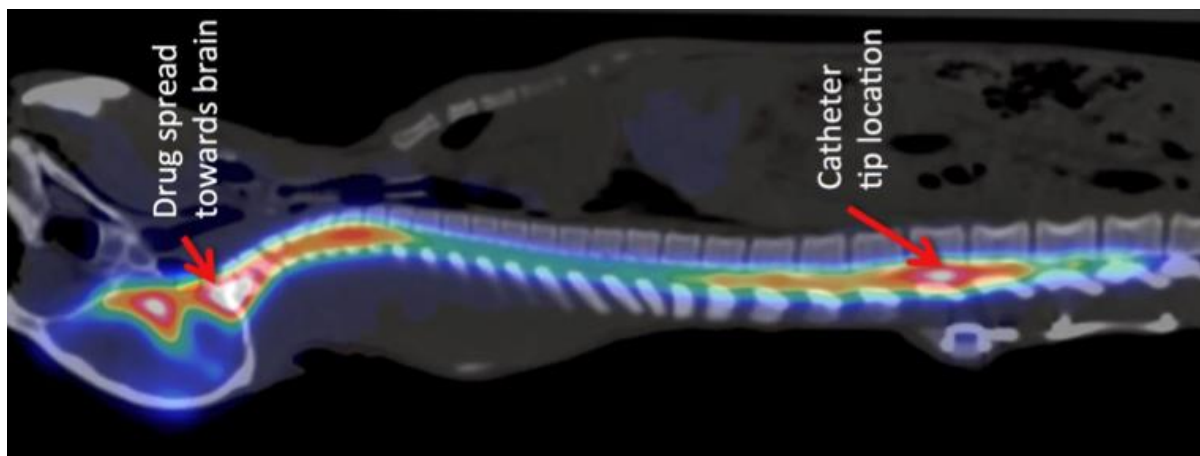


Figure 1.3. Visualization of drug delivery to the brain and CNS in a non-human primate using fused CT and PET imaging (Figure from [40]).

Magnetic Resonance Imaging

Magnetic resonance imaging (MRI) is a medical imaging technique used to form images of the anatomical and the physiological processes of the body. MRI scanners use strong magnetic fields and radio waves to generate pictures of the organs in the body. MRI is extensively used in hospitals for medical diagnosis, staging of disease and follow-up without exposing the body to radiation.

Mechanism

Certain atomic nuclei are able to absorb and emit radio frequency energy when they are in a magnetic field. In research MRI, atoms of hydrogen are most often used to produce a detectable radio-frequency signal that is received by probes close to the target anatomy. Hydrogen are abundant in biological organs, mainly in water and fat. Most MRI scans basically map the site of water and fat in the body. Pulses of radio waves stimulate the nuclear spin energy transition. Then magnetic field gradients localize the signal in space. Different contrasts are generated between tissues due to the relaxation properties of the hydrogen atoms. MRI requires a strong and uniform magnetic field.

Anatomical MRI

Anatomical MRI is used to study the shape, volume and integrity of the CSF system. Some of the applications for structural MRI include studying CSF geometry changes in neurological disorder disease. MRI of anatomical structures do not require contrast agents as the varying properties of the tissues provide natural contrasts. MRI is one of the greatest tool for the anatomy of central nervous system. It offers a perfect visualization of the brainstem and the cerebellum. MRI provides a fine contrast between grey and white matter. This makes MRI the best choice for anatomical analysis of the central nervous system.

MRI Image Segmentation

The aim of image segmentation is to divide an MRI image into a set of meaningful and homogeneous areas. The segmentation result is a STereoLithography (.STL) file that shows different regions in the CSF system such as nerve roots, brain, dura and spinal cord. Image segmentation can be performed in 2D or 3D. If the data is defined in 3D space, then normally each slice is segmented individually in a “slice-by-slice” way. The final segmentation results can contain inconsistencies and roughness. Thus, the final 3D segmentation volumes requires a post processing step to smooth the 3D volume to have continuous surface. Advanced 3D segmentation algorithms is desired for more accurate 3D segmentation.

Phase Contrast Magnetic Resonance Imaging

Phase contrast magnetic resonance imaging (PC-MRI) is a particular type of MRI used mainly to determine the flow velocities. PC-MRI can be considered as a method of Magnetic Resonance Velocimetry and provides a method of magnetic resonance angiography. As modern PC-MRI is usually time-resolved, it provides a means of 4D imaging (three spatial dimensions plus time) [43]. To get highly resolved scans in 3D space and time without motion artifacts from the heart or lungs, retrospective cardiac gating are used. First, the patient’s ECG signal is recorded throughout the imaging process. Also, the patient’s respiratory patterns will be tracked during the scan. Then, the continuously collected data in temporary image space can be assigned accordingly to match-up with the timing of the patient heartbeat so the measured blood velocities are an average of multiple cardiac cycles. [44]

Computational Fluid Dynamics

Computational fluid dynamics (CFD) is a subdivision of fluid mechanics that uses numerical methods to analyze and solve fluid flow problems. Computers are used to carry out the calculations required for the simulation of the flow field and the interaction of the fluid with the boundary conditions. High performance computers can be used to solve the large and most complex problems. In this study, initial verification of CFD is typically performed using full-scale bench top in vitro model experimental apparatus. A final validation is often performed using in vivo data for a particular problem.

CFD in Biomedical Engineering

Numerical methods have been applied as an engineering approach to help understand the nature of CSF dynamics. These techniques have been valuable because they can investigate the flow parameters non-invasively. It is difficult to measure all the details of CSF flow using PCMRI or by invasive measurements. Therefore, CFD is valuable in detailed analysis of the CSF flow to determine the importance of different anatomical features and physiological functions on CSF dynamics.

Methodology

In all of the CFD simulations the same basic procedure is followed.

1. The geometry and physical bounds of the problem can be defined using computer aided design. After that, it can be post-processed and then fluid domain will be extracted.
2. The volume occupied by the fluid will be divided into discrete cells called mesh. The mesh could be uniform or non-uniform, structured or unstructured, containing different elements such as hexahedral, tetrahedral, prismatic, pyramidal or polyhedral elements.
3. Boundary conditions will be defined to specify the fluid behavior near the bounding surfaces.
4. For transient problems, we also need to define the initial conditions.
5. The simulation will be carried out by solving the Navier-stocks equations iteratively as a steady-state or transient.
6. Lastly a postprocessor software will be used for the visualization and analysis of the solution.

Obtaining the Model Domain

The CSF space consist of a number of different connected compartments (**Figure 2**). MRI is the widely used technique for determining the shape and the anatomy of compartments in the CSF. Due to limits in resolution, the small anatomical structures such as arachnoid trabeculae cannot be acquired in sufficient detail for CFD simulations. Nerve roots and similar structures can be integrated into the computational domain artificially. When MR images of the CNS have been acquired, the anatomic structures will be extracted by image segmentation software such as ITK-SNAP (Version 3.4.0, University of Pennsylvania, U.S.A.). The final output of the segmentation step is 3D model of the anatomic structures of the CSF domain.

Mesh Generation

For spatial discretization, the fluid domain must be divided into sub-volumes, called computational mesh. An unstructured grids needs to be used for exact representation of CSF space, since structured grids are very difficult to be generated due to the geometric complexity of the CSF spaces. Higher grid densities are applied in zones with expected large velocity gradients, such as at the tip of the nerve roots. Because the accuracy of the obtained solution depends on the quality of the computational grid. Therefore, grid independence or mesh convergence study needs to be performed and solutions obtained with different grid densities have to be compared. Grid independence studies will give an approximation of the relative error related to the mesh size.

Boundary and Initial Conditions

Boundary conditions need to be defined near the fluid domain boundaries. Boundary conditions for CSF models are typically based on MRI but it is not possible to obtain absolute pressures from MRI. This means that velocity and/or flow rate are the only boundary conditions that can be prescribed. The pulsatile CSF flow are produced primarily by the expansion and contraction of blood vessels in and around the CNS, and also by respiration. This means that the CSF boundaries have to be flexible boundaries that can transfer momentum by deformation. Once the boundary conditions are defined, then we need to define initial conditions in the form of velocity and pressure. If results from previous simulations are available, they can be applied to the new grid as initial conditions. Otherwise, zero initial velocity and pressure will be applied.

Discretization Methods

The finite volume method is a common approach used in CFD simulations, as it has a better efficiency in memory usage and solution speed, especially for complex problems and multiphase flows. In the finite volume method, the Navier-Stokes, the mass and energy conservation, and the turbulence equations will change in to a conservative form (**Equation 1**), and then will be solved over discrete control volumes. This method guarantees the conservation of fluxes through a particular control volume. The finite volume equation yields governing equations in the following form,

$$\frac{\partial}{\partial t} \iiint Q dV + \iint F d\mathbf{A} = 0 \quad (1)$$

Where Q is the vector of conserved variables, F is the vector of fluxes, V is the volume of the control volume element, and A is the surface area of the control volume element.

Calculating the Flow

There are many different CFD software for CSF dynamics modelling, such as FLUENT, CFX and free open-source codes OPEM-FOAM, each with their unique powers and weaknesses. CFD software choice depends mainly on the complexity of the model, licensing cost and familiarity with the software. High complexity in terms of mesh size needs a software that can utilize high performance computing resources. While most of CFD software offer parallel processing, the low efficiency of traditional finite volume codes is a significant factor.

CSF flow has an oscillatory component with zero net flow, which makes it impossible to perform steady-state simulations. For transient CFD simulations, the proper time step size has to be chosen, which highly depends on the CSF flow frequencies and the mesh resolution. Commonly used time step sizes for the CSF flow simulations are on the order of 1 ms. Like the grid independence study, the time step independence study must be ensured.

Multiphase Flow

A large number of flows in nature and technology are a mixture of different phases. Physical phases are gas, liquid, and solid, but the definition of phase in a multiphase flow system is applied in a wider sense. In multiphase flow, a phase can be described as a class of material that has a specific inertial response. For example, different-sized solid particles of the same material can be defined as different phases because particles with the same size will have a similar dynamical response to the fluid.

Developments in CFD have provided the basis for additional insight into the dynamics of multiphase flows. At this time, there are two approaches for the numerical simulation of multiphase flows: the Euler-Lagrange approach and the Euler-Euler approach.

Different phases are treated mathematically in the Euler-Euler approach. The concept of phase volume fraction is introduced because the volume of each phase cannot be occupied by another phase. These volume fractions are considered to be constant functions of time and space. Thus, their sum is equal to one. In FLUENT, three different Euler-Euler multiphase models are available such as: the volume of fluid (VOF) model, the Eulerian model and the mixture model.

The mixture model can be used for two or more phases such as fluid or particles. The mixture model solves for the mixture momentum equation and prescribes relative velocities to define the dispersed phases. Applications of the mixture model include miscible fluids. The mixture model can also be used without relative velocities for the dispersed phases to model homogeneous multiphase flow.

Chapter 2: Research Objectives

There is a need to understand the impact of realistic geometry on CSF flow patterns. An anatomically accurate and validated model will allow testing and optimization of CNS therapeutics that could lead to more rapid application for clinical use and reduced cost for non-human primate studies. There is a need to develop a CSF hydrodynamic simulator (flow model) with a realistic geometry and CSF flow distribution. Such a simulator will allow testing and optimization of CNS therapeutics and biomedical technologies. In this dissertation, we studied five main aspects on CSF dynamics as:

Aim 1: CFD Simulation of CSF Dynamics in Non-human Primates

For the first step of this project, since these therapies often require testing on NHPs, our approach was to develop a subject-specific numerical model of CSF hydrodynamics in a cynomolgus monkey, a commonly used species for these studies. The focus of this numerical model was accurate representation of the spinal SAS CSF flow rate and waveform distribution as intrathecal infusion is primarily conducted within the spine. Comparison of CSF dynamics within the numerical model and MRI flow measurements were made to understand its hydrodynamic similarity to in vivo.

Aim 2: Characterization of CSF Dynamics and Geometry in Non-human Primates

The goal of this step was to develop a non-invasive MR imaging protocol to assess CSF dynamics and geometry in NHPs and provide quantitative results based on the measurements. In this step we investigated the SSS geometry and flow compliance distribution in eight healthy NHPs using: 1) 3D, T2 SPACE MRI sequence, optimized to provide very high contrast between CSF and other tissues and 2) a thru-plane phase contrast MRI flow scan obtained at various locations along the SSS. Segmentation methodologies as well as the descriptions of parameters such as the Total Flow, the Mean Velocity, the Reynolds Number and the Volumetric Compensation were introduced in this step to allow us to investigate the CSF behavior in the CNS.

Aim 3: CFD Simulation of CSF Dynamics in Human

In the third step, a subject specific CFD simulator were developed to be used for human. This model was used to address more needs in this field. The objectives of this step was to build upon the body of CSF modeling work by: 1) MRI measurements of SSS geometry and flow distribution in a patient, and 2) CFD simulation of unsteady CSF flow in a SSS model with and without anatomically realistic spinal

cord NR based on the MRI measurements. We created a 3D computational model of the complete CSF system. The 3D model was based on MR images already collected in an ongoing funded research project to quantify CSF flow and geometry in a subject specific human. Following creating the numerical model, we characterized the 3D flow field within the model. This is important, as we need to prove that the model mimics the in vivo CSF flow field and geometry around the brain and CNS. Thus, a series of analysis were carried out to quantify the hydrodynamics and geometric parameters compared to the in vivo data that the model was based on [45-47].

Aim 4: Numerical Investigation of Filtration System Impact on CSF Dynamics

The goal of this step was to develop and validate a computational model for analysis and optimization of CSF filtration therapeutic devices. A major advantage of this project is that we will leverage use of our anthropomorphic CSF system in a CFD model. The major task in this step was to perform a numerical simulation of the filtration system and then validate the simulation results with the experimental data. After completion, we had a fully advanced numerical model to optimize and test multiple CSF filtration protocols and tested in detail a catheter design provided by Minnetronix [48]. After validation of the model, we parametrically assessed different CSF flow rates applied by the filtration pump and determine the impact on local CSF dynamics (e.g. velocity profiles). Different flow rates were examined with respect to CSF pulsation amplitude and frequency.

Aim 5: CFD simulation of Intrathecal Drug Delivery

The overarching goal of this step was to develop and validate a numerical simulator for brain therapeutic development. Our focus was on the mimicking the macroscale dynamics of CSF motion around the brain and spinal cord. We conducted preliminary drug delivery and spreading simulation with a catheter system to demonstrate future research project possibilities.

Project Sustainability

The aim of this research was to allow a start towards formation of a neural engineering group. The proposed CFD model will have potential to allow rapid investigation of many important questions to medical companies and basic science researchers. We expect that a model in hand will allow many of these questions to be answered and make opportunities for federal grants allowing sustainability of the project. In specific, the following important questions will be possible to investigate:

1. How can we use CFD model to teach medical doctors about the CSF system physiology and therapies?
2. How does catheter tip location or design impact drug distribution (e.g. ventricular vs. cervical or near spinal cord NR)
3. Can we engineer a catheter shape/geometry for specific applications/diseases?
4. What impact does drug dose rate and volume have on drug spread (e.g. bolus vs. constant infusion protocols)?
5. How do drug kinetics alter spreading (e.g. viscosity, buoyancy)
6. What is the optimal delivery method to obtain consistent drug spread results?

Deliverables

This project provided preliminary data used for research grant applications in the area of gene vector drug delivery and CSF filtration. We also filed one patent and multiple invention disclosures based on the proposed simulator. The following full-length peer-reviewed journal papers were published based on primarily results from this dissertation:

Publication 1: Anthropomorphic model of intrathecal cerebrospinal fluid dynamics within the spinal subarachnoid space: spinal cord nerve roots increase steady-streaming

M Khani, LR Sass, T Xing, MK Sharp, O Balédent, BA Martin

Journal of biomechanical engineering 140 (8), 081012, 2018

Publication 2: Nonuniform moving boundary method for computational fluid dynamics simulation of Intrathecal cerebrospinal flow distribution in a Cynomolgus monkey

M Khani, T Xing, C Gibbs, JN Oshinski, GR Stewart, JR Zeller, BA Martin

Journal of biomechanical engineering 139 (8), 081005, 2017

Publication 3: **Impact of Neurapheresis system on intrathecal cerebrospinal fluid dynamics: a computational fluid dynamics study**

M Khani, L Sass, A McCabe, LZ Verbick, SP Lad, MK Sharp, B Martin

Journal of biomechanical engineering, 2019

Publication 4: **Characterization of intrathecal cerebrospinal fluid geometry and dynamics in cynomolgus monkeys (*macaca fascicularis*) by magnetic resonance imaging**

M Khani, BJ Lawrence, LR Sass, CP Gibbs, JJ Fluid, JN Oshinski, ...

PloS one 14 (2), e0212239 2019

Wider Impact

The proposed research uniquely aligns with multiple targets of the Grand Challenges for Engineering in the 21st Century including: Advancing Personalized Learning, Reverse-Engineering of the Brain, Engineering the Tools of Scientific Discovery and Enhancing numerical modeling. Completion of this research project will bring faculty at the University of Idaho closer to these targets and allow students exciting learning opportunities to get involved in the challenge.

Future Work

1-Impact of Catheter Placement on CSF Dynamics in Non-Human Primates

Therapeutic substances have been administered directly into the CSF by using an intrathecal catheter which provides a strategy to bypass the Blood Brain Barrier (BBB). In addition to delivery of

next generation treatments, intrathecal catheters are currently being used in humans for chronic pain management.

An animal model is commonly used to identify toxicity effects and test the efficacy of the drug absorption into the CNS tissue. Cynomolgus Macaques are one of the gold-standard models for drug development trials [49, 50]. While there have been several studies that look into the effect of catheter placement of CSF flow in humans [51] and drug distribution in pigs[52], no studies have looked at how catheter placement affects CSF flow in Cynomolgus Macaques. Altered CSF dynamics has the potential to change dosing requirements, drug distribution and potentially cause harm to patients. Given the complexity of CSF circulation, and the potential benefits from a better understanding of CSF flow dynamics, more research into this area is warranted. Our previous study[53] developed a quantitative method to characterize CSF dynamics and geometry in non-human primates (NHPs). This method was able to reliably measure CSF parameters over a two-week period in a group of 8 NHPs. A new study can use the same techniques on additional scans in that dataset to: 1) Quantify CSF parameter changes after catheter placement, 2) track these changes over time, and 3) see if catheter placement in the lumbar or cervical region has a different effect on CSF dynamics.

2- Parametric Study of Key Factors for Intrathecal Drug Delivery

Spinraza is a new medication used to treat spinal muscular atrophy, a rare neuromuscular disorder. Nusinersen or Spinraza became the first approved drug used in treating this specific neurological disease. Nusinersen costs \$750,000 in the first year and \$375,000 annually after that in the United States as of 2019 [54].

A 3D anatomically-detailed model can be used to investigate the possibility and a range of effects of injection parameters on intrathecal drug delivery to reduce the cost of drug usage and increase drug spread by optimizing the drug injection protocol. Developing the current numerical model by adding a drug injection needle and addressing the effect of catheter position, drug injection flow rate

and bolus volume on the resulting drug distribution and verify numerical results against in vitro measurements can be accomplished using the provided numerical modeling platform for systemwide CSF solute transport.

Chapter 3: Non-uniform Moving Boundary Method for Computational Fluid Dynamics Simulation of Intrathecal Cerebrospinal Flow Distribution in a Cynomolgus Monkey

Abstract

A detailed quantification and understanding of cerebrospinal fluid (CSF) dynamics may improve detection and treatment of central nervous system (CNS) diseases and help optimize CSF system-based delivery of CNS therapeutics. This study presents a computational fluid dynamics (CFD) model that utilizes a non-uniform moving boundary approach to accurately reproduce the non-uniform distribution of CSF flow along the spinal subarachnoid space (SAS) of a single cynomolgus monkey. A magnetic resonance imaging (MRI) protocol was developed and applied to quantify subject-specific CSF space geometry and flow and define the CFD domain and boundary conditions. An algorithm was implemented to reproduce the axial distribution of unsteady CSF flow by non-uniform deformation of the dura surface. Results showed that maximum difference between the MRI measurements and CFD simulation of CSF flow rates was <3.6%. CSF flow along the entire spine was laminar with a peak Reynold's number of ~ 150 and average Womersley number of ~ 5.4 . Maximum CSF flow rate was present at the C4-C5 vertebral level. Deformation of the dura ranged up to a maximum of $134 \mu\text{m}$. Geometric analysis indicated that total spinal CSF space volume was $\sim 8.7 \text{ ml}$. Average hydraulic diameter, wetted perimeter and SAS area was 2.9 mm , 37.3 mm and 27.24 mm^2 , respectively. CSF pulse wave velocity along the spine was quantified to be 1.2 m/s .

Introduction

Cerebrospinal fluid (CSF) plays a vital role in the immunological support, structural protection and metabolic homeostasis of the central nervous system (CNS). A detailed understanding of CSF dynamics may improve treatment of several CNS diseases and help to optimize CSF system-based CNS therapeutics. The importance of CSF dynamics have been investigated in several CNS diseases that include syringomyelia[3], Alzheimer's disease[1], Chiari malformation[5], and hydrocephalus[8]. Recent studies have examined the possible role of CSF as a conduit for distribution of therapeutic molecules to neuronal and glial cells of CNS tissues[55, 56]. Intrathecal-based CNS therapeutics for treatment of devastating CNS disorders such as Alzheimer's, amyotrophic lateral sclerosis, Parkinson's and autism are under investigation. Researchers found that brain tissue is rapidly "washed out" with CSF during sleep in a mouse model[57]. Tracer studies showed that solutes within the CSF are

transported into and out of the brain tissue via a leptomeningeal or perivascular pathway[58]. While many studies have shown increasing importance of the role of CSF in CNS system homeostasis, there is a paucity of information on CSF biofluid mechanics.

CSF-based brain therapeutics are gaining interest because they allow direct pharmaceutical targeting of the CNS that can help minimize some side effects associated with conventional oral and intravenous based pharmacotherapies and allows delivery of larger molecule sizes to the CNS that may not normally be able to cross the blood-brain-barrier. The CSF is a promising route with many potentially important roles for CNS therapeutics such as: a) direct delivery of large drug molecules to the CNS tissue that is not possible via blood injection due to the blood brain barrier, b) CSF filtration, termed neurophoresis, to remove unwanted toxins in diseases such as meningitis. c) CSF cooling, termed CSF hypothermia, to slow down traumatic brain and spinal cord (SC) injury following severe accidents. However, while CNS therapeutics have a great deal of potential, they require expensive and restricted non-human primate (NHP) studies to reach clinical use. This expense makes detailed testing and optimization of brain therapeutic systems and medications difficult.

There is a need to develop a CSF hydrodynamic simulator (flow model) with a realistic geometry and CSF flow distribution. Such a simulator will allow testing and optimization of CNS therapeutics. Since these therapies often require testing on NHPs, our approach was to develop a subject-specific numerical model of CSF hydrodynamics in a cynomolgus monkey, a commonly used species for these studies. The focus of this numerical model was accurate representation of the spinal SAS CSF flow rate and waveform distribution as intrathecal infusion is primarily conducted within the spine. Comparison of CSF dynamics within the numerical model and MRI flow measurements were made to understand its hydrodynamic similarity to in vivo.

Methods and Materials

Measured Data

Ethics Statement

This study was submitted to and approved by the local governing Institutional Animal Care and Use Committee (IACUC). This study did not unnecessarily duplicate previous experiments and alternatives to the use of live animals were considered. Procedures used in this study were designed with the consideration of the well-being of the animals.

Animal Selection

A healthy four-year-old adult male cynomolgus monkey (*Macaca fascicularis*, origin Mauritius) from Charles River Research Models, Houston TX with a weight of 4.39 kg was selected for the study. This animal was purpose-bred and experimentally naïve.

Pre-MRI NHP Preparation

The NHP was positioned in the scanner in the supine orientation with natural breathing (no mechanical ventilation). During each scan, heart rate (HR) and respiration was monitored with ~1 liter/minute of oxygen and 1-3% isoflurane anesthetic administered via oral mask for sedation and intubation for the duration of the scanning procedures.

MRI Scan Protocols

MRI measurements were collected at Northern Biomedical Research on a Philips 3T scanner (Achieva, software V2.6.3.7, Best, The Netherlands). This NHP did not have prior administration of intrathecal drugs and/or catheter systems in the spine. Total scan time to quantify SAS geometry and flow, not including pre-MRI NHP preparation, was 1 hour and 21 minutes.

Phase-contrast MRI Protocol for CSF Flow Detection

Phase-contrast MRI measurements were collected with retrospective ECG gating and 24 heart phases were reconstructed over the cardiac cycle. In-plane resolution was reconstructed at 0.45 x 0.45 mm and slice thickness was 5.0 mm. Slice location for each scan was oriented perpendicular to the CSF flow direction with slice planes intersecting vertebral discs. These locations included the foramen magnum (FM) and vertebral disks located between the C2-C3, T4-T5, T10-T11 and L2-L3 vertebral levels (Figure 1a). Velocity encoding value was 5 cm/s at the FM and L2-L3, and 10 cm/s at all other locations.

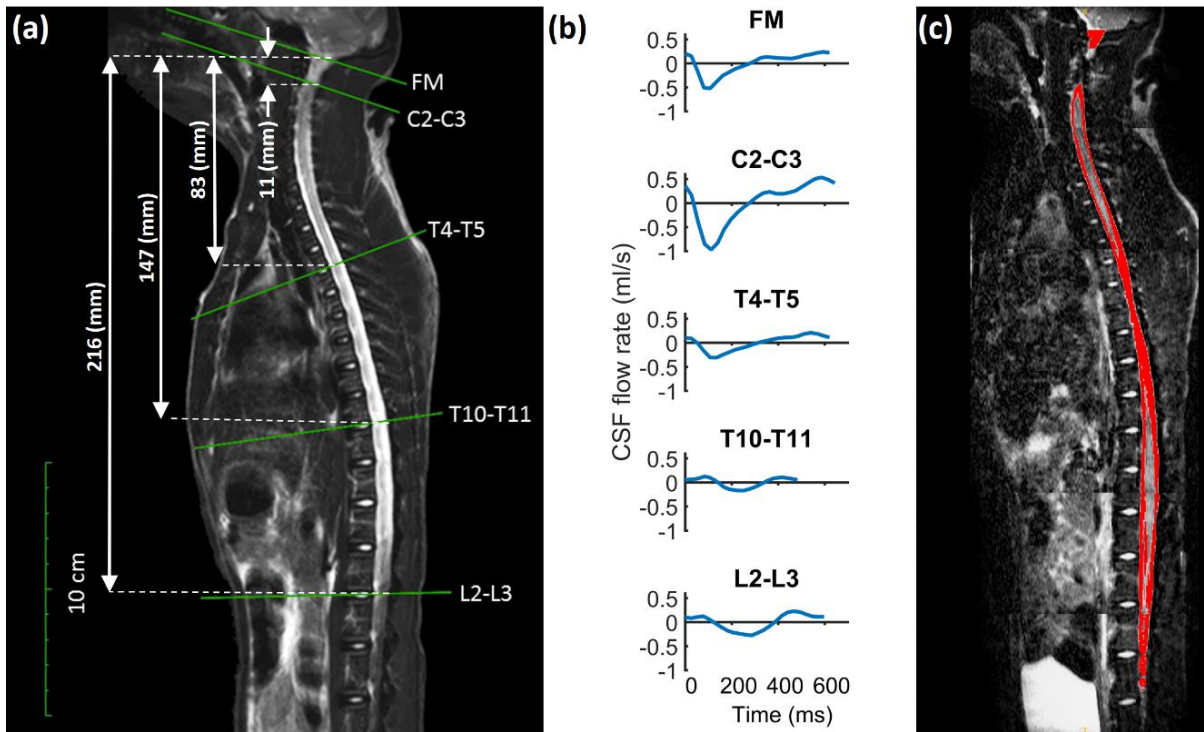


Figure 3.1. (a) T2-weighted MR image of the entire spine for the cynomolgus monkey analyzed. Axial location and slice orientation (lines) of the phase-contrast MRI scans obtained in the study. Slice axial distance from foramen magnum indicated by dotted lines (b) The CSF flow rate based on in vivo PCMRI measurement at FM, C2-C3, T4-T5, T10-T11, and L2-L3. (c) sagittal view of the SAS segmentation based on T2-weighted MRI.

MRI CSF Space Geometry Protocol

A stack of 720 axial images were acquired using a volumetric isotropic T2w Acquisition (VISTA) for complete coverage of the spinal SAS geometry (Figure 1a). Scan time was 55 minutes with parameters indicated in Table 1. The anatomical region scanned was ~31 cm in length and included the entire spinal SAS extending caudally to the filum terminale. Images had a 0.5 mm slice spacing and 0.38 mm isotropic in-plane resolution.

Table 3.1. Anatomic and CSF flow MRI scan protocol parameters.

Parameter	Anatomic (T2-VISTA)	CSF Flow (phase-contrast MRI)
Acquisition contrast	T2	Flow encoded
Acquisition type	3D	2D
Slice Thickness	1 mm	5
Slice spacing	0.5 mm	N/A
Pixel bandwidth	481	192
Pulse Sequence	TSE	TFE
Transmit coil	15 ch. Sense Spine Coil	15 ch. Sense Spine Coil
Duration	55 minutes	4 minutes each (20 minutes total)
Number of slices	660	N/A
Image matrix	864x864	224x224
In-plane resolution	0.375 mm isotropic	0.446 mm isotropic
TR	2000	11.293
TE	120	6.774
Cardiac phases	N/A	24
R-R interval	N/A	482 - 644 ms
Encoding direction	N/A	Thru-plane
Plane orientation	Axial	Axial
Trigger	N/A	Retrospective ECG
Velocity encoding	N/A	5 cm/s at FM and L2-L3 10 cm/s at C2-C3, T4-T5, T10-T11

CSF Flow Quantification

CSF flow was quantified for each of the axial locations shown in Figure 1b. As detailed in our previous studies [45, 59], the CSF flow waveform, $Q_{(t)}$, was computed within Matlab based on integration of the pixel velocities with $Q(t) = \sum A_{pixel} [V_{pixel}(t)]$, where A_{pixel} is the area of one MRI pixel, V_{pixel} is the velocity for the corresponding pixel, and $Q_{(t)}$ is the summation of the flow for each pixel of interest as in our previous studies.

MRI Geometry Post Processing

The high-resolution T2-weighted anatomic MRI images were semi-automatically segmented using the free open-source ITK-snap software (Version 3.0.0, University of Pennsylvania, U.S.A.). Details on the segmentation procedure are provided in our previous work[60]. SC nerve roots and denticulate ligaments were not included in the model as they were not possible to accurately quantify at the acquired MRI resolution. Individual SC nerves were quantified at the filum terminale. The final segmentation (Figure 1c) was exported in STereoLithography format (Figure 2a). The initial geometry of the numerical model was based on the time-averaged geometry measured over the MRI acquisition period.

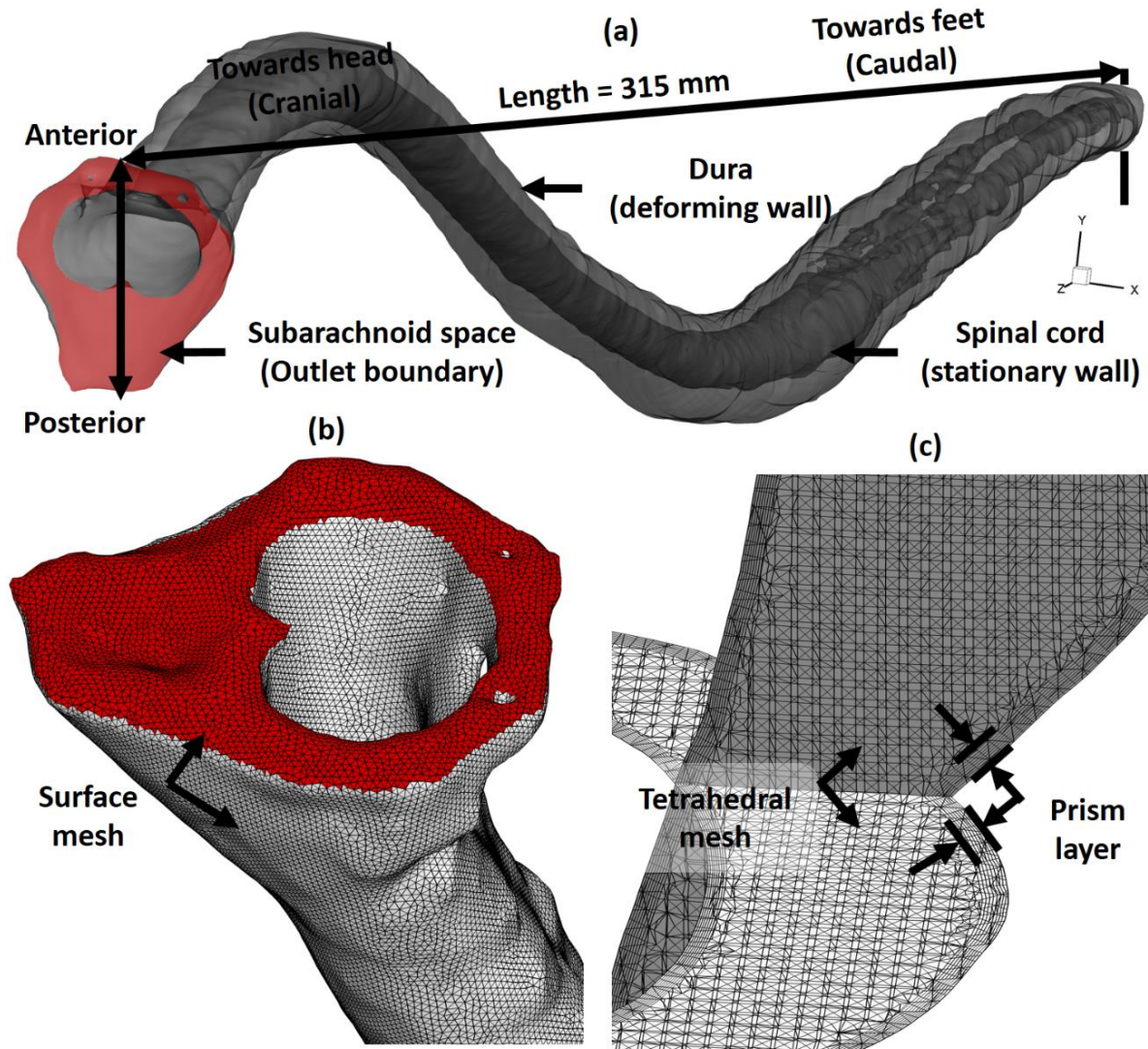


Figure 3.2. (a) Three-dimensional CFD model of the SAS. (b) Zoom of the upper cervical spine mesh showing the model inlet (top). (c) Volumetric mesh visualization in the axial and sagittal planes within the cervical SAS.

Flow Model

Our overall flow model approach was to solve for the CSF flow field within the spinal SAS using CFD with a specified moving boundary motion based on the *in vivo* MRI measurements. The volume flow rate of the incompressible CSF flow along the spine was purely determined by the mass/volume conservation. Results were verified based on numerical independence studies, quantified in terms of geometry and hydrodynamics and validated based on comparison to the *in vivo* measurements.

Non-uniform Mesh Deformation to Reproduce CSF Flow Along Spine

The phase-contrast MRI measurements showed a complex non-uniform distribution of CSF flow along the spine. Thus, to reproduce the non-uniform flow a non-uniform deformation of the computational mesh was implemented at each time step by a User Defined Function (UDF) applied within ANSYS FLUENT (ANSYS® Academic Research, Release 17.2). A spring-based smoothing algorithm was applied to the mesh based on the calculated deformation within each section, as described in the following steps (Flow chart with steps 1-7 indicated in Figure 3a):

Step 1) In vivo CSF flow rates along the spine were measured at five distinct locations (Figure 1b). To generate a smooth CSF flow distribution along the spine within 1 mm sections, these five distinct flow rates were spatial-temporal filtered in MATLAB using the 2D “fit” function with fitype = “spline” configuration. Some HR variability was present between the PCMRI scans. Thus, the diastolic portion of the CSF flow waveforms with a shortened cardiac cycle was extended using methods previously developed by Schmidt-Daners et al.[61]. Maximum waveform extension was 180 ms at T10-T11. The smooth CSF flow distribution along the spine was then read into the mesh deformation algorithm (Figure 3a).

Step 2) Maximum and minimum geometry height in the caudocranial direction (Z_{max} and Z_{min}) was calculated. Total model length was calculated as the difference of these values ($Length = Z_{max} - Z_{min}$).

Step 3) To apply the non-uniform deformation on each spine node, the entire geometry was divided into “n” sections with 1 mm height (315 total sections with $\Delta h = 1\text{ mm}$). Total model length was 315 mm.

Step 4) The center of each section was defined based on the maximum and minimum location along the X- and Y-axis based on equation (2).

$$\begin{aligned} X_C &= \frac{X_{max} - X_{min}}{2} + X_{min} \\ Y_C &= \frac{Y_{max} - Y_{min}}{2} + Y_{min} \end{aligned} \quad (2)$$

Where subscripts “max”, “min” and “C” denote maximum, minimum and center of each section, respectively (see Figure 3b for diagram).

Step 5) To identify the dura and SC location, each section was divided into 32-parts each containing 11.25 degrees (10080 total parts for entire model). Further calculations of mesh deformation were repeated for each part.

Step 6) Our approach was to move the dura location and maintain the SC in a fixed position (SC compressibility is likely small). A limitation value (see Figure 3b) was calculated based on the maximum and minimum radius of each part using equation (3).

$$Limit = r_{\min} + \frac{r_{\max} - r_{\min}}{2} \quad (3)$$

Each point with a greater radius than the limit value was allowed to move during the simulation and all others remained fixed in location.

Step 7) The time-course radial displacement for each node within each part was calculated based on the difference in CSF flow rate across each section (ΔQ). This variation was assumed equal to the volume change of each section at each time-step ($\Delta V = \Delta Q \cdot \Delta t$). Where Δt denotes solver time-step size. Under the assumption of zero dura and SC axial motion along the Z-axis, deformation was only calculated within the XY-plane (Figure 3b). Due to the relatively small angle within each part (11.25°), the outer boundary of each part (dura) was assumed as a circular arc. Thus, radial displacement of each node on the dura surface for each part, Δr , was computed based on area variation within that pseudo-circular part, where $\Delta A = \Delta V / \Delta h$, using equation (4).

$$\Delta r = \sqrt{r_{\max}^2 - \Delta A} - r_{\max} = \sqrt{r_{\max}^2 - \frac{\Delta Q \cdot \Delta t}{\pi \cdot \Delta h}} - r_{\max} \quad (4)$$

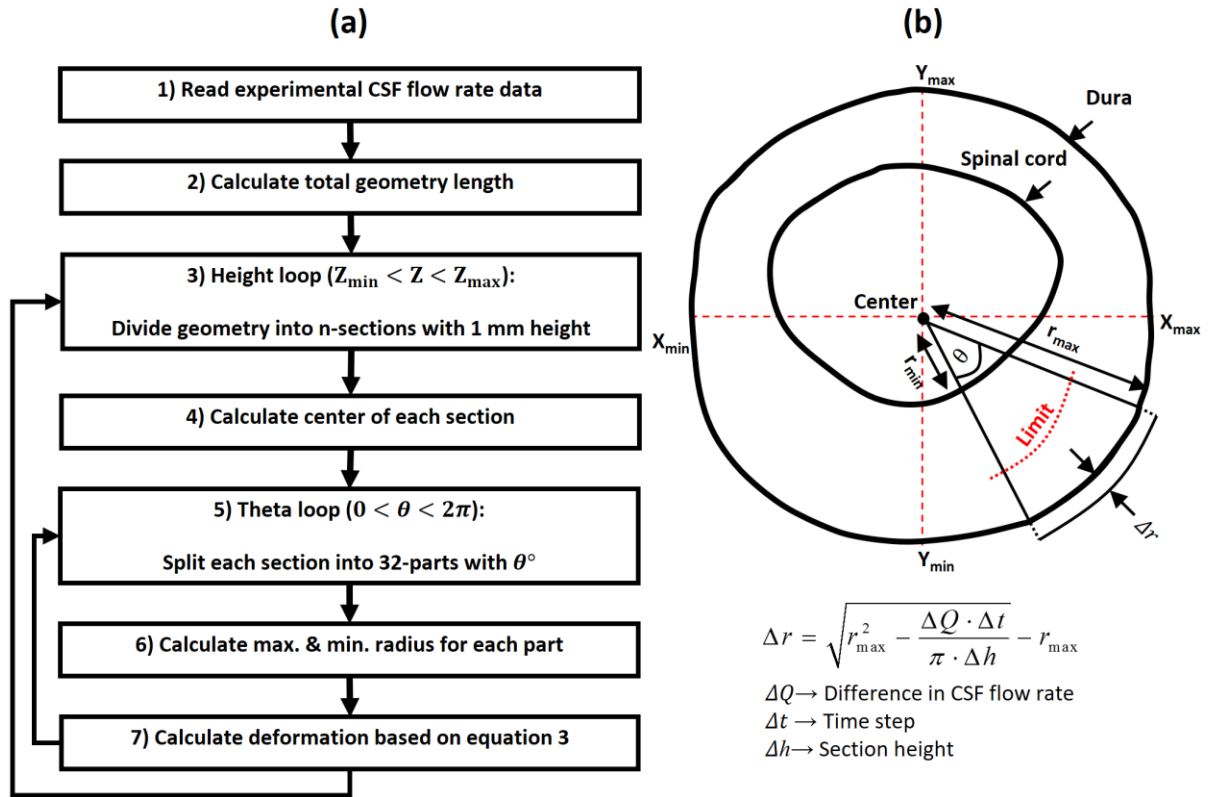


Figure 3.3. (a) Dynamic mesh motion flow chart used for the CFD simulation. Recursive arrows indicate repetition of steps. (b) A 2D axial cross-section with relevant variables and key equation used to compute radial deformation of the dura.

Numerical Solver Settings

The computational domain with non-uniform unstructured grid (Figure 2b) was generated within ANSYS ICEM CFD software and consisted of approximately 11.2 million tetrahedral elements (Figure 2c). The commercial finite volume CFD solver ANSY FLUENT was used to solve the continuity (Equation 5) and Navier-Stokes (Equation 6) equations numerically using the finite volume method.

$$\nabla \cdot (\rho u) = 0 \quad (5)$$

$$\rho \left(\frac{\partial u}{\partial t} + u \cdot \nabla u \right) = -\nabla P + \mu \nabla^2 u \quad (6)$$

Where ρ is the density, μ is the dynamic viscosity, and u and P describe the velocity and pressure fields, respectively.

The laminar viscous model was used to simulate laminar incompressible Newtonian flow. CSF hydrodynamic characteristics were considered to be equivalent with water at body temperature[62, 63] (density of $\rho=993.3 \text{ kg/m}^3$ and dynamic viscosity of $\mu=0.6913 \text{ mPa}\cdot\text{s}$). A no slip boundary condition was imposed at the walls. A pressure-outlet boundary condition with zero (pa) gauge pressure was defined at the model cranial opening. Flow at the model cranial opening was produced based on the non-uniform deformation of the model wall. The model terminated at the caudal end and was only open at the cranial end (Figure 2). Thus, it was unnecessary to prescribe an inlet velocity boundary condition. Deformation of the outlet boundary was set as a faceted wall. Second order upwind numerical scheme was used for both momentum and pressure gradient solver settings. The utilized transient formulation was second order implicit with default values for under relaxation factors. The convergence criteria for continuity and velocity was set to $1\text{E-}08$. CFD simulation for each cycle required ~ 14 hours to complete in parallel mode with 141 GB RAM and 30 processors at a clock speed of 2.3 GHz. Total simulation time was 28 hours for the two cycles simulated. Results are presented for the 2nd cycle only.

Verification Studies

To verify our numerical results, independence studies were carried out to determine the effect of cycle, mesh size and time-step size on velocity results for a 6 cm model length located within the thoracic spine (Figure 4a, Table 2). Our focus was velocity since velocity was the parameter measured by the MRI measurements used to define the numerical model. A baseline simulation was conducted for a coarse tetrahedral mesh with wall prism layers containing a total of 0.6 million cells. Subsequent “medium” and “fine” simulations were carried out with mesh size and prism layer length halved for each case. Results were assessed at three axial slice locations separated by a 2 cm distance. For each slice, z-direction velocities, V_w , were quantified using a rake containing $n = 1000$ points along a straight line (Figure 4b). Maximum error between each case was calculated at peak systolic flow using the following equation:

$$error = \max \left(\left| \frac{V_{w\text{fine}}(t_{\text{sys}},n) - V_{w\text{medium}}(t_{\text{sys}},n)}{\text{mean}(V_{w\text{fine}}(t_{\text{sys}},n))} \right| \right) \times 100 \quad (7)$$

Table 3.2. Verification of results by numerical independence studies— values show the maximum relative error for velocity in the z-direction for the three axial planes analyzed (Figure 4).

Independence study	Parameter to study	Constant parameters	Maximum error (%)
Grid size	MS= 0.5 mm, GS= 0.6 M PS= 0.05 mm, PN= 3	TS=CT/66	10.76
	MS= 0.25 mm, GS= 1.2 M PS= 0.025 mm PN= 5	CN=2	4.77
	MS= 0.125 mm, GS= 7.5 M PS= 0.0125 mm, PN=8		
Time Step Size	CT/33	GS=1.2 M	10.34
	CT/66	CN=2	2.06
	CT/132		
Period number	1	GS=1.2 M	40.0
	2	TS=CT/66	1.59
	3		

GS = Grid Size, PS = Prism Size, PN = Prism Number, MS = Mesh Size,

CN = Cycle Number, M = Million cells, CT = Cycle Time in seconds, TS = Time Step size

Maximum error for the medium versus fine grid was 4.7% and coarse versus medium grid was 10.76%. Thus, subsequent independence studies were carried out with the medium grid. Three time-step sizes were investigated through three flow cycles. Unsteady velocity was monitored at three different points within each of the slice locations and used to compute error (i.e. $V_{w\text{fine}(t_{\text{sys}},n)} = V_{w\text{fine}(t)}$ in equation 4). A time-step size of 0.01 seconds was selected for future studies having a maximum error of 2.1%. Similarly, cycle independence results for unsteady velocity showed that velocity variation after the first cycle was negligible (~1.5%). Thus, results for the final CFD study were analyzed based on the second cycle with a medium grid and time-step size of 0.01 seconds.

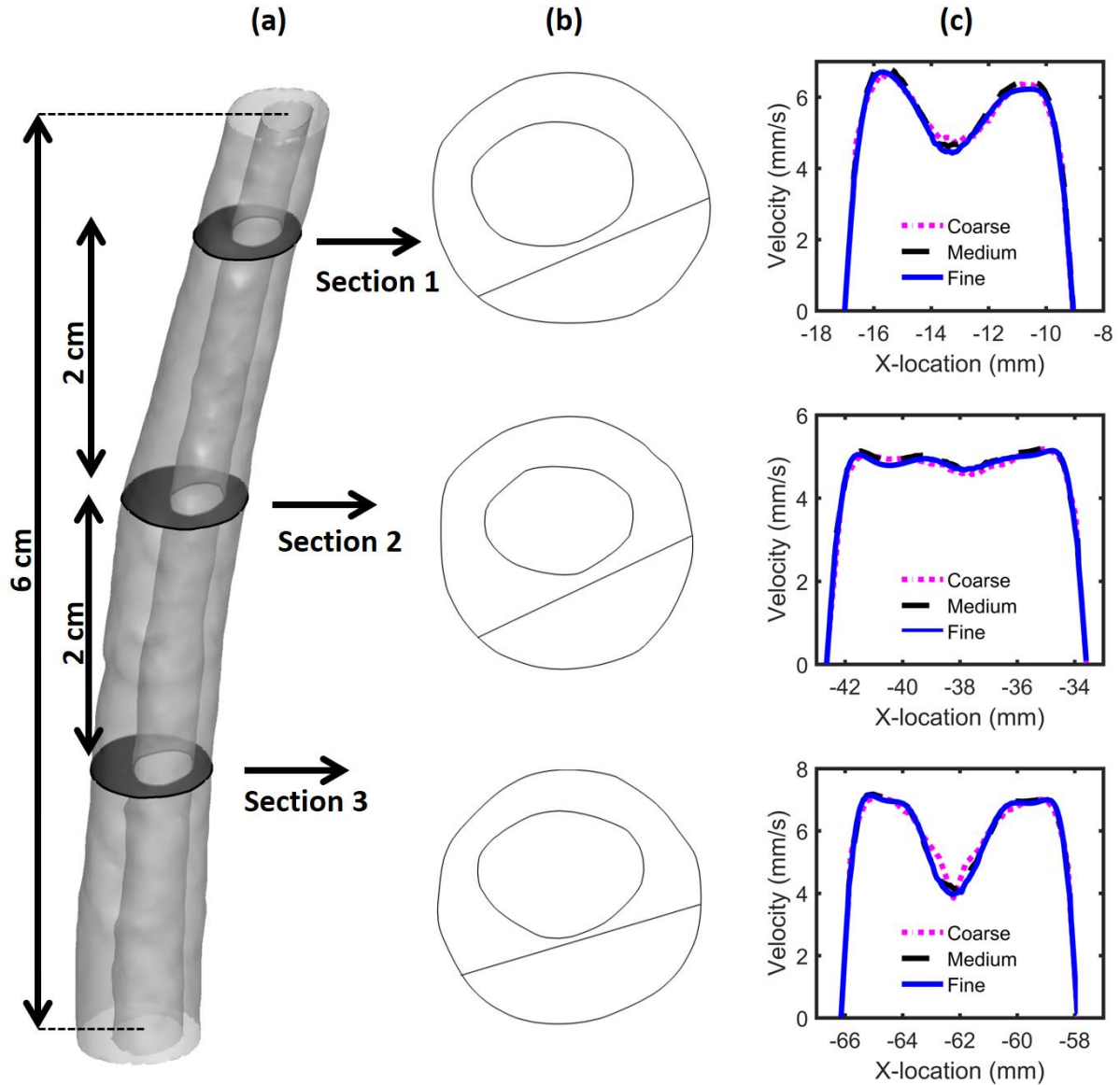


Figure 3.4. (a) 3D geometry of the independence study and axial plane positions (b) line location along each plane (c) Peak systolic w-velocity component visualized along each line for the three grids (coarse, medium and fine).

Geometric Quantification

Based on the 3D reconstruction and meshing, the following geometric parameters were calculated along the spine at 1 mm intervals similar to our previous studies [59]. Cross-sectional area of SAS, $A_{cs} = A_d - A_c$, was determined based on cross-sectional area of the SC, A_c , and dura, A_d .

Hydraulic diameter for internal flow within a tube, $D_H = 4A_{cs} / P_{cs}$, was determined based on the cross-

sectional area and wetted perimeter, $P_{cs} = P_d + P_c$. Wetted perimeter was computed as the sum of the SC, P_c , and dura, P_d , perimeter. Each of these parameters was calculated within an UDF compiled in ANSYS FLUENT after the computational mesh was formed. The MRI-based time-averaged geometry, at baseline or zero deformation, was used to compute the above parameters.

Hydrodynamic Quantification

The hydrodynamic environment at 1 mm slice intervals along the entire spine was assessed by

Reynold's number based on peak flow rate, $Re = \frac{Q_{sys} D_H}{\nu A_{cs}}$, and Womersley number based on hydraulic

diameter. In this equation, Q_{sys} is the temporal maximum of the local flow at each axial location along the spine obtained by interpolation from the experimental data and ν is the kinematic viscosity of the fluid. CSF was assumed to have a viscosity of water at body temperature. Reynold's number at peak systole, or the ratio of steady inertial forces to viscous forces, was utilized as an indicator of the presence of laminar flow ($Re < 2300$) along the spine. It should be noted that this formulation of Reynolds number is only an indicator of laminar flow for flow within a straight circular pipe. We provide this number for comparison to many previous studies in the field that have used it as an indicator of the

flow type [60]. Womersley number, $\alpha = \frac{D_h}{2} \sqrt{\omega / \nu}$, was computed where ω is the angular velocity of the volume flow waveform with $\omega = 2\pi / T$) and ν is the kinematic viscosity of CSF ($\nu = \mu / \rho$). Womersley number was used to quantify the ratio of unsteady inertial forces to viscous forces, which was found to be large for SAS CSF flow relative to viscous forces by Loth, et al.[64]. A Womersley number greater than 5 indicates transition from parabolic to “m-shaped” peak-systolic velocity profiles for oscillatory flows[65]. CSF pulse wave velocity (PWV) was quantified as an indicator of CSF space stiffness. PWV was quantified based on the timing of peak systolic CSF flow rate along the spine using a method similar to Kalata et al. [66]. A linear fit was computed based on the peak systolic flow rate arrival time with the slope being equivalent to the PWV.

Validation of Numerical Simulation flow results

Simulation results were compared to the in vivo measurements to help understand how well the simulation reproduced the in vivo CSF flow in terms of distribution and velocity profiles along the spine. Similar to studies previously conducted by our research group for humans [60], simulation results

and in vivo measurements were compared at each phase-contrast MRI slice location (FM through L2-L3) in terms of unsteady CSF flow rate. Maximum percent difference in CSF flow rate, $Q_{\%error}$, was computed as the instantaneous difference in CSF flow in the CFD simulation and the MRI measurements, $Q_{CFD}(t) - Q_{MRI}(t)$, divided by the maximum of the absolute value of MRI derived CSF flow over the cardiac cycle.

Peak flow patterns were also assessed visually to understand any differences in flow fields. Although the primary objective of this study was to simulate CSF flow rate distribution along the spine, we also compared the numerical results to in vivo MRI measurements in terms of the following parameters: peak systolic and diastolic velocity values (for any pixel in the plane of interest) and peak systolic velocity profiles.

Results

The relative axial location for each vertebral disc along the cynomolgus monkey spine with respect to the numerical model is shown in Table 3. Axial locations along the model are provided with respect to the SC center coordinate for a plane positioned parallel to each disk and intersecting the SC (orthogonal to CSF flow direction).

Table 3.3. Reference chart for vertebral disk location with respect to axial distance from the foramen magnum.

Vertebral level	Distance from foramen magnum (mm)
FM	0
C1-C2	4.0
C2-C3	11.5
C3-C4	16.1
C4-C5	30.2
C5-C6	36.6
C6-C7	43.9
C7-T1	50.7
T1-T2	58.4
T2-T3	66.0
T3-T4	74.9
T4-T5	83.0
T5-T6	92.1
T6-T7	101.8
T7-T8	111.7
T8-T9	122.3
T9-T10	134.0
T10-T11	147.1
T11-T12	162.6
T12-L1	178.9
L1-L2	197.2
L2-L3	215.8
L3-L4	236.2
L4-L5	256.9
L5-S1	279.7
S1-Co1	301.0
Caudal end	312.9

FM= Foramen Magnum, C= Cervical, T= Thoracic, L= Lumbar, S=Sacrum, Co= Coccygeal.

Geometric Parameters

Total CSF volume within the SAS from the FM to spinal canal termination was 8.7 ml for the single cynomolgus monkey analyzed (Table 4). For that same region, the SC volume was 4.5 ml. Mean values of surface area were 41.5 and 14.2 mm² for the dura and SC, respectively. Mean values of perimeter were 22.7 and 14.5 mm for the dura and SC, respectively. As expected, maximum area and perimeter of the dura, SC and SAS was located at the FM (Figure 5a and b). A notable local increase in area and perimeter was present at ~30 mm caudal to the FM. Hydraulic diameter, omitting the model termination region (caudal), had a minimum value of 1.74 mm occurring at a distance of 28 mm caudal

to the FM within the cervical spine (Figure 5c). Hydraulic diameter was larger at both the FM and within the intrathecal sac enlargement of the SAS than elsewhere.

Table 3.4. Summary of hydrodynamic and geometric results from the numerical simulation. Average, maximum and minimum values for each parameter are computed based on the full SAS length.

Parameter	Average	Maximum	Minimum
P_c (mm)	14.59	29.41	3.41
P_d (mm)	22.71	32.69	12.54
P_{sas} (mm)	37.30	62.10	16.99
A_c (mm²)	14.29	41.66	1.75
A_d (mm²)	41.53	103.71	13.18
A_{sas} (mm²)	27.24	62.06	8.91
Volume_c (ml)	4.51	4.51	4.51
Volume_d (ml)	13.25	13.28	13.22
Volume_{sas} (ml)	8.74	8.77	8.71
D_H (mm)	2.93	4.56	1.59
Re	53.51	149.90	2.47
α	5.42	8.45	2.95
V_{peak-sys} (cm/s)	-3.08	-0.08	-9.30
V_{peak-dia} (cm/s)	1.85	5.57	0.29
V_{mean-sys} (cm/s)	-1.47	-0.11	-5.50
V_{mean-dia} (cm/s)	0.94	3.02	0.10
Q_{peak-sys} (ml/s)	-0.36	-0.01	-1.04
Q_{peak-dia} (ml/s)	0.23	0.58	0.01
PWV (m/s)	1.19	N/A	N/A
Δr (μm)	7.79	114.91	-134.03

P_c = Spinal cord perimeter, P_d = Dura perimeter, P_{sas} = Subarachnoid space perimeter

A_c = Spinal cord area, A_d = Dura area, A_{sas} = subarachnoid space area

D_H = Hydraulic diameter, Re = Reynold's number, α = Womersley number

V = Velocity, Q = CSF Flow rate, Peak-sys = Systolic peak flow, Peak-dia = Diastolic peak flow

PWV = Pulse wave velocity, Δr = Radial deformation.

Hydrodynamic Parameters

Womersley number ranged from 8.45 to 2.95 (Table 4, Figure 5d). Local maxima for Womersley number were present within the intrathecal sac ($\alpha = 8.4$), thoracic enlargement ($\alpha = 7.1$) and at the FM ($\alpha = 7.4$). Womersley number had local minima within the cervical spine and just rostral to the intrathecal sac. Maximum Reynold's number was 149.9 and located in the cervical spine where CSF flow was maximum and the SAS had a relatively small hydraulic diameter.

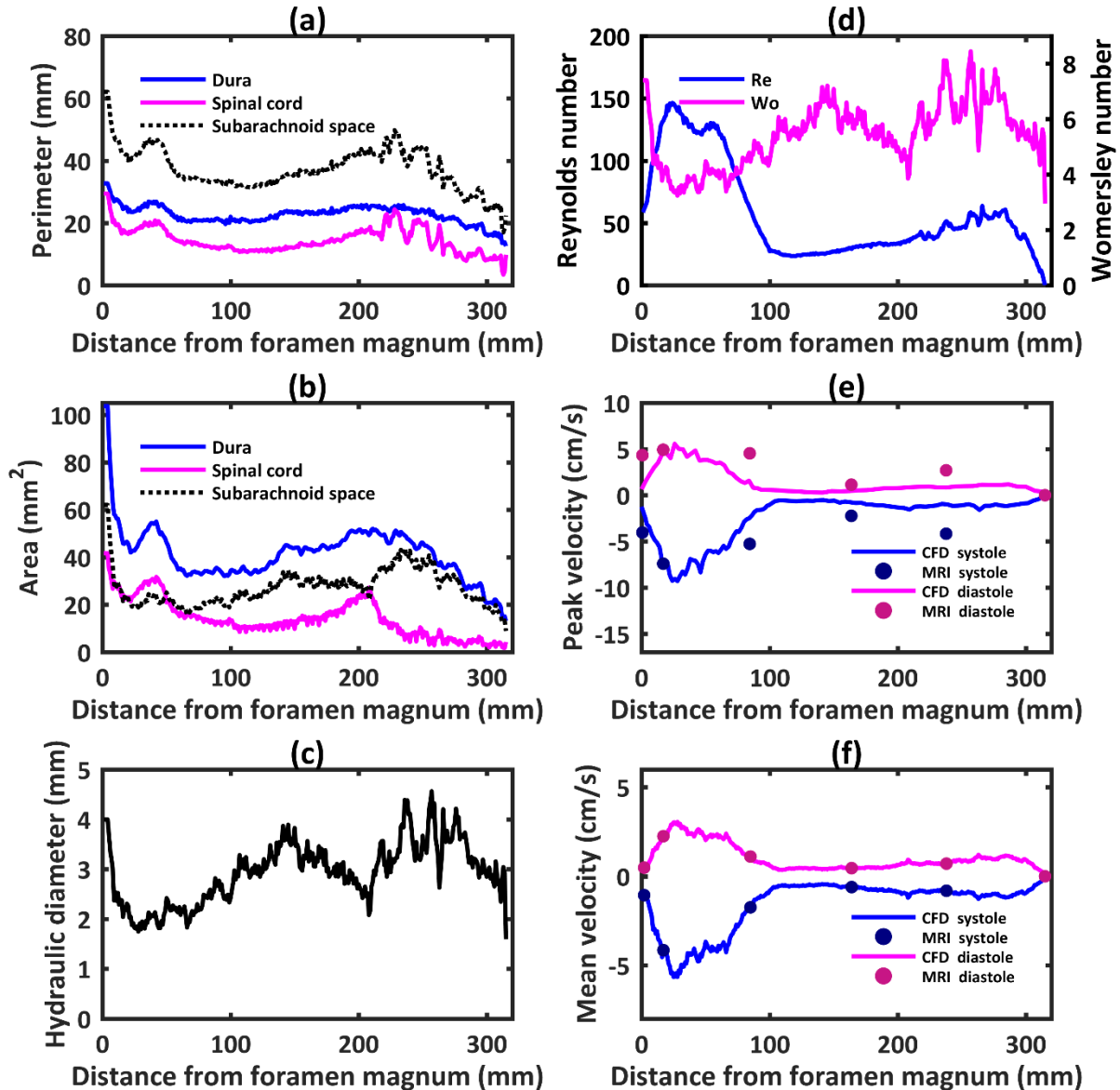


Figure 3.5. Hydrodynamic parameter distribution for the dura, spinal cord and subarachnoid space computed along the spine for a cynomolgus monkey in terms of: (a) perimeter, (b) cross-sectional area, (c) hydraulic diameter, (d) Reynold's number, Re and Womersley number, α . Comparison of CFD simulation (continuous line) and PCMRI measurements (dots) in terms of: (e) peak systolic and diastolic CSF velocity and (f) mean CSF velocity at peak systolic and diastolic flow.

CSF Flow

Maximum peak and mean CSF velocities in the numerical model were present at 28 mm (~C4-C5, Figure 5f). Minimum value of peak and mean CSF velocities occurred in the lower lumbar spine and within the thoracic spine from 108 to 141 mm (~T7-T10).

CSF flow oscillation had a decreasing magnitude and considerable variation in waveform shape along the spine (Figure 6a). Spatial temporal distribution of CSF flow rate along the SAS showed that

maximum CSF flow rate occurred caudal to C3-C4 at ~30 mm (Figure 6b). CSF flow rate waveform shape and magnitude was similar from ~125 mm to the SAS termination. CSF PWV was quantified to be 1.19 m/s (Figure 6b).

Comparison of mean velocity at peak systolic flow at the five MRI slice locations (Figure 5f) showed that MRI measurements were nearly identical to CFD results (error < 2.87%). Maximum percent difference in CFD versus MRI flow rate for all locations over the entire CSF flow cycle was 3.6% (Figure 6a). Maximum percent difference in CFD versus MRI flow rate at peak systole was ~2.8% (Table 5). Comparison of peak systolic and diastolic thru-plane CSF velocities at the five MRI slice locations (Figure 5e) indicated that the MRI measurements had from 1.03 – 3.59X greater peak velocities compared to CFD.

Table 3.5. Comparison of hydrodynamic CFD peak values with in vivo PCMRI measurements.

Parameter	Location	CFD	MRI	% error
Q_{peak-sys} (ml/s)	FM	-0.61	-0.60	1.10
	C2-C3	-1.02	-1.00	2.20
	T4-T5	-0.35	-0.35	2.10
	T10-T11	-0.19	-0.19	2.87
	L2-L3	-0.29	-0.29	0.60
Q_{peak-dia} (ml/s)	FM	0.25	0.26	1.87
	C2-C3	0.54	0.55	1.63
	T4-T5	0.22	0.22	1.39
	T10-T11	0.14	0.14	0.59
	L2-L3	0.24	0.24	1.29

V = Velocity, Q= CSF Flow rate, Peak-sys= Systolic peak flow, Peak-dia= Diastolic peak flow.

Dura Radial Displacement

Radial displacement of the dura over the cardiac cycle is depicted in Figure 6c. Three axial locations at 55, 162 and 268 mm had zero radial displacement over the cardiac cycle. Also, different segments of the dura, with the exception of the lower lumbar spine, showed general trends in either positive or negative displacement. Spatial-temporal distribution of dura radial displacement (Figure 6d) was different than CSF flow rate (Figure 6b).

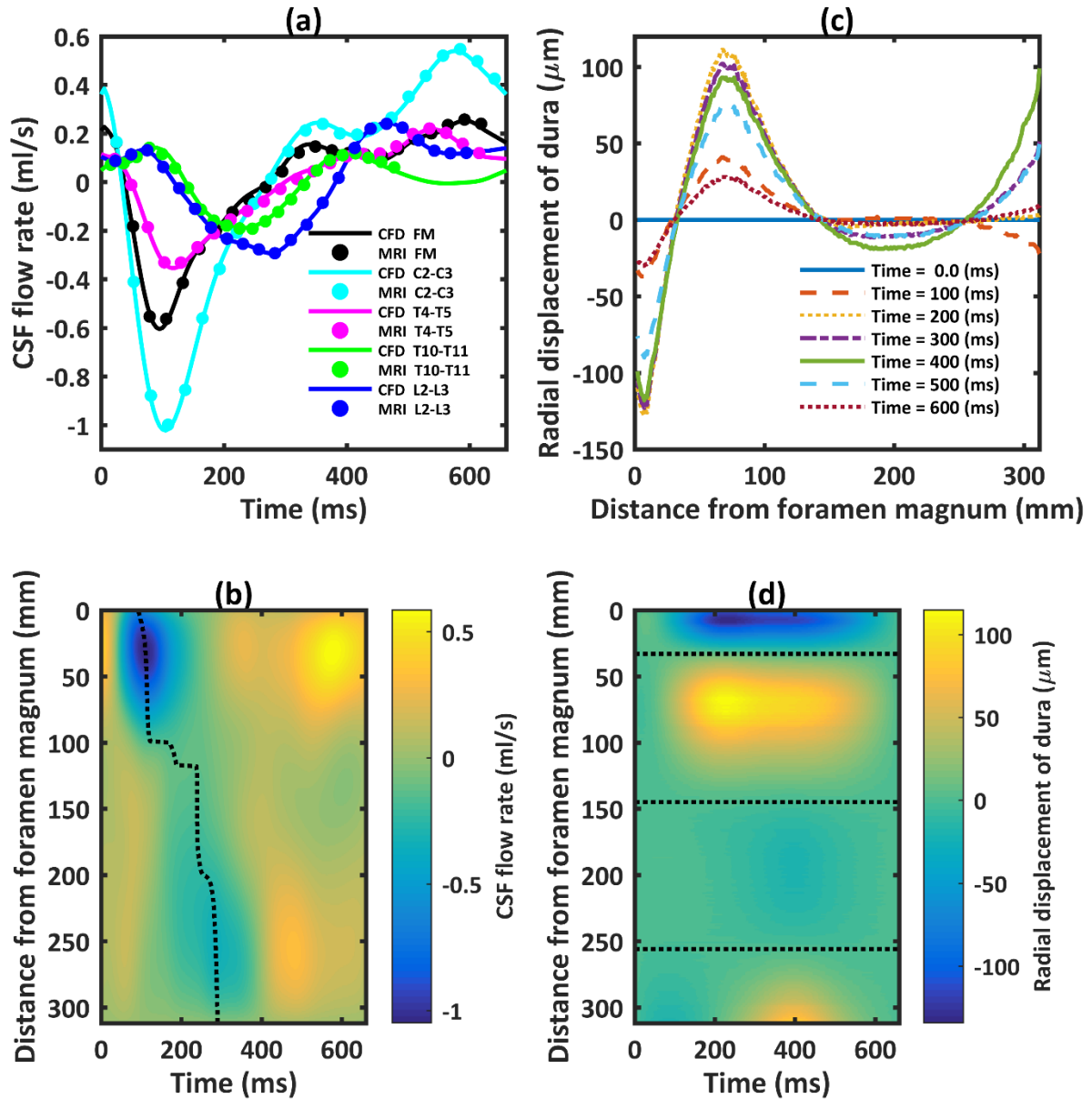


Figure 3.6. (a) CSF flow waveforms measured by PCMRI at five axial locations along the spine. Dots indicate experimental data and lines denote CFD results. Note: negative, or peak systolic, CSF flow is in the caudal direction. (b) Spatial-temporal distribution of the interpolated CSF flow rate along the spine. Dotted line indicates peak CSF flow rate at each axial level used to compute CSF pulse wave velocity (PWV). (c) Radial displacement of the dura surface at 100 ms intervals over the CSF flow cycle. (d) Spatial-temporal distribution of the dura radial displacement along the spine. Dotted line indicates the three locations along the spine with zero radial motion of the dura.

Comparison of CFD and in Vivo CSF Velocity Profiles

Visual inspection of the PCMRI and CFD thru-plane velocity profiles at peak systole revealed large spatial differences (Figures 7). Greater CSF velocities were observed by PCMRI in the anterior in comparison to the posterior space. In contrast, relatively uniform CSF flow profiles were simulated by CFD. All of the five sections showed CSF flow jets on PCMRI images. No such flow jets were present in the corresponding CFD velocity profiles. Epidural and vertebral artery blood flow was noted in the lumbar spine at L2-L3 and FM, respectively as denoted by the black arrows at those locations (Figure 7d). This flow was in close proximity to the CSF within the SAS and required omission in the MRI-based CSF flow waveform quantification.

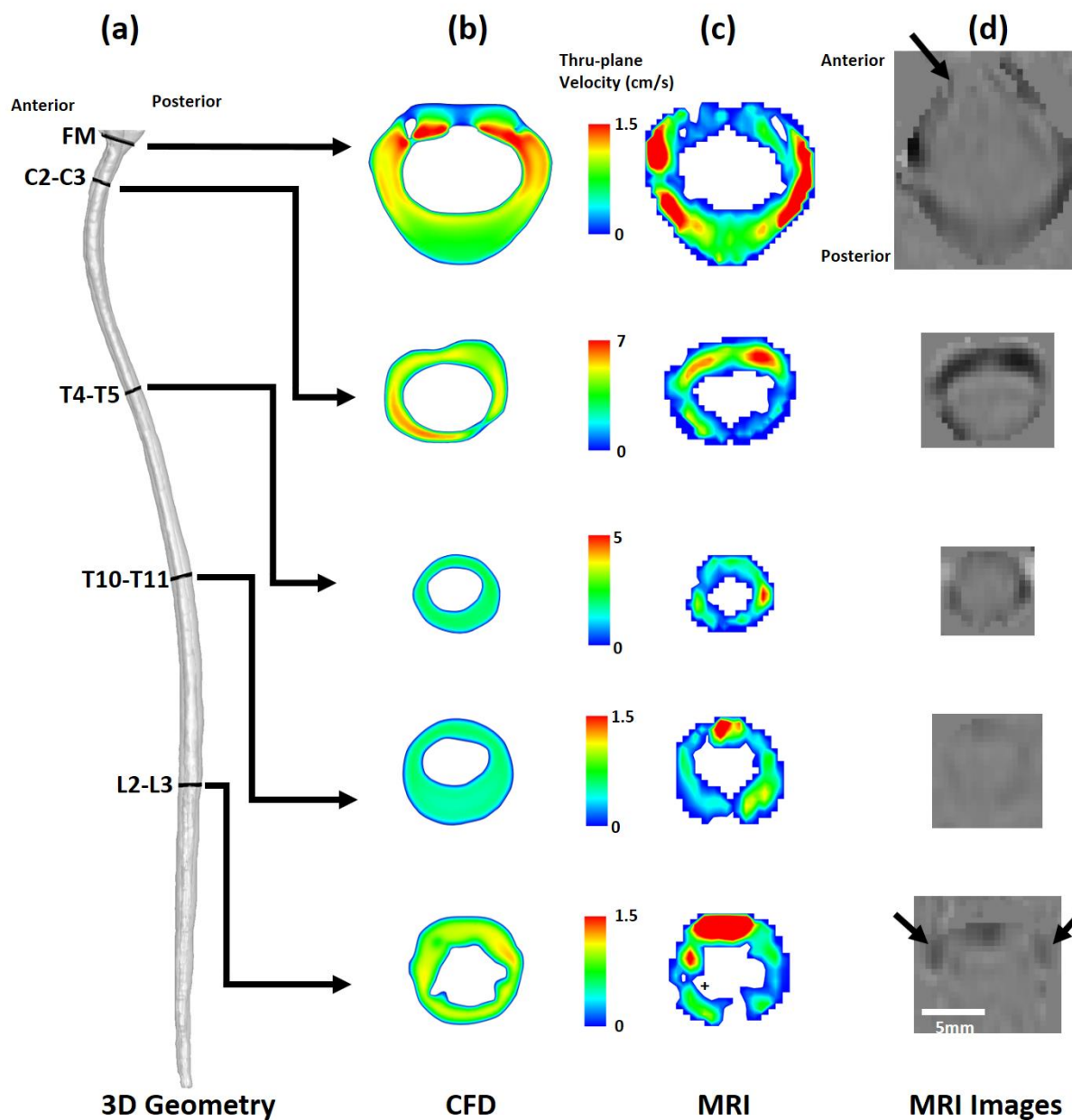


Figure 3.7. Peak-systolic thru-plane CSF velocity profiles simulated by CFD and measured by PCMRI for a cynomolgus monkey. (a) Overall view of the CFD model and slice locations. Note: different velocity scales are used at each slice location. (b) CSF velocity profiles at each slice location. (c) PCMRI visualization of CSF velocity profiles. (d) PCMRI gray scale images used to compute CSF flow waveforms. \uparrow symbols highlight nearby regions with PCMRI signal that are not within the CSF space ROI (epidural venous flow at L2-L3, and vertebral artery flow at the FM).

Discussion

The delivery of therapeutic agents to the CNS tissue by the CSF is dependent on the following four stages: (1) pulsation-dependent mixing of the CSF, (2) arterial pulsation assisted transport along the perivascular spaces, (3) absorption from the perivascular space to the CNS tissue and (4) extracellular transport and uptake into the neurons and along axons[56]. Each of these aspects must be understood to optimize CSF-based therapeutics. This study provides a flow model for accurate subject-specific reproduction of the non-uniform distribution of CSF flow along the entire spine using a non-uniform moving boundary approach. Results were verified by numerical independence studies and validated based on in vivo PCMRI measurements of CSF flow rates along the SAS.

Non-uniform CSF flow waveform reproduction

The distribution of CSF flow along the spine is non-uniform and shows local variations in waveform shape and magnitude (Figure 1b). For example, CSF flow waveform amplitude was smaller at the FM compared to C2-C3 and then decreased at T4-T5 (Figure 1b). Waveform amplitude was greater at L2-L3 compared to T10-T11. Thus, we implemented a non-uniform moving boundary approach to accurately reproduce the subject-specific MRI measurements. This involved an algorithm to compute local radial displacement of the dura (Figure 3) and nearby mesh elements. The resulting CSF flow rate waveforms were compared to the in vivo measurements and shown to be nearly identical over the entire CSF flow cycle (Figure 6a). In addition, comparison of mean velocity at peak systolic flow at the five MRI slice locations (Figure 5f) showed that MRI measurements were nearly identical to CFD results (error < 2.87% at peak systolic CSF flow). To our knowledge, this model represents the first validation of numerically modeled subject-specific CSF flow rates along the entire spine. Increasing the mesh resolution would decrease the degree of error and also increase simulation time. Additional simulation time and computing resources should be considered carefully with respect to the clinical problem and specific questions.

A number of previous studies have simulated CSF flow along the spine under varying levels of complexity. Tangen et al. [67] used a dynamic mesh to simulate an axially phase lagged version of the C4 CSF flow waveform measured by PCMRI. Agreement of CFD and MRI measurement of CSF flow rates at C4, T4 and L4 varied considerably depending on the axial location [67]. Another model by Sweetman et al. simulated CSF flow along the spine using a fluid-structure-interaction approach with prescribed material properties of the dura. This model predicted a decreasing trend in CSF flux along the spine. Kuttler et al. [68] completed a semi-idealized model of CSF flow along the entire spine using a moving grid approach. Martin et al. completed a 1-dimensional tube wave propagation model

of CSF flow along the spine [3]. Bertram [69], Elliott et al. [70], Cirovic et al. [71] and Lockey et al. [72], also completed wave propagation models under varying degrees of geometric complexity. For all of these models, CSF flow or pressure was imposed at the model inlet but not validated based on in vivo CSF flow measurements.

Comparison of CFD and in Vivo CSF Velocity Profiles

While the objective of our numerical modeling approach was to accurately reproduce the desired CSF flow rate distribution along the spine (Figure 6a), the numerical model did not result in identical CSF velocity profiles as the in vivo PCMRI measurements. PCMRI showed axial CSF velocity profiles to be non-uniform with presence of CSF flow jets and decreased CSF flow near nerve roots (Figure 6c). Similar findings have been reported by others in the literature [73]. CFD velocity profiles at the same locations were relatively uniform. A number of numerical studies of CSF flow in the cervical spine in humans also found that CSF velocity profiles did not match in vivo PCMRI measurements [73, 74]. In our study, agreement of peak CSF velocities was best at C2-C3 (error ~7%, Figure 5e). Maximum difference in peak CSF velocity at any location was 1.61 cm/s (Figure 5e). This level of difference is likely within the range of noise present in the PCMRI signal that was collected with a Velocity Encoding of 10 cm/s.

The differences in velocity profiles and peak velocities between the PCMRI measurements and CFD simulations suggest that the level of anatomical detail in CFD simulations is not adequate to accurately model the CSF velocity profiles. A study by Pahlavian et al. showed that the discrepancy in CFD and PCMRI velocity profiles is not due to PCMRI measurement noise [75] or neural tissue motion over the cardiac cycle [6]. Taken together, these studies indicate that relatively small structures within the CSF flow field alter the CSF flow velocity profiles [76].

Unfortunately, the current 3T MR image resolution does not allow accurate reproduction of these relatively small anatomical structures such as spinal cord nerve roots, dorsal and dorsal lateral septum, arachnoid trabeculae, denticulate ligaments and tiny blood vessels. These structures are likely the underlying reason for the differences in velocity profiles, in particular in the lower thoracic and lumbar spine (Figure 7c). MR image resolution must improve to define these features in the future, for example using 7T MRI [77]. Our geometric model did not include these small structures as they are not possible to image on a subject-specific basis. However, they should be included to accurately reproduce in vivo CSF flow profiles.

It is likely that accurate subject-specific reproduction of CSF flow rate distribution and velocity profiles is needed to model subject-specific intrathecal solute transport. Alternatively, one may choose to create idealized models with these structures included that can help inform intrathecal device design

and protocol development. In any case, these models should have accurate distribution of non-uniform CSF flow along the spine. Our approach satisfies that need.

CSF Space Geometry Quantification

To our knowledge, axial variation in spinal SAS geometry in terms of A_{cs} , P_{cs} and D_H in a cynomolgus monkey has not been reported in the literature. This is likely due to the relatively long time period (55 minutes total) required to obtain the high-resolution MRI images (375 μm isotopic) used to segment the CSF space in this study. Hydraulic diameter ranged from $\sim 1.5\text{-}4.5$ mm in the NHP analyzed. The axial distribution of SAS geometry in the cynomolgus monkey had a similar trend as that quantified in humans for A_{cs} , P_{cs} and D_H [59], albeit approximately ~ 7.4 , 2.3 and 2.4X smaller, respectively in magnitude compared to a human [64]. Total CSF volume in the spine for the cynomolgus monkey in this study was ~ 8.7 ml. Based on Loth et al., human spinal CSF volume can be estimated to be ~ 125 ml. Detailed MR investigation of the complete spinal CSF space in terms of its geometry is lacking in the literature.

Importance of Hydrodynamic Parameters

The analysis of Reynold's and Womersley numbers is helpful to compare the present study results with the literature and validate the CFD methodology assumptions, such as laminar flow. Using the peak CSF flow rate and hydraulic diameter, Re , did not exceed 150 for any axial location along the NHP spine (Figure 5d). Re for the NHP analyzed in our study was consistent with previous findings for humans that quantified Re to range from ~ 150 to 450 [64]. In the present study, Re was significantly lower than the critical value for transition to turbulence for flow in a straight circular pipe and thus, we expect the flow to be laminar throughout the SAS. However, a study by Helgeland et al. indicated that CSF flow may have instabilities [78]. The phase-contrast MRI measurements used to detect the CSF velocity profiles in our study were time-averaged over multiple cardiac cycles. Thus, any unsteadiness in pixel velocities that could be due to flow instability was not possible to detect.

Our findings indicated that maximum Re was present at C4-C5. This location may be best suited for intrathecal delivery of solutes [56]. However, intrathecal drug delivery at C4-C5 may have increased risk for CNS tissue damage in comparison to the typical delivery location in the lumbar spine. It is unclear if this location would be the same for humans, as little information is known about CSF flow rates along the entire spine in humans.

Womersley number, α , ranged from ~ 3 to 8, suggesting that transient inertial forces were dominant over viscous forces. These findings are in agreement with the range of Womersley numbers for CSF flow in humans[60]. They also indicate that viscous effects within the spinal SAS are relatively insignificant as documented by Loth et al. [64].

CSF Pulse Wave Velocity Along the Spine (PWV)

Spatial-temporal smoothing of the in vivo measured CSF flow rate waveforms showed that the CSF flow has a distinguishable wave propagation velocity (PWV) along the SAS of approximately 1.19 m/s (Figure 6b). This PWV is lower than previously reported in the literature for humans, albeit, the number of in vivo studies is limited. An in vivo study by Kalata et al. used high-speed PCMRI to quantify the CSF velocity wave speed in a ~ 20 cm portion of the cervical spine and found it to be 4.6 ± 1.7 m/s at systole in healthy subjects [66]. A fluid-structure-interaction study by Sweetman et al. predicted spinal CSF PWV to be ~ 3 m/s [79]. Another simulation by Martin et al. used a numerical 1-D tube model of the spinal SAS to parametrically alter the dura mechanical properties and analyze the effect on spinal CSF flow and pressures[80]. In that study, CSF PWV varied from 2.5 to 13.5 m/s depending on dura elasticity. Martin et al. also investigated CSF wave phenomena in the spine using in vitro models and found CSF wave reflections to be present [3]. Similar findings have been found numerically by a number of investigators using a number of approaches [69, 81]. Our results did not show a large degree of CSF wave reflection within the spine (Figure 6b). More detailed investigation is needed to understand CSF PWV in the spine and its relevance, if any, to CNS disease pathophysiology and intrathecal therapeutics.

Motion of the Dura

To our knowledge, radial motion of the dura has not been directly measured along the spine using MR imaging, likely due to the relatively small degree of motion present in that tissue. Our results indicate that a maximum radial dura displacement of ~ 135 μm (Figure 6c) is sufficient to reproduce the measured CSF flow rates along the NHP spine (Figure 6a). Interestingly, there were three axial locations along the spine that did not have dura radial displacement (Figure 6d, dotted lines). The location of maximum dura displacement was at the T3-T4 and C1-C2 vertebral level (Table 3). These locations had a positive and negative displacement from baseline, respectively. Maximum CSF flow rate was present between these two locations at approximately C3-C4. CSF flow wave propagation and dura displacement did not appear to be coupled in terms of their spatial temporal distribution (compare Figure 6c and d).

Limitation

The numerical modeling methods in this study were based on MRI measurements for a single cynomolgus monkey. Geometric and hydrodynamic findings were presented to understand the hydrodynamic environment. These parameters should be investigated in a larger group of NHPs to determine their statistical variance with gender, among NHP species and comparison to humans.

A single operator accomplished geometric segmentation of the MRI images used in this study. A study by Martin et al. indicated a high-degree of reliability in CFD results for geometries produced by different operators [60]. We therefore expect the trends in CSF dynamics and geometry to be similar given a different operator. Non-uniform motion of the numerical mesh was defined by the measured CSF flow rate using a manual ROI selection. Careful attention was given to omit regions outside of the SAS by referencing the high-resolution T2-weighted image sets (e.g. for omission of epidural venous flow around the dura). Pixels with net flow in one direction were omitted (blood flow), pixels with oscillatory flow were included (CSF). Nevertheless, in some cases it was difficult to distinguish CSF flow from nearby epidural flow that may pulsate.

Our modeling approach did not include CSF within the SAS of the brain or ventricles because we did not have MR images of flow or geometry obtained within those regions for validation of the numerical model. These images were not possible to collect in the already relatively long 1 hour and 21 minute MRI measurement timeframe. Additionally, the presented model used a moving boundary method in which boundary motion was prescribed at the model wall. This model did not account for fluid structure interaction of the wall (tissues) and fluid. Prescribed motion of the dura allowed reproduction of the in vivo measured CSF flow rate.

Conclusion

This study presents a flow model based on a non-uniform moving boundary method to accurately reproduce in vivo CSF flow rate distribution and waveform along the spinal SAS of a cynomolgus monkey. Maximum error measured at peak CSF flow rate in the numerical model was <3.6%. Deformation of the dura ranged up to a maximum of 135 μm . MRI measurements of CSF space geometry and flow were successfully acquired to define the numerical domain and boundary conditions. For the single cynomolgus monkey analyzed, results showed that CSF flow was laminar with a peak Reynold's number of ~ 150 and average Womersley number of ~ 5.4 . Geometric analysis indicated that total spinal CSF space volume was ~ 8.7 ml. Average hydraulic diameter, wetted perimeter and SAS area was 2.9 mm, 37.3 mm and 27.2 mm^2 , respectively. CSF PWV along the spine was quantified to be 1.2 m/s and did not appear to have a significant degree of wave reflection at the spine termination.

Maximum CSF flow movement was present at the C4-C5 vertebral level. In combination, these results represent the first CFD simulation of spinal CSF hydrodynamics in a monkey.

Chapter 4: Characterization of intrathecal cerebrospinal fluid geometry and dynamics in cynomolgus monkeys (*Macaca fascicularis*) by magnetic resonance imaging

Abstract

Recent advancements have been made toward understanding the diagnostic and therapeutic potential of cerebrospinal fluid (CSF) and related hydrodynamics. Increased understanding of CSF dynamics may lead to improved detection of central nervous system (CNS) diseases and optimized delivery of CSF based CNS therapeutics, with many proposed therapeutics hoping to successfully treat or cure debilitating neurological conditions. Before significant strides can be made toward the research and development of interventions designed for human use, additional research must be carried out with representative subjects such as non-human primates (NHP). This study presents a geometric and hydrodynamic characterization of CSF in eight cynomolgus monkeys (*Macaca fascicularis*) at baseline and two-week follow-up.

Results showed that CSF flow along the entire spine was laminar with a Reynolds number ranging up to 80 and average Womersley number ranging from 4.1-7.7. Maximum CSF flow rate occurred ~25 mm caudal to the foramen magnum. Peak CSF flow rate ranged from 0.3-0.6 ml/s at the C3-C4 level. Geometric analysis indicated that average intrathecal CSF volume below the foramen magnum was 7.4 ml. The average surface area of the spinal cord and dura was 44.7 and 66.7 cm² respectively. Subarachnoid space cross-sectional area and hydraulic diameter ranged from 7-75 mm² and 2-3.7 mm, respectively. Stroke volume had the greatest value of 0.14 ml at an axial location corresponding to C3-C4.

Introduction

Cerebrospinal fluid (CSF) is a clear, colorless fluid with water-like mechanical properties that bathes the entire brain and spinal cord. CSF plays a role in the protection of neural structures, metabolic homeostasis of the central nervous system (CNS), autoregulation of cerebral blood flow, and immunological support for neural tissue. CSF moves freely in an oscillatory manner with approximately zero net flow, and in synchrony with cardiac-related intracranial pulsations and respiration [82-86]. Recent advances have been made toward understanding the diagnostic and therapeutic potential of CSF and related hydrodynamics. Increased understanding of CSF dynamics may lead to improved detection

of CNS diseases, development of CSF system-based intrathecal drug delivery, and improved treatment of debilitating neurological conditions.

The importance of CSF dynamics has been investigated in several CNS conditions including syringomyelia [47] Alzheimer's disease [87], Chiari malformation [88], and hydrocephalus [89]. Researchers have also applied computational fluid dynamics modeling approaches to understand how CSF dynamics related parameters could relate to CNS disease states and intrathecal drug delivery [18, 90-93]. Before significant strides can be made toward the research and development of interventions designed for human consumption, additional research must be carried out with representative subjects such as non-human primates (NHP). However, relatively little information is known regarding CSF geometry and hydrodynamics in NHPs.

Studies have examined the possible role of CSF as a conduit for distribution of radiolabeled tracers [94] and therapeutic molecules to neuronal and glial cells of CNS tissues [40, 95]. Intrathecal delivery of these molecules directly to the CNS tissue [83] is, in part, dependent on pulsation-dependent mixing of the spinal CSF dynamics. A solute injected into the CSF mixes [40], spreads throughout the CSF system, and is then taken up into the brain parenchyma via the perivascular (Virchow-Robbin) spaces [57, 96]. Molecule injection to the CSF bypasses the blood-brain-barrier and allows delivery of many molecules that may not be possible through the systemic system [97, 98]. The direct contact of CSF with neural tissue can enable delivery of small molecules to biologics including protein, cell-based, viral-mediated gene transfer, and gene therapies involving trophic factors to stimulate dying neurons [99, 100]. These therapies have shown promise in animal studies [101, 102] and safety in human clinical trials [103]. In addition, delivery in the CSF is a minimally invasive surgical intervention with a lower risk to the patient than other surgical interventions such as convection enhanced drug delivery and deep brain stimulation [102, 104, 105].

While intrathecal delivery of drugs or biologics to the CNS offers a promising treatment option, the dearth of knowledge has slowed therapeutic development and potentially confounded the analysis of therapeutic effectiveness. A common animal model used to test intrathecal therapeutics is the NHP, with one of the most common species being the cynomolgus monkey (*Macaca fascicularis*). Cynomolgus monkeys are a useful model for such studies since they are relatively compact compared to other NHP species, and share physiologic and cognitive similarities to humans. Despite being a frequently studied species, CSF hydrodynamic properties have not been studied or reported. At present, we do not know how NHP CSF hydrodynamics compare to humans or if they are consistent across animals and/or over time. The aim of the present study was to a) develop an MRI-based method to quantify intrathecal CSF dynamics in cynomolgus NHPs, b) use this method to quantify intrathecal

CSF dynamics and geometry in a series of NHPs (N=8), and c) measure the reliability of MRI-derived measures over a 2-week time interval.

Methods and Materials

Ethics Statement

This study was submitted to and approved by the local governing Institutional Animal Care and Use Committee at Northern Biomedical Research (IACUC approval #084-014A, Spring Lake, MI). This study did not unnecessarily duplicate previous experiments and alternatives to the use of live animals were considered. Procedures used in this study were designed with the consideration of the well-being of the animals.

Animals

MRI measurements were obtained for eight (NHP 01-08) healthy five-year-old adult cynomolgus monkeys (*Macaca fascicularis*, origin Mauritius) from Charles River Research Models, Houston TX with a weight of 4.4 ± 1.2 kg (mean \pm standard deviation). NHP 01 was male. All other NHPs were female (02-08). These animals were purpose-bred and experimentally naïve. Each NHP was scanned with an identical protocol at baseline and at follow-up after a 2-week time interval.

MRI scan Protocols

All MRI measurements were acquired at Northern Biomedical Research (Muskegon, Michigan, U.S.A.) on a Philips 3T scanner (Achieva, software V2.6.3.7, Best, The Netherlands). Prior to MRI scanning each NHP was prepared using standard procedures and precautions. NHPs were positioned in the scanner in the supine position without assistance from artificial respiration. During each scan, heart rate and respiration was monitored continuously with ~ 1 liter/minute of oxygen and 1-3% isoflurane anesthetic administered via endotracheal tube for sedation.

Anatomic MRI Scan Protocol for CSF Space Geometry Quantification

Total scan time to quantify CSF space geometry and flow (including NHP MRI preparation) for each NHP was ~ 1 hour after the protocols were in place. A stack of high-resolution axial T2-weighted MR images of the complete spinal subarachnoid space (SAS) geometry was acquired for each NHP using a VISTA (31 minutes) protocol (**Table 1**). The anatomical region scanned was ~ 30 cm in length, which included the intrathecal SAS below the lower brain stem extending caudally to the filum

terminale. This comprised a total of ~720 images with 0.5 mm slice spacing, 1.0 mm slice thickness, and 0.375 mm isotropic in-plane resolution.

Table 4.1. Anatomic (T2-VISTA) and CSF flow (phase-contrast MRI) scan protocol parameters used for imaging cynomolgus monkeys.

Parameter	Anatomic (T2-VISTA)	CSF Flow (PC-MRI)
File size	941 MB	7 MB
Acquisition contrast	T2	Flow encoded
Acquisition type	3D	2D
Slice Thickness	1 mm	5 mm
Slice spacing	0.5 mm	N/A
Pixel bandwidth	481	192
Pulse Sequence	TSE	TFE
Transmit coil	Body	Body
Duration	31 minutes	200 – 240 seconds
Number of slices	660	N/A
Image matrix	864 x 864	224 x 224
In-plane resolution	0.375 mm	0.446 mm
Repetition time	2000 (ms)	11.226 – 12.704 (ms)
Echo Time	120 (ms)	6.749 – 8.226 (ms)
Cardiac phases	N/A	24
R-R interval	N/A	454 - 653 ms
Encoding direction	N/A	Thru-plane
Plane orientation	Sagittal	Axial
Trigger	N/A	Retrospective ECG
Velocity encoding	N/A	5 at FM and L4; 10 elsewhere

Phase-contrast MRI Scan Protocol for CSF Flow Quantification

Thru-plane (head-foot, z-direction) CSF flow was measured by phase-contrast MRI (PC-MRI) images collected at six axial locations along the spine for each NHP. Axial locations were located at the foramen magnum (FM), C2-C3, C5-C6, T4-T5, T10-T11, and L3-L4 and required ~3 minutes scan time per location. Flow images were acquired with a retrospective ECG triggered sequence with 24 heart phases, 0.45 mm isotropic in plane resolution, and 5 mm slice thickness (**Table 1**). Slice location for each scan was oriented approximately perpendicular to the CSF flow direction with slice planes intersecting vertebral discs. More details on the PC-MRI protocol are given in Martin et al. [59].

3D Image Segmentation

The high-resolution T2-weighted anatomic MRI images were semi-automatically segmented using the free open-source ITK-snap software (Version 3.0.0, University of Pennsylvania, U.S.A.) [106], which provided semi-automatic segmentation using active contour methods, as well as manual delineation and image navigation (**Fig 1**). The manual segmentation tool was used most frequently with view of the three orthogonal planes. Detailed information on the segmentation procedure is provided by Martin et al. [107]. Once the segmentation was complete, the 3D model was exported in a .STL (Stereo Lithography) format for subsequent analysis as outlined below.

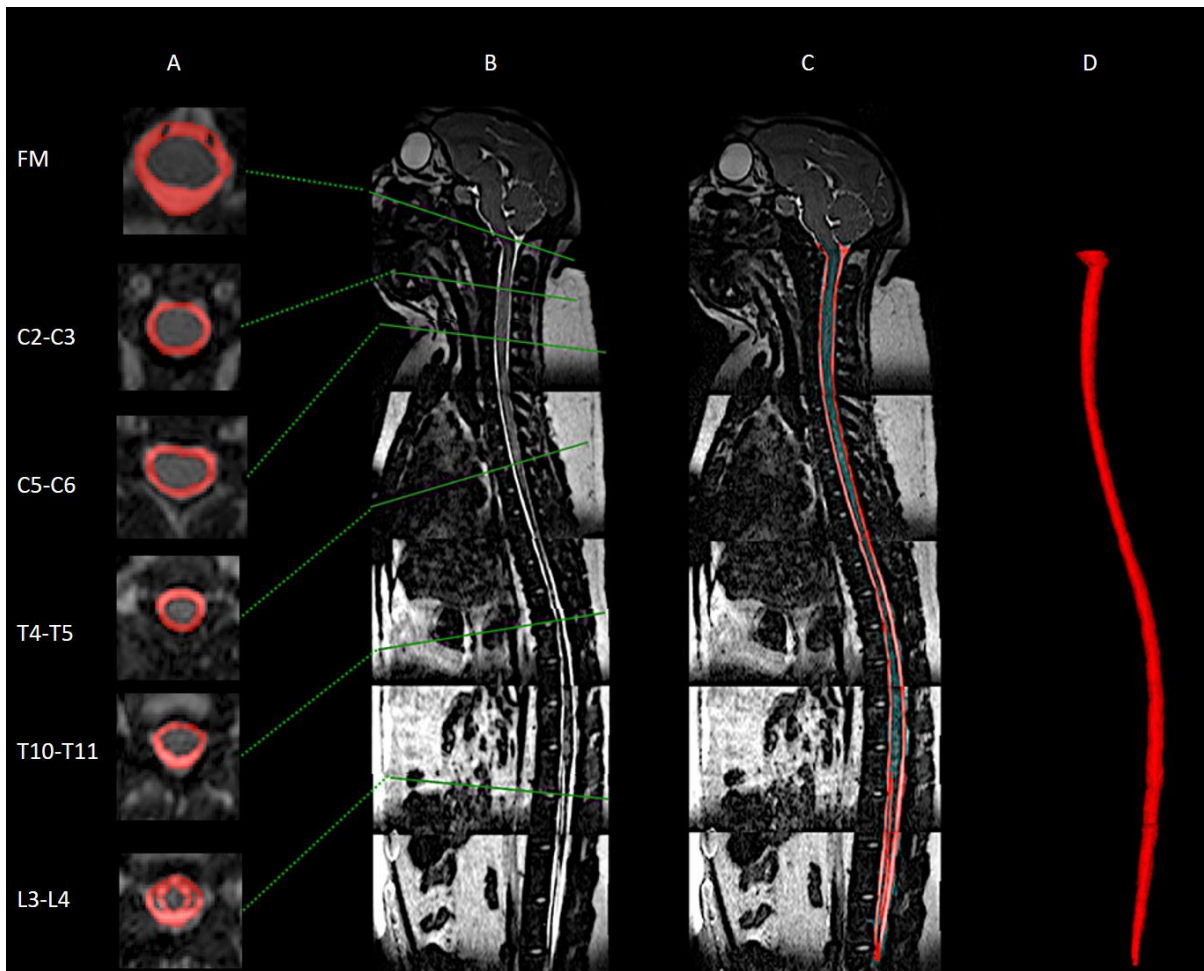


Figure 4.1. Manual segmentation of the spinal subarachnoid space using a T2-weighted MR image for a cynomolgus monkey analyzed in this study. (A) Visualization of SAS area manually selected around the spinal cord at multiple axial levels. (B) Mid-sagittal high-resolution T2-weighted MRI. (C) Sagittal visualization of segmented SAS around the spinal cord. (D) 3D visualization of entire SAS geometry. The same methods were applied to all MR images obtained for all NHPs.

CSF Flow Waveform and Profile Analysis

CSF flow was quantified at six axial locations along the spine (**Fig 2**) using GTFLOW software (64-bit, Version 2.2.10, Gyrotools, Zurich, Switzerland) by the following procedure previously described in [107]. PC-MRI and corresponding magnitude images were loaded into GTFLOW. A region of interest (ROI) was created within the area of CSF flow between the dura and spinal cord (**Fig 2A**). Individual pixel velocities within each ROI were exported to a .CSV (Comma-Separated Values) file for further analysis using MATLAB software (Ver. R2016a Mathworks Corp., Natick, MA). CSF

flow waveform within the ROI, $Q(t)$, was computed with $Q(t) = \sum A_{pixel} V_{pixel}(t)$, where A_{pixel} is the area of one MRI pixel, $V_{pixel}(t)$ is the velocity for the corresponding pixel at any time, and $Q(t)$ is the summation of the flow for each pixel within the ROI. The CSF flow waveform was offset to ensure zero net flow over the flow cycle since CSF flow in the spine has approximately zero net flow (oscillatory).

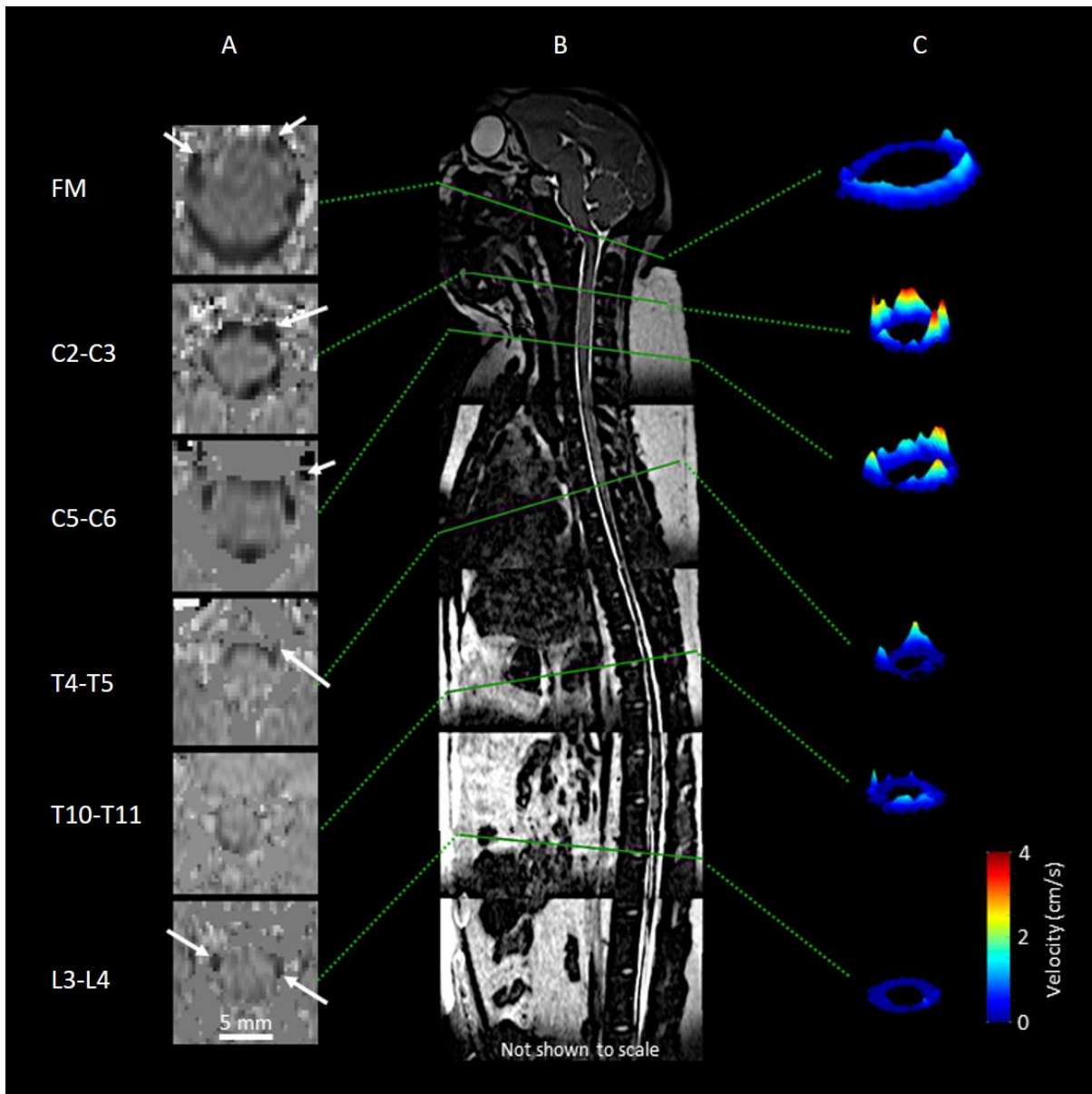


Figure 4.2. Axial PC-MRI and CSF velocity profiles at corresponding vertebral levels for a cynomolgus monkey in this study. (A) PC-MRI axial cross-sections for a given case at each respective vertebral level. (B) T2-weighted MR image of a cynomolgus monkey in the study with corresponding PC-MRI axial locations and slice orientation (solid green lines) at FM, C2-C3, C5-C6, T4-T5, T11-T12, and L3-L4. (C) 3D visualization of peak systolic CSF velocity profiles based on in vivo PC-MRI measurements at each vertebral level.

The following method was applied to generate a smooth spatial-temporal CSF flow distribution, $Q(z,t)$, along the spine. The axial phase-contrast slice locations were not identical for each NHP due to differences of the exact vertebral levels across cases. Thus, the z-location of each slice was manually measured based on the distance of that slice caudal to the FM (**Table 2**). The six distinct

flow rates were smoothed in a spatial-temporal fashion using MATLAB and a 2D “fit” function with the fit-type designated as “smoothing-spline”. Since heart rate variability was present between the PC-MRI scans, the CSF flow waveform timing was normalized to the average heart rate for all NHPs. An average spatial-temporal CSF waveform was determined. CSF pulse wave velocity, PWV , was computed based on the slope of the arrival time of peak CSF flow along the spine [66].

Table 4.2. Reference chart for vertebral disk location with respect to axial distance from the foramen magnum in cynomolgus monkeys.

Vertebral level	Mean \pm std (mm)
'FM'	0.0 \pm 0.0
'C1'	5.7 \pm 2.4
'C2'	10.3 \pm 2.6
'C3'	22.3 \pm 3.9
'C4'	29.0 \pm 3.6
'C5'	35.2 \pm 3.8
'C6'	42.2 \pm 3.4
'C7'	48.7 \pm 3.8
'T1'	56.1 \pm 4.2
'T2'	63.4 \pm 4.4
'T3'	72.0 \pm 4.2
'T4'	79.8 \pm 4.2
'T5'	88.5 \pm 4.5
'T6'	97.9 \pm 4.9
'T7'	107.4 \pm 4.5
'T8'	117.6 \pm 4.8
'T9'	128.8 \pm 4.5
'T10'	141.4 \pm 5.4
'T11'	156.3 \pm 5.0
'T12'	172.0 \pm 5.1
'L1'	189.6 \pm 5.4
'L2'	207.5 \pm 5.8
'L3'	227.1 \pm 6.8
'L4'	247.0 \pm 7.0
'L5'	268.9 \pm 6.2
'Sacrum'	289.4 \pm 6.7
'coccyx'	301.0 \pm 6.8

FM = Foramen magnum, C= Cervical, T= Thoracic, L= Lumbar

Geometric and Hydrodynamic Parameter Quantification

Several geometric and hydrodynamic parameters were calculated based on the 3D segmentation and flow analysis using our previously published methods [91]. Using the exported 3D .STL file (above), each of these parameters was calculated by a user-defined function (UDF) compiled in ANSYS FLUENT (ANSYS® Academic Research, Release 19.1, Canonsburg, PA, USA) based on a computational mesh generated from ANSYS ICEM (ANSYS® Academic Research, Release 19.1, Canonsburg, PA, USA). Details on the methods used to generate each parameter are as follows.

The following parameters were computed based on overall spine geometry: Total SAS surface area, SA_{sas} , was calculated as the sum of surface area of spinal cord, SA_c , and dura, SA_d . Spinal cord nerve roots were not included in the surface area calculation of the cord since these small features were not possible to accurately visualize by MR imaging. Total volume of the SAS, V_{sas} , was computed by subtracting the volume of the spinal cord, V_c from the volume of the dura, V_d . An overall average, maximum, and minimum value was then computed across all NHPs. Total SAS length, L_{sas} , from the FM to the SAS termination was quantified.

The following parameters were determined for each 1 mm interval along the spine (z-location): Axial distribution of the SAS cross-sectional area, $A_{sas}(z)$, was based on cross-sectional area of the spinal cord at that location, $A_c(z)$, and dura, $A_d(z)$. Similarly, hydraulic diameter, $D_h(z) = 4A_{sas}(z) / P_{sas}(z)$, was determined based on the wetted perimeter, $P_{sas}(z)$, with the perimeter computed as the sum of the spinal cord, $P_c(z)$, and dura, $P_d(z)$, perimeters at each z-location. Axial distribution of CSF stroke volume was computed as $SV(z) = \int |Q(z,t)| dt$, where $|Q(z,t)|$ is the absolute value [73]. Peak systolic (toward feet) and diastolic (toward head) CSF flow rate was quantified as $Q_{sys}(z)$ and $Q_{dia}(z)$, and the CSF flow rate amplitude was given by $Q_a(z) = Q_{dia}(z) - Q_{sys}(z)$. Spatial mean thru-plane velocity at peak systole was computed as $\bar{U}_{sys}(z) = Q_{sys}(z) / A_{sas}(z)$ and at diastole as $\bar{U}_{dia}(z) = Q_{dia}(z) / A_{sas}(z)$. Reynolds number was computed as $Re(z) = (\bar{U}_{sys}(z) \cdot D_h(z)) / \nu$, where ν is the kinematic viscosity of CSF at body

temperature, 0.693 mPa·s [59]. Womersley number was computed as $\alpha(z) = \frac{D_h(z)}{2} \sqrt{\omega/\nu}$, where ω is the angular velocity ($\omega = 2\pi/T$) of the volume flow waveform with T equal to the heart rate.

To allow parameter comparison across NHPs, each parameter's axial distribution for each NHP was normalized to the average L_{sas} measured for all NHPs. After normalization, the mean axial distribution for each parameter was computed across all NHPs. The mean axial distribution was then used to obtain an average, maximum, and minimum parameter value along the spine based on all NHPs.

Parameter Reliability

Reliability was assessed by obtaining MRI measurements for each NHP at baseline and 2-week follow-up while ensuring identical methods during both collection intervals. To quantify measurement reliability, we performed a regression of baseline versus follow-up parameters computed at each axial location along the spine. All computations and plots were generated using MATLAB software (Ver. R2016a Mathworks Corp., Natick, MA).

Results

Results were obtained for a total of eight NHPs at baseline and a 2-week follow-up time point (Table 3). Overall, the MRI protocol allowed quantification of all proposed geometric and hydrodynamic parameters. These parameters had a relatively similar axial distribution across all NHPs analyzed and were similar at follow-up for each NHP. CSF flow was laminar in all NHPs with the greatest degree of CSF motion observed in the cervical spine. Average results showed that maximum Re and α was 80 and 7.7, respectively. A_{sas} and D_h ranged from 7-75 mm² and 2 - 3.7 mm, respectively. Maximum \bar{U}_{sys} and \bar{U}_{dia} was -2.7 to 1.6 cm/s and located in the cervical spine. SV ranged from 0.14 ml in the cervical spine to roughly 0 ml in the lower lumbar spine for all NHPs.

Table 4.3. Summary of geometric and hydrodynamic results. Mean values correspond to the average along the entire spine for all 16 NHPs (except for total surface area, volume, and PWV). Local maximum and minimum values are computed based the average for all 16 NHPs (solid lines in Fig 6).

Parameter	Symbol	Unit	Average	Maximum	Minimum
<i>Parameters computed at 1 mm intervals along the spine</i>					
<i>Perimeter of spinal cord</i>	P_c	<i>mm</i>	14.77	62.02	0.73
<i>Perimeter of dura</i>	P_d	<i>mm</i>	22.06	38.63	9.54
<i>Perimeter of subarachnoid space</i>	P_{sas}	<i>mm</i>	36.82	99.56	10.50
<i>Area of spinal cord</i>	A_c	mm^2	15.05	81.50	0.50
<i>Area of dura</i>	A_d	mm^2	39.59	137.45	7.61
<i>Area subarachnoid space</i>	A_{sas}	mm^2	24.54	75.10	6.98
<i>Hydraulic diameter</i>	D_h	<i>mm</i>	2.68	3.73	2.02
<i>Reynolds number</i>	Re	<i>NA</i>	29.30	79.27	0.66
<i>Womersley number</i>	α	<i>NA</i>	5.50	7.67	4.15
<i>Mean velocity at peak systole</i>	\bar{U}_{sys}	<i>cm/s</i>	-0.83	-0.02	-2.69
<i>Mean velocity at peak diastole</i>	\bar{U}_{dia}	<i>cm/s</i>	0.58	1.59	0.02
<i>Flow rate at peak systole</i>	Q_{sys}	<i>ml/s</i>	-0.20	0.00	-0.60
<i>Flow rate at peak diastole</i>	Q_{dia}	<i>ml/s</i>	0.14	0.35	0.00
<i>Flow rate amplitude</i>	Q_a	<i>ml/s</i>	0.33	0.94	0.00
<i>Stroke volume</i>	SV	<i>ml</i>	0.05	0.14	0.00
<i>Parameters computed based on the entire spine</i>					
<i>Surface area of spinal cord</i>	SA_c	cm^2	44.74	49.63	37.76
<i>Surface area of dura</i>	SA_d	cm^2	66.66	70.49	60.53
<i>Surface area of subarachnoid space</i>	SA_{sas}	cm^2	111.39	120.12	98.31
<i>Volume of spinal cord</i>	V_c	<i>ml</i>	4.57	5.40	3.98
<i>Volume of Dura</i>	V_d	<i>ml</i>	11.99	13.45	10.25
<i>Volume of subarachnoid space</i>	V_{sas}	<i>ml</i>	7.41	8.47	6.24
<i>Length of subarachnoid space</i>	L_{sas}	<i>mm</i>	301	306.98	295.80
<i>Pulse wave velocity</i>	PWV	<i>m/s</i>	1.13	3.45	0.73

Geometric Parameters

Average V_{sas} for all NHPs was 7.41 ml. Average SA_c and SA_d was 44.74 ± 3.52 and 66.66 ± 3.11 cm^2 respectively. A_{sas} and D_h decreased moving caudally down the spinal cord from the FM (**Fig 3**). The minimum value for A_{sas} and D_h was 7 mm^2 and 2 mm, respectively (**Table 3**). These values occurred at ~ 70 mm caudal to the FM, a location approximately corresponding to T2-T3 (**Table 2**). Maximum difference in A_{sas} and D_h between NHPs at any axial location (omitting the FM) was ~ 30 mm^2 and 4 mm, respectively.

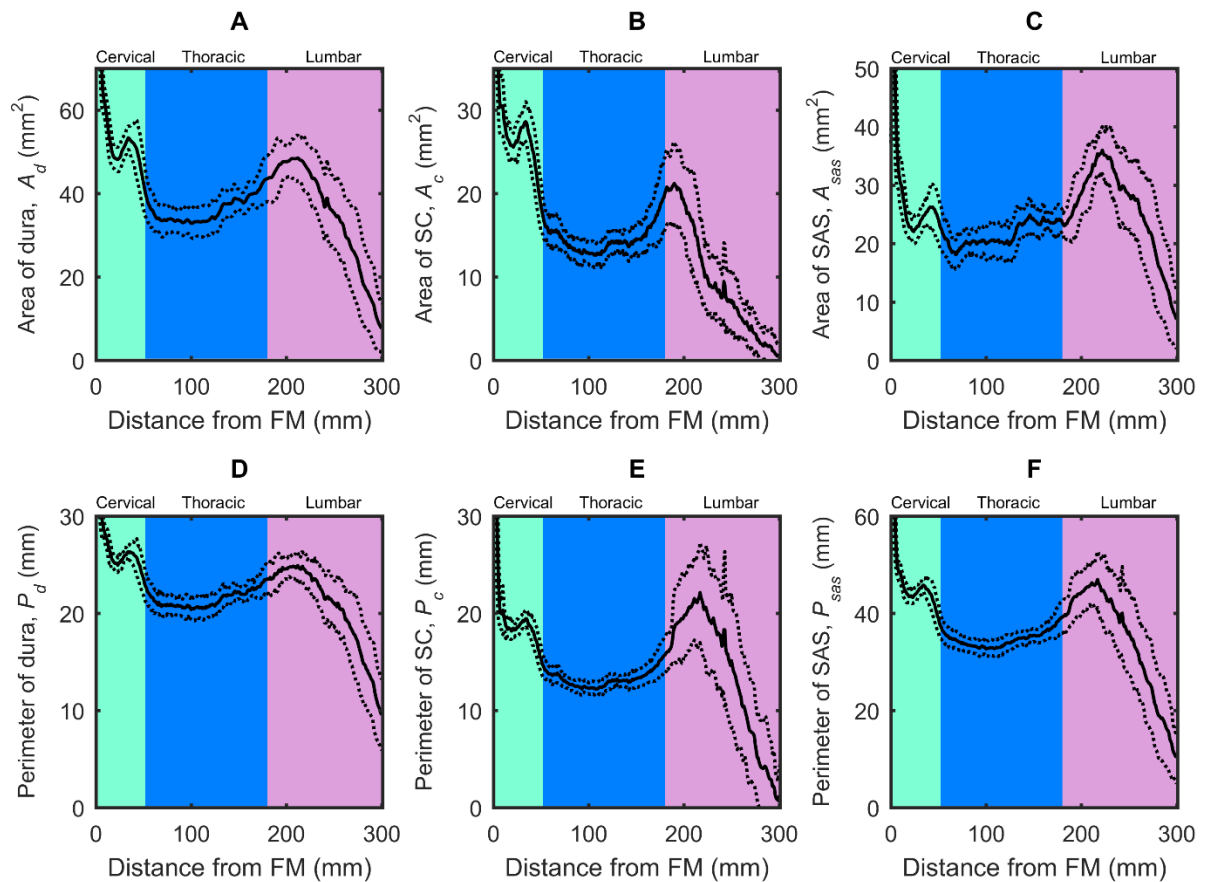


Figure 4.3. Geometric parameters distribution computed along the spine for cynomolgus monkeys. (A) Area of dura, (B) Area of spinal cord, (C) Area of subarachnoid space, (D) Perimeter of dura, (E) Perimeter of spinal cord, (F) Perimeter of subarachnoid space. Mean value for all 16 NHPs corresponds to the solid line. Dotted lines correspond to ± 1 standard deviation for all 16 NHPs analyzed.

CSF Flow Waveforms

$Q(t)$ of each NHP quantified along the spine had a similar waveform shape, magnitude and axial distribution (**Fig 4**). $Q(t)$ shape showed a well-defined systolic peak at 100 to 300 ms (negative flow) followed by a diastolic peak that varied based on the heart rate (similar to cardiac blood flow). Q_{sys} ranged from 0.35 - 0.87 (ml/s) at the C3-C4 level for all NHPs. $Q(t)$ at the FM was markedly smaller than at C3-C4. Caudal to C3-C4, $Q(t)$ had a decreasing trend in magnitude moving down the spine. The CSF flow was found to be nearly zero in all PC-MRI scans before eddy current offset correction. Maximum average CSF flow offset was 13% relative to the arithmetic mean of the absolute CSF flow.

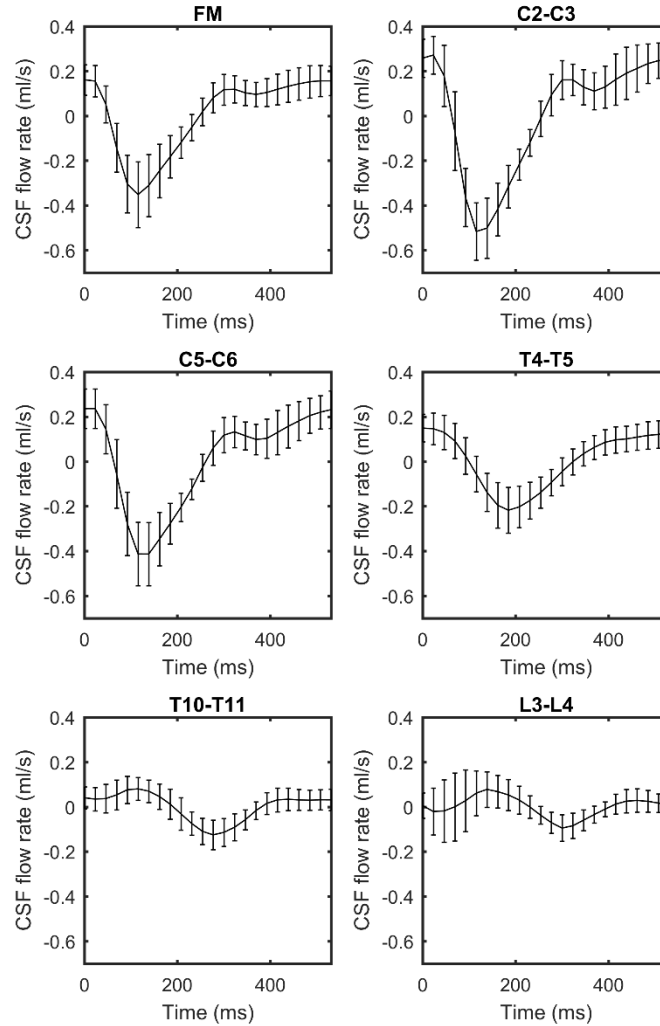


Figure 4.4. CSF flow waveforms for all 16 cases measured by PC-MRI at six axial locations along the spine. Error bars correspond to ± 1 standard deviation of flow rates obtained for all 16 NHPs. Note: negative, or peak systolic, CSF flow is in the caudal direction.

Average spatial-temporal $Q(t)$ distribution across all NHPs showed a relatively smooth decrease in amplitude along the spine and had relatively small, if any, wave reflections from the SAS termination (**Fig 5B**). Spatial temporal $Q(t)$ distribution showed that maximum CSF flow rate occurred ~ 25 mm caudal to the FM (**Fig 5B**). $Q(t)$ shape and magnitude were similar from ~ 125 mm to the SAS termination.

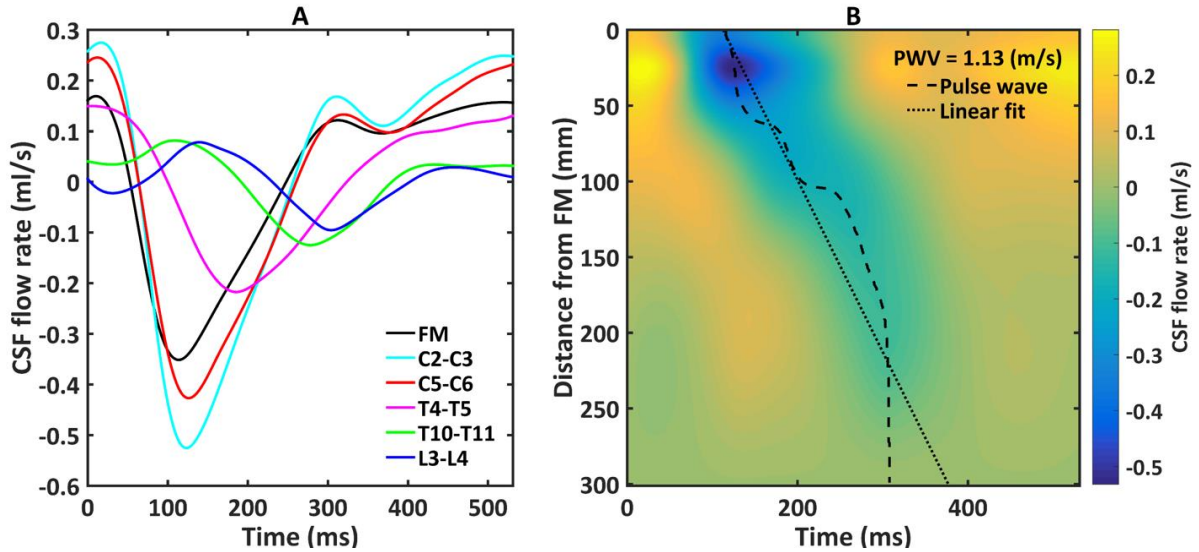


Figure 4.5. Mean CSF flow waveforms and Spatial-temporal distribution of CSF flow rate (A) Mean CSF flow waveforms for all 16 cases measured by PC-MRI at six axial locations along the spine. Note: negative, or peak systolic, CSF flow is in the caudal direction. (B) Spatial-temporal distribution of the interpolated CSF flow rate along the spine. Dotted line indicates peak CSF flow rate at each axial level used to compute CSF pulse wave velocity (PWV).

Hydrodynamic Parameters

SV ranged from ~ 0 to 0.14 ml along the spine and had the greatest value at the axial location corresponding to C3-C4 (**Fig 6**). Difference in SV between NHPs was a maximum of ~ 0.1 ml at the upper cervical spine (C3-C4).

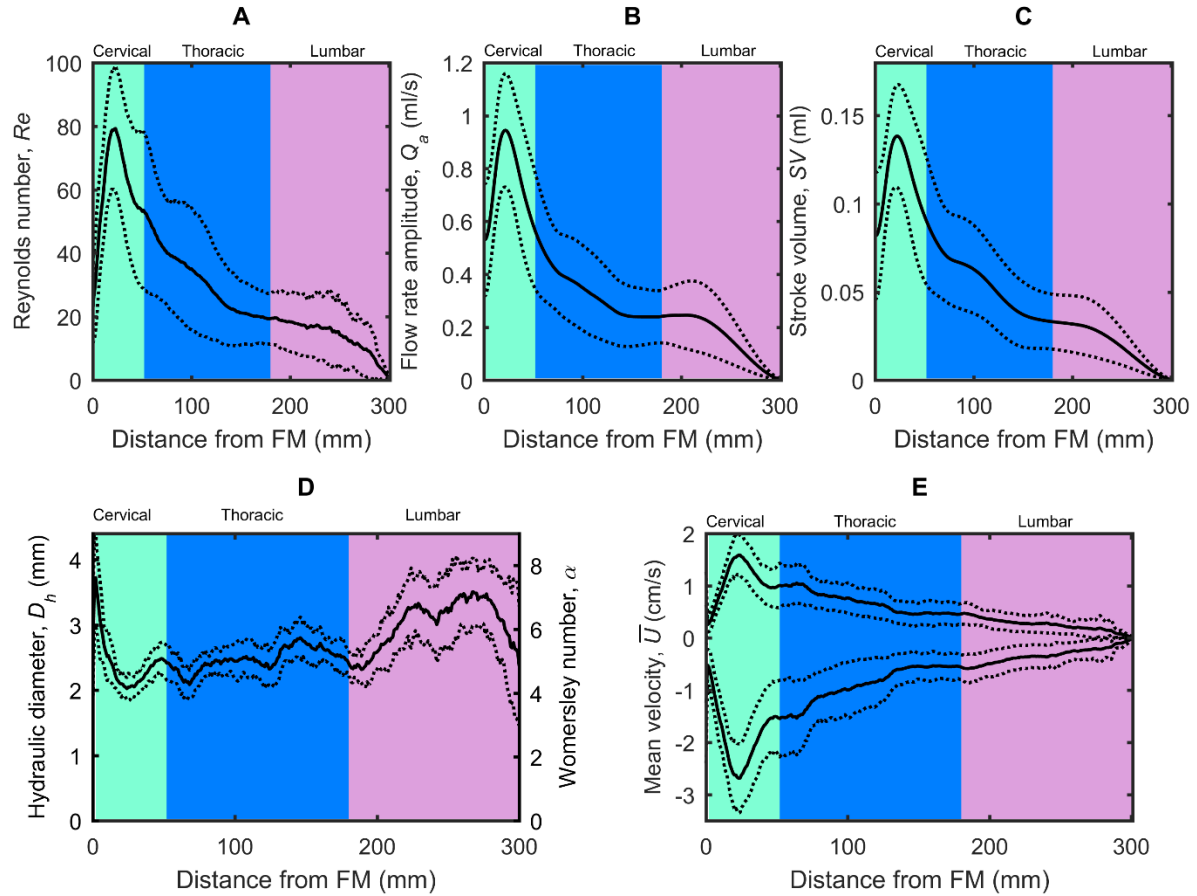


Figure 4.6. Hydrodynamic parameter distribution computed along the spine for cynomolgus monkeys. (A) Reynolds number, Re , (B) Flow rate amplitude, Q_a , (C) Stroke Volume, SV , (D) left axis, Hydraulic diameter, D_h , right axis, Womersley number, α , (E) mean peak systolic, \bar{U}_{sys} , and diastolic, \bar{U}_{dia} , CSF velocity. Mean value for all 16 NHPs corresponds to the solid line. Dotted lines correspond to ± 1 standard deviation for all 16 NHPs analyzed.

A noticeable phase shift was observed in the $Q(t)$ along the spine (**Fig 4**). This phase shift is thought to be representative of intrathecal space stiffness or compliance and can be quantified in terms of PWV . Based on the time of Q_{sys} at the FM versus the lumbar spine, PWV was estimated to be vary from 0.73 to 3.45 m/s among NHPs with an average value of 1.13 m/s (**Table 3**).

Re had a decreasing trend moving caudally along the spine (**Fig 6A**). Re varied from 80 in the cervical spine to 0 at the most caudal region, with the maximum value located at C3-C4 level. Local

difference in Re among the NHPs was a maximum of ~ 75 and located within the cervical spine. α ranged from 4 to 7.7, with a maximum value located near the FM (**Fig 6D**, right axis).

The peak value of the \bar{U}_{dia} and \bar{U}_{sys} ranged from +1.6 to -2.7 cm/s and occurred at the C3-C4 level (**Fig 6E**). \bar{U} was smaller at the FM compared to C3-C4 for all NHPs. As expected, these alterations in \bar{U} were inversely related to A_{sas} ; axial locations with largest A_{sas} (FM, see **Table 3** and **Fig 3**) demonstrated reduced velocities compared to areas with smaller A_{sas} and their respective increased velocities.

Parameter Reliability

There was relatively good agreement between the baseline and follow-up MRI scans across all parameters confirming the reproducibility of the method. Differences between geometrics and hydrodynamic parameters obtained from the baseline to the follow-up MRI scan were quantified using regression analysis as shown in **Figs 7** and **8**. The results correspond to all eight NHPs and are plotted for the entire spine model between baseline and follow-up (from FM to the SAS termination).

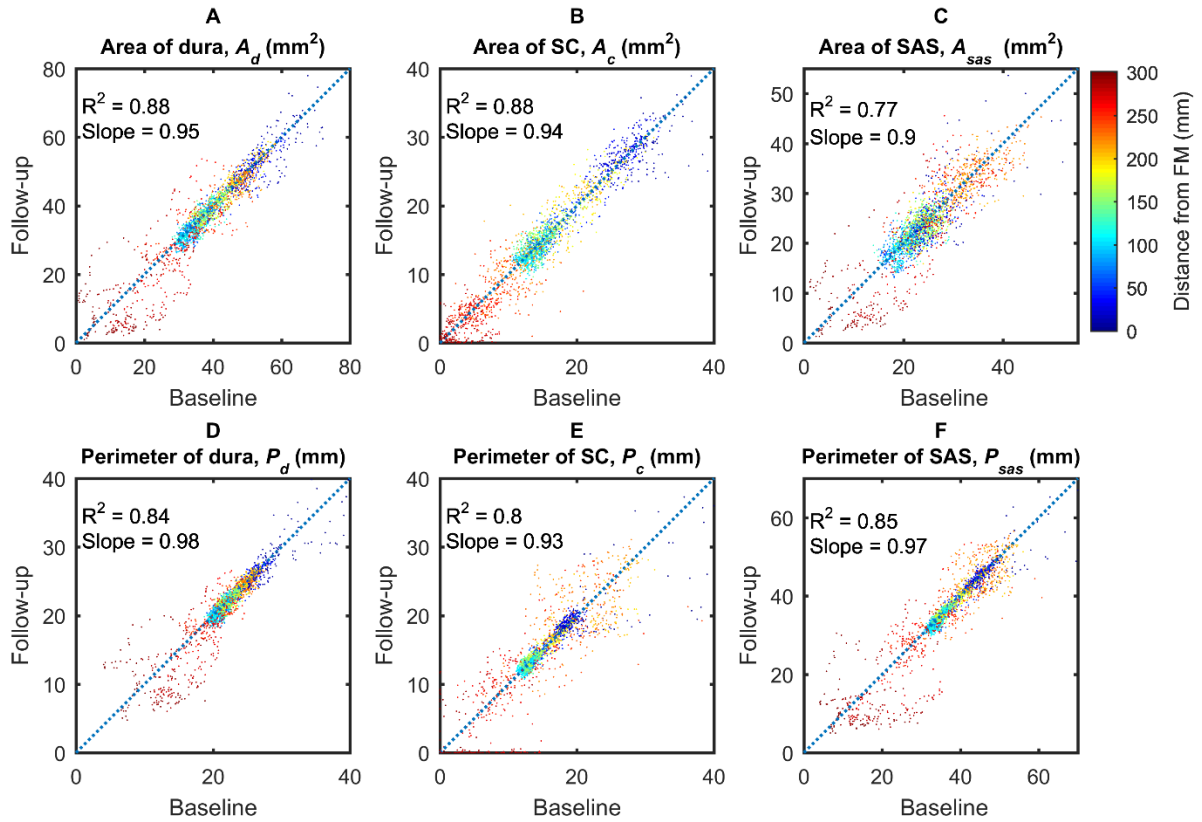


Figure 4.7. Scatter plots of geometric parameters. (A) Area of dura, (B) Area of spinal cord, (C) Area of subarachnoid space, (D) Perimeter of dura, (E) Perimeter of spinal cord, (F) Perimeter of subarachnoid space. Dot color represents distance from the FM (blue is near the FM and red is near the SAS termination).

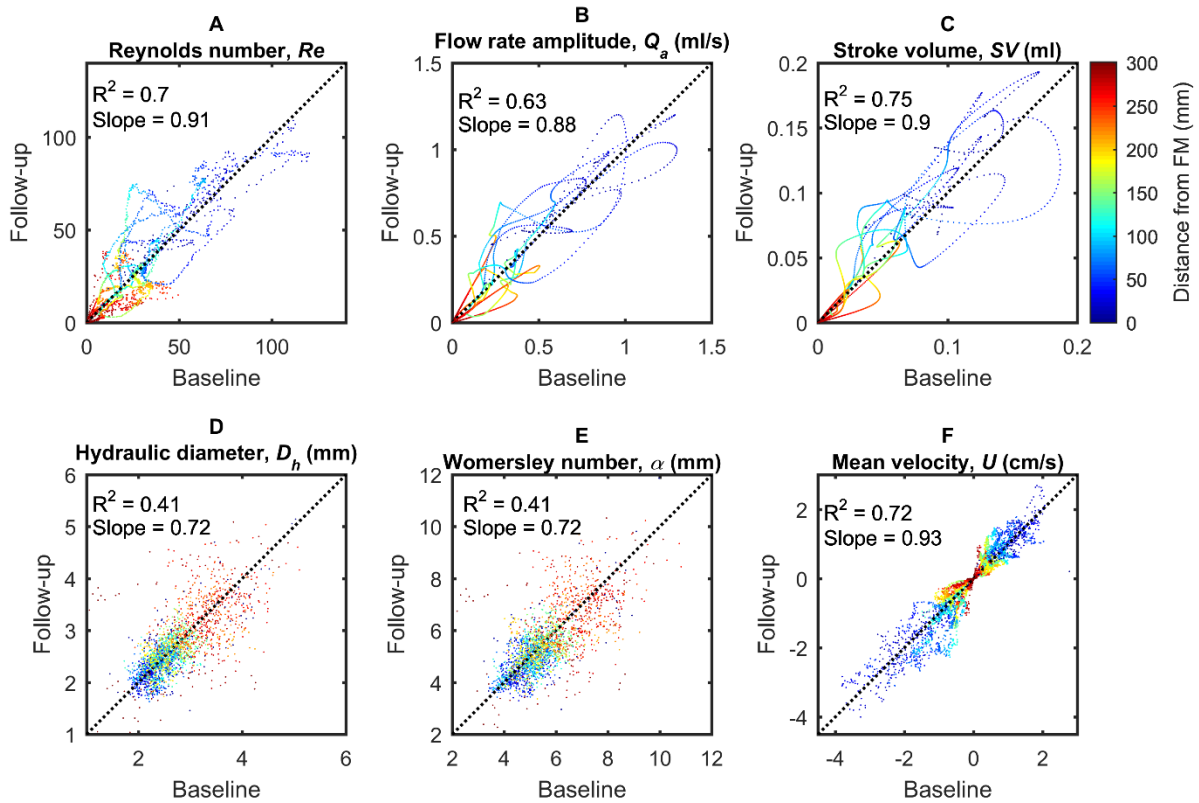


Figure 4.8. Scatter plots of hydrodynamic parameter distribution computed along the spine. (A) Reynolds number, Re , (B) flow rate amplitude, Q_a , (C) stroke volume, SV , (D) hydraulic diameter, D_h , (E) Womersley number, α , and, (F) mean peak systolic, \bar{U}_{sys} , and diastolic, \bar{U}_{dia} , CSF velocity. Dot color represents distance from the FM (blue is near the FM and red is near the SAS termination).

Strong correlation was observed from the linear regression analysis for P_d ($R^2 = 0.84$, $slope = 0.98$), P_c ($R^2 = 0.80$, $slope = 0.93$), and P_{sas} ($R^2 = 0.85$, $slope = 0.97$). Correlation was stronger for the A_d ($R^2 = 0.88$, $slope = 0.95$) and A_c ($R^2 = 0.88$, $slope = 0.94$), but was slightly weaker in A_{sas} ($R^2 = 0.77$, $slope = 0.90$).

The second set of regression plots (**Fig 8**) showed that the value of discrepancy between baseline and follow-up results could be higher for hydrodynamic parameters. There was a relatively weak correlation for α and D_h ($R^2 = 0.41$, $slope = 0.72$). Relative to geometric results, there was

additional discrepancy for flow parameters related to \bar{U} ($R^2=0.72$, $slope=0.93$), Q_a ($R^2=0.63$, $slope=0.88$), and SV ($R^2=0.75$, $slope=0.90$), though not to the degree as the α and D_h .

Discussion

This study presents a method and results for detailed characterization of intrathecal CSF geometry and hydrodynamics in cynomolgus monkeys (*Macaca fascicularis*). Results show that CSF geometry and dynamics can be reliably detected using non-invasive MRI measurements and that results are consistent for cynomolgus monkeys of a similar size and age.

Nature of CSF Dynamics in Cynomolgus Monkeys

Our results show that CSF moves in a smooth oscillatory manner along the entire spinal axis of cynomolgus NHPs. Chaotic velocity or pressure fluctuations are not expected and transverse CSF velocities (non-streamwise) are likely small compared to axial velocities. CSF dynamics were found to be most active in the cervical spine near the C3-C4 vertebral level with a maximum Re of 80 (**Table 3** and **Fig 6**). Re was computed to represent the ratio of steady inertial forces to viscous forces and help indicate whether laminar flow ($Re < 2300$) was present at each phase contrast slice location (**Fig 6** and **Table 3**). A laminar CSF flow indicates that the flow is smooth with relatively little lateral mixing. This is different from a turbulent flow, where chaotic changes in pressure and velocity occur and can lead to a large increase in lateral mixing. Thus, CSF flow is expected to remain laminar throughout the CSF flow cycle as the Re remained sub-critical ($Re_{critical}=2100$) for all NHPs analyzed. However, it is possible that disease states that result in strongly elevated CSF flow velocities (jets) could result in turbulence [108].

Inertial effects are expected to dominate the SAS CSF flow field for normal physiological flow rates, frequencies and CSF fluid properties. α varied in the same fashion as D_h with a minimum and maximum value of 4.1 and 7.7 (**Table 3** and **Fig 6**). α , was computed to quantify the ratio of unsteady inertial forces to viscous forces that impact the CSF velocity profile shape [64]. For $\alpha < 1$, the CSF velocity profiles will be parabolic in shape. $\alpha > 10$ will result in relatively flat or plug-like velocity profiles [109]. This means that the CSF velocity profiles will have a plug-like shape throughout the spine. Albeit, flows in an annulus may be less inertial compared to pipe flows of the same α [64].

Our previous computational fluid dynamics NHP model indicated a relatively blunt CSF velocity profile in the cervical spine [91]. It is difficult to confirm if the *in vivo* velocity profiles measured in the current study were in fact blunt shaped (**Fig 2C**) as the MRI resolution was not fine enough to accurately capture the relatively thin boundary layer expected in a blunt flow profile.

CSF Pulse Wave Velocity along the Spine (PWV)

With each heartbeat, a cardiac-induced CSF pulse wave was found to travel in the cranial-caudal direction (downwards) at a rate of $PWV \sim 1.13$ m/s (**Fig 5B**). This wave appeared to be damped along the spinal axis and had relatively little reflection due to the SAS termination. This PWV is similar to the study previously reported by our group [91] for one cynomolgus monkey. CSF PWV studies have been conducted for humans. Williams obtained simultaneous invasive recordings of ventricular and lumbar CSF pressure in humans during various maneuvers such as coughing and valsalva [39]. From these recordings, a CSF PWV can be estimated to range from 8-4 m/s, after coughing. Kalata et al. used high-speed PC-MRI to quantify the CSF velocity wave speed in a small portion of the cervical spine (~20 cm) and found it to be 4.6 ± 1.7 m/s [66]. Another study by Sweetman et al. predicted spinal CSF PWV to be ~3 m/s [79]. Martin et al. used a numerical 1-D tube model of the spinal SAS to analyze the effect of dura mechanical properties on spinal CSF flow and pressures and they found CSF PWV varied from 2.5 to 13.5 m/s depending on dura elasticity [80]. They also investigated spinal CSF wave phenomena using *in vitro* models and found CSF wave reflections to be present [3]. Similar conclusions have been reported by other groups with different approaches and numerical simulations [69, 71, 81, 110]. Results in this study did not show a large degree of CSF wave reflection within the spine (**Fig 5B**).

Arterial PWV has been found to have important implications in several vascular diseases [111, 112]. Spinal CSF PWV could also have implications on perivascular transport in context of syringomyelia [113-115]. Further study is necessary to understand CSF PWV in the spine and its relevance CNS physiology in health and disease.

Geometric and Hydrodynamic Characterization

To the best of our knowledge, axial variation in spinal SAS geometry in terms of A_c , P_c , and D_h in a cynomolgus monkey has not been reported in the literature. This may be due, in part, to the relatively long time period (55 minutes total) required to obtain the high-resolution MRI images (375 μm isotopic) used to segment the CSF space in this study. Geometric parameters such as A_d , A_c , A_{sas} , P_d , P_c , and P_{sas} were shown to vary significantly along the spine. Hydrodynamic parameters such as D_h , Re , α , \bar{U} , Q_a and SV also varied significantly along the spinal canal due to the changes in geometry. CSF flow measurements in the cervical spine by MRI were used to estimate flow values of hydrodynamic parameters. The variation in A_{sas} is significant ~ 7 to 75 mm^2 (see **Fig 3B**), which indicates fluid acceleration may be significant in the spinal cavity near the skull and base of the spine. D_h ranged from ~ 1.5 - 4.5 mm in all NHPs analyzed. The axial distribution of SAS geometry in the cynomolgus monkey had a similar trend as that quantified in humans for A_c , P_c , and D_h [59], albeit approximately ~ 7.4 , 2.3 , and 2.4 times smaller, respectively, in magnitude compared to a human [64].

Average V_{sas} for all NHPs in this study was $\sim 7.41 \text{ ml}$. To our knowledge, V_{sas} has not been measured in NHPs. However, total NHP CSF volume is typically considered to range from 12 - 15 mL in CSF dosing studies [116]. Our results indicate that the total NHP CSF volume in these studies is likely to be underestimated by approximately a factor of 2. Similarly, recent studies in humans show that total CSF volume is not 150 mL as reported in the traditional literature [117]. Recent researchers using high-resolution non-invasive MRI-based methods have reported the total CSF volume to be approximately two times larger, ranging from 250 - 400 mL [118, 119]. Geometric differences across people will impact results and there may be greater differences in geometry across people than in monkeys. Detailed MRI investigation of the complete CSF space in terms of its geometry is lacking in the literature.

Measurement Reliability

To help understand parameter reliability, we collected MRI images for 8 NHPs at two time points separated by a two-week time interval. Results showed a relatively strong degree of parameter reliability for all geometric-based parameters (A_d , A_c , A_{sas} , P_d , P_c , and P_{sas} in **Fig 7**) and to a lesser

degree for hydrodynamics based parameters (D_h , Re , α , \bar{U} , Q_a and SV in **Fig 8**). The reason for lower degree of reliability for hydrodynamic parameters is likely because these parameters incorporate input from both flow and geometry, both of which will have associated error and/or natural physiologic variation in NHPs. It should also be noted that we do not expect all parameters to remain identical at the 2-week follow-up time point as CSF flow can be altered due to posture, sedation, and other factors that were not specifically controlled to be identical across MRI scans in the present study. Nevertheless, the degree of reliability is presented to give a benchmark for how much these parameters can change under normal conditions. A previous study by Martin et al. showed a high degree of inter- and intra-operator reliability for MR-based geometric and hydrodynamic parameters derived from the SAS for a single patient with Chiari malformation and a healthy control subject [60]. 2-week follow-up reliability of these parameters was not considered in that study.

Limitations and Future Directions

This study provides quantitative measures and reliability assessment for intrathecal CSF dynamics and geometry in eight NHPs. Further studies should quantify potential variance of these parameters in a larger study size across NHP species, age, sex, weight, and in disease states. Geometric characterization did not take into account spinal cord nerve root surface area or volume, which may account for $\sim 231 \text{ cm}^2$ and $\sim 6 \text{ ml}$, respectively within the SAS in humans [118]. It is expected that these structures will alter the SAS surface area results presented in the current study to a large degree. Albeit, the surface area in contact with the spinal cord and dura is likely similar since the junction of spinal cord nerve roots with these structures is relatively small. Also, we do not expect these structures to alter spinal cord and dura surface area to a great degree or total SAS volume.

There are also a few unknowns in relation CSF flow dynamics. First, CSF flow coupling with the cardiovascular cycle is accounted for in the present study. However, CSF flow is also affected by respiration [120], which was not considered in this study using cardiac-gated PC-MRI measurements. Future studies could investigate the relatively contribution of respiration and cardiovascular pulsations to CSF flow dynamics along the spinal axis. Finally, CSF flow was measured at six axial locations and interpolated to generate a smooth distribution along the spine. The ideal study would minimize or eliminate interpolation as much as possible by adding more axial slice locations. Also, CSF dynamics should be quantified within the intracranial space. However, in the present study, MRI time limitation for each NHP did not allow additional slice measurement locations. The focus of the present study was on the intrathecal space, as this region is most nearby intrathecal therapeutic injection location that can be accessed by lumbar puncture or other relatively minimally invasive procedures. Injection of

medications within the ventricular space of the brain or cortical subarachnoid space would also be impacted by nearby CSF dynamics within the ventricles and cisterns of the brain.

Conclusion

This study presents a detailed geometric and hydrodynamic characterization of intrathecal CSF for eight cynomolgus monkey (*Macaca fascicularis*) with reliability assessed between baseline and a two-week follow-up time point. Results showed laminar CSF flow along the entire spine with maximum CSF flow rate at the C3-C4 vertebral level and peak systolic CSF flow rate and stroke volume at C3-C4. The methods presented demonstrate a reliable method for CSF quantification in NHPs, which may extend in future studies to *Homo sapiens*.

Chapter 5: Anthropomorphic Model of Intrathecal Cerebrospinal Fluid Dynamics within the Spinal Subarachnoid Space: Spinal Cord Nerve Roots Increase Steady-Streaming

Abstract

Cerebrospinal fluid (CSF) dynamics are thought to play a vital role in central nervous system (CNS) physiology. The objective of the present study was to investigate the impact of spinal cord nerve roots (NR) on CSF dynamics. A subject-specific computational fluid dynamics (CFD) model of the complete spinal subarachnoid space (SSS) with and without anatomically realistic NR and non-uniform moving dura wall deformation was constructed. This CFD model allowed detailed investigation of the impact of NR on CSF velocities that is not possible in vivo using MRI or other non-invasive imaging methods. Results showed that NR altered CSF dynamics in terms of velocity field, steady-streaming and vortical structures. Vortices occurred in the cervical spine around NR during CSF flow reversal. The magnitude of steady-streaming CSF flow increased with NR, in particular within the cervical spine. This increase was located axially upstream and downstream of NR due to the interface of adjacent vortices that formed around NR.

Introduction

Cerebrospinal Fluid Importance and Therapeutic Applications

Dynamic motion of cerebrospinal fluid (CSF) plays an important role in central nervous system (CNS) physiology. CSF is a water-like fluid that surrounds the brain and spinal cord (SC) and pulsates in an oscillatory manner with each cardiac and respiratory cycle [120-122]. A detailed understanding of CSF dynamics could improve treatment of CSF-related CNS diseases and lead to novel CSF-based therapeutics. The importance of CSF dynamics has been investigated in several CNS diseases that include Alzheimer's disease[123, 124], syringomyelia[47, 125], Chiari malformation[5, 6], astronaut vision impairment due to space flight[126] and hydrocephalus[8]. CSF can also serve as a conduit for drug delivery to the brain, as solutes delivered to the CSF bypass the blood brain barrier thereby providing relatively direct access to neuronal and glial cells[40, 55]. CSF-based therapeutics are presently under development for brain hypothermia[9], CSF filtration[10-13] and control of intracranial CSF pressure oscillations[14].

The efficacy of many of these treatments depends, in part, on transport within the spinal subarachnoid space (SSS). Among the least studied factors is the effect of structures within the SSS on flow and transport, yet the structures appear to strongly affect transport. For example, Stockman found that simplified nerve roots (NR) increased longitudinal transport by five to ten times compared the same channel without NR [15, 16]. Tangen et al. found that simplified microstructures increased vorticity and rostral transport of intrathecal drugs[67] and Tangen et al. noted mixing of subarachnoid hemorrhage around NR[19, 127]. Accordingly, this study focuses on the effects of more highly-resolved NR.

Previous Numerical Models of SSS CSF Dynamics

CFD has an advantage in that it is capable of achieving CSF pressure and flow field resolution that may be difficult in vivo with magnetic resonance imaging (MRI) or other invasive techniques. In addition, parameters can be varied that may not be possible to vary in vivo. One challenge has been accurately representing the complex CSF space geometry that includes feature sizes that range over five orders of magnitude from microns to tens of centimeters. In addition, these features are attached to deforming dural and pial boundaries. Numerical studies of CSF dynamics in the spine (**Table 1**) can be roughly stratified in terms of:

Table 5.1. Summary of previous spinal CSF dynamics numerical studies with key information on the numerical method, anatomic / physiologic feature investigated and the feature impact on CSF dynamics.

Study	Numerical method	3D	subject-specific	Full spine	TM	NR	AT	Anatomic / physiologic feature investigated	Feature Impact on CSF dynamics
Khani et al. (present study)	Finite volume	x	x	x	x	x		NR and non-uniform CSF flow	Steady-streaming flow and CSF vortices created during flow reversal
Tangen et al.[67]	Finite volume	x	x	x	x	x	x	Impact of AT on CSF pressure and solute spread	AT increase pressure drop but have little impact on drug spread to cervical spine
Khani et al.[128]	Finite volume	x	x	x	x			Non-uniform CSF flow in a nonhuman primate	Laminar, inertial dominated CSF flow found throughout nonhuman primate spine
Hsu et al.[129, 130]	Finite volume	x	x	x	x			Impact of CSF pulse freq. and mag. on drug spread	Increased CSF pulse frequency and magnitude increase drug spread
Cheng et al.[131]	Finite volume	x	x	x	x			FSI between CSF and spinal cord	Caused up to 2 mm of spinal cord displacement
Tangen et al.[132]	Finite volume	x		x	x	x		Infusion settings, drug chemistry and anatomy	Drug dispersion is impacted by infusion, chemistry and anatomy
Tangen et al.[127]	Finite volume	x		x	x	x		Lumbar CSF drainage after subarachnoid hemorrhage	Body position and CSF drainage rate impact blood removal from CSF
Kuttler et al.[133]	Finite volume	x		x	x			Impact of slow or fast bolus dose	Pulsation and breathing dominated long-term bolus spread (not bolus speed)
Pizzichelli et al.[134]	Finite element	x	x				x	Catheter position & angle and tissue permeability	Injection perpendicular to cord increased penetration to the cord tissue
Haga et al. [135]	Finite element	x	x				x	Catheter position, angle and injection flow rates	Catheter position, angle and injection flow rates impact solute distribution
Pahlavian et al. [43, 74]	Finite volume	x	x				x	Comparison of in vivo & in vitro MRI with CFD results	In vitro MRI compared well with CFD results, in vivo compared poorly with CFD
Pahlavian et al. [76]	Finite volume	x	x				x	Presence of NR and DL	Increased peak CSF velocities, mixing and bi-directional flow
Stockman [15]	Lattice Boltzmann	x					x	NR, DL and AT	Increased non-streamwise components of CSF velocity
Pahlavian et al. [6]	Finite volume	x	x		x			Pulsatile motion of cerebellar tonsils	Increased peak CSF velocities, mixing and bi-directional flow
Bertram et al.[136]	Finite element			x	x			Spinal cord and dura compliance	Pressure wave propagation impacted by the elastic properties of tissue
Bertram et al.[137]	Finite element			x	x			Spinal cord tethering due to arachnoiditis	Increased tensile radial stress and decreased pressure in the spinal cord material
Elliott[138]	Finite difference			x	x			Posttraumatic syringomyelia	Stress induced by syrinx fluid sloshing diminishes as syrinx expands
Elliott[70]	Analytic			x	x			Syrinx filling due to CSF wave mechanics	Syrinx filling impacted by CSF flow obstruction and tissue properties
Jain et al.[139]	Lattice Boltzmann	x	x					Highly resolved direct numerical simulation	Onset of transitional CSF flow in Chiari patients
Cheng et al. [140]	Finite volume	x	x					Arachnoiditis permeability	Increased bi-directional flow, peak CSF pressure timing shifted
Rutkowska[141]	Finite volume	x	x					Presence of tonsillar herniation	Increased peak CSF velocities, gradient and bi-directional flow
Yiallourou et al.[73]	Finite volume	x	x					Presence of tonsillar herniation	Increased peak systolic CSF velocities, flow jets near foramen magnum
Clarke et al.[142]	Finite volume	x	x					Presence of tonsillar herniation	Increased magnitude of peak pressure
Shaffer et al.[143]	Finite volume	x	x					Tonsillar descent	Increased longitudinal impedance to CSF flow and correlated with tonsillar descent
Martin et al.[59]	Finite volume	x	x					Tonsillar descent	Increased peak CSF velocities, pressure gradient and longitudinal impedance
Roldan et al.[144]	Boundary element	x	x					Tonsillar descent	Increased peak CSF velocities near the CVJ and peak pressure gradient along SSS
Linge et al.[145]	Finite volume	x						Tonsillar descent & surgery impact	Increase peak CSF velocities, velocity heterogeneity and CSF pressure gradient
Linge et al.[146]	Finite volume	x						Presence of tonsillar herniation	Increased peak CSF velocities and pressure gradient near the tonsils
Linge et al.[147]	Finite volume	x						Increase in cardiac rate	Increased pressure gradient, increased magnitude of bi-directional flow
Bilston et al.[148]	Finite volume							Decreased arachnoiditis permeability	Increased pressure gradient along the SSS
Loth et al. [64]	Finite volume		x	x				Cross sectional geometry and spinal cord motion	Pressure gradient waveform dependent on CSF flow waveform and cross-sectional area

Key: 3D - model constructed in three dimensions, TM - tissue motion included in model, AT - arachnoid trabeculae included in model, NR - nerve roots included in model.

- a) *Numerical method applied*: finite volume, finite element, finite difference, analytic and lattice Boltzmann methods.
- b) *Anatomic domain and physiological accuracy*: partial/entire SSS length, simplified 2D/3D, subject-specific based on MR imaging.
- c) *Microstructure and tissue motion*: spinal cord nerve roots (NR) and/or arachnoid trabeculae (AT), prescribed boundary motion, fluid-structure interaction.
- d) *Focus of the investigations*: impact of NR and AT on CSF mixing[76], fluid structure interaction of dynamically deforming spinal cord tissue[140], intrathecal drug solute[133-135] and blood[132] transport, and anatomic alterations within disease states such as Chiari malformation and syringomyelia[59]. Several studies have included anatomically idealized NR. Only three studies included arachnoid trabeculae [15, 67, 149] (note: study by Gupta et al. focused on intracranial SAS and not included in **Table 1**).

Objectives

There is a need to understand the impact of realistic geometry on CSF flow patterns. An anatomically accurate and validated model will allow testing and optimization of CNS therapeutics that could lead to more rapid application for clinical use and reduced cost for non-human primate studies. To address these needs, the objectives of this study were to build upon the body of CSF modeling work (**Table 1**) by: 1) MRI measurements of SSS geometry and flow distribution in a patient, and 2) CFD simulation of unsteady CSF flow in a SSS model with and without anatomically realistic spinal cord NR based on the MRI measurements. We hypothesized that the presence of NR increases non-uniformity of axial flow velocities and promotes steady-streaming within the SSS.

Methods and Materials

Ethics Statement

In this study, all the MRI data collection development was approved by the local institutional review board in Amiens, France and satisfied all local and international regulations for human subject research. All data was de-identified before transferring to the University of Idaho for further analysis.

Subject Selection

A 23-year female was chosen for this study as a representative healthy subject to define the CSF space geometry and flow for the numerical model. The subject did not have any history of spinal deformity or CSF-related disorders.

MRI CSF Flow Measurement and Quantification

A General Electric 3T scanner was used to obtain all MRI measurements (Signa HDxt, software 15.0_M4_0910.a, Boston MA, USA) using our previously published methodology[128]. CSF flow rate was measured at three vertebral levels, C2-C3, C7-T1 and T10-T11 (**Figure 1a and b**), using phase-contrast MRI with retrospective electrocardiogram gating with 32 cardiac phases [59]. Each slice had a thickness of 5.0 mm and an in-plane resolution of 0.54 x 0.54 mm. The slice orientation was approximately perpendicular to the spine and placed vertically by intersection with a vertebral disk (**Figure 1a**). CSF flow waveforms were interpolated between the measurement locations to obtain a smooth distribution of CSF flow rate along the entire spine[128]. Zero flow was assumed at the spine termination. Flow at the foramen magnum was assumed to have identical shape as C2-C3 but with 40% reduction in amplitude based on our previous publications with quantification of axial distribution of CSF flow in humans[73, 74] and nonhuman primates[128].

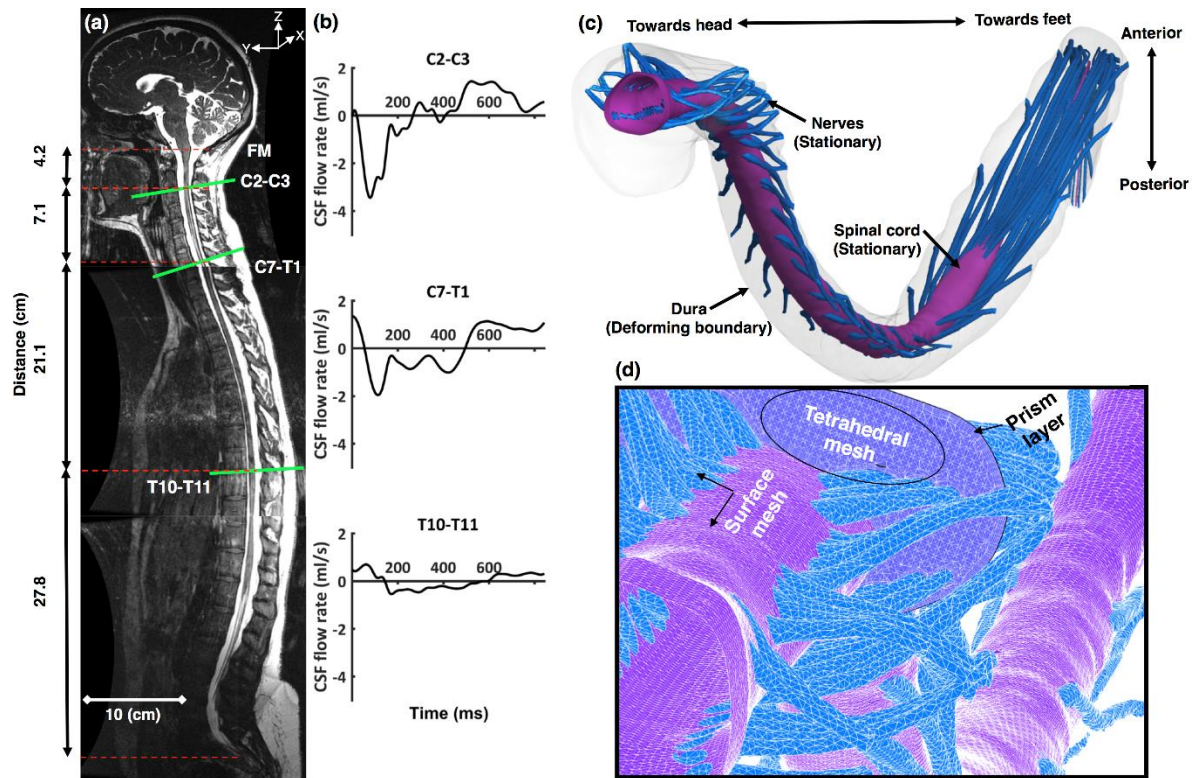


Figure 5.1. Summary of numerical modeling approach based on subject specific MRI measurements. (a) T2-weighted MR image of the entire spine for the human analyzed (open-source 3D geometry from Sass et al.[150]). Axial location and slice orientation (lines) of the phase-contrast MRI scans obtained in the study. Slice axial distance indicated by dotted lines (b) The CSF flow rate based on in vivo PCMRI measurement at C2-C3, C7-T1, T10-T11. (c) Three-dimensional CFD model of the SSS. (d) Volumetric and surface mesh visualization with zoom of the upper cervical spine (top).

MRI CSF Space Geometry Protocol and Segmentation

The freely downloadable open-source 3D spine geometry with spinal cord NR given previously by Sass et al. was used for this study[150]. In brief, high-resolution MR images were collected within three regions to define the complete intrathecal CSF space geometry (**Figure 1a**). 3D fast imaging employing steady state acquisition (3D FIESTA) was used to collect geometric measurements with improved CSF signal. In-plane voxel spacing was 0.547 x 0.547 mm and slice thickness was 1 mm with slice spacing set at 0.499 mm. Echo times (TE) were 1.944, 2.112, 2.100 and repetition times (TR) were 5.348, 5.762, 5.708 for the craniocervical, thoracic, and lumbosacral volumes, respectively. Total imaging time for the three levels was ~45 minutes.

The open-source program, ITK-SNAP (Version 3.4.0, University of Pennsylvania, U.S.A.) [106], was used to segment the MRI data. A single operator segmented the complete spine. The final model includes the 31 pairs of dorsal and ventral NRs, the spinal cord and dural wall (**Figure 1c**). Axial position of NR was placed based on the MR imaging. However, the structure and orientation of each NR was idealized based on cadaveric measurements as described by Sass et al. 2017[150].

Computational Model

The computational domain with non-uniform unstructured grid was generated within ANSYS ICEM CFD software (ANSYS® Academic Research, Release 17.2, University of Idaho, Moscow ID, USA) and consisted of approximately 13.7 million tetrahedral elements (**Figure 1d**). The commercial finite volume CFD solver ANSYS FLUENT (ANSYS® Academic Research, Release 17.2, University of Idaho, Moscow ID, USA) was used to solve the continuity (Equation 8) and Navier-Stokes (Equation 9) equations

$$\nabla \cdot (\rho U) = 0 \quad (8)$$

$$\rho \left(\frac{\partial U}{\partial t} + U \cdot \nabla U \right) = -\nabla P + \mu \nabla^2 U \quad (9)$$

where ρ is the density, μ is the dynamic viscosity, and U and P describe the velocity and pressure fields, respectively. CSF was considered to be an incompressible Newtonian fluid with viscosity and density equivalent to water at body temperature[62, 149] ($\rho=993.3 \text{ kg/m}^3$ and $\mu=0.6913 \text{ mPa}\cdot\text{s}$). The laminar viscous model was used.

A zero pressure-outlet boundary condition was defined at the foramen magnum. No-slip boundary conditions were imposed at the dural and pial walls. The pial boundary was stationary. Dural boundary motion was modeled based on the in vivo MRI flow measurements. The non-uniform deformation of the computational mesh was implemented at each time step, as described by Khani et al. 2017, by a User Defined Function[128]. In summary, this method split the dura into 1 mm segments (606 Segments total) and dural spatial-temporal displacement was modeled to reproduce the interpolated CSF flow rates at each axial level. This resulted in a non-uniform circumferential displacement in the radial direction. In brief, the method involved 1) interpolation of MRI CSF flow measurements onto 1 mm slice intervals of size, Δh , along the spine 2) determination of the centroid of each slice, 3) dividing the slice into N pie-shaped radial sections depending on the number of nodes

present at the dura wall, 4) movement of each node on the dura surface by a value, Δr , for each radial

section based on its radial distance, r_{node} , from the centroid of the slice:

$$\Delta r = \sqrt{r_{node}^2 - \frac{\Delta Q \cdot \Delta t}{\pi \cdot \Delta h}} - r_{node}$$

where ΔQ is the difference in CSF flow rate across each slice section and Δt is the time-step (see Khani et al. 2017[128]).

Second-order momentum and pressure gradient solvers were used with default values for under relaxation factors. The convergence criteria for velocity, continuity and momentum were set to 1E-06. Total simulation time was 30 hours for two cycles (results are presented for the 2nd cycle only) in parallel mode with 141 GB RAM and 30 processors at a clock speed of 2.3 GHz.

Numerical Sensitivity Studies

CFD results were verified by numerical sensitivity studies for time-step size, cycle and mesh resolution (**Table 2**) with respect to velocity and cyclic mean velocity (**Figure 2**) using an improved methodology from that of Khani et al.[128]. For these studies, we quantified sensitivity of z-velocity and cyclic mean z-velocity (steady-streaming) at three locations within the model for a “coarse”, “medium”, “fine” and “X-fine” mesh with wall prism layers (**Figure 2a and b**). Based on these results, a single “fine” mesh was carried forward for completion of subsequent cycle and time-step sensitivity studies. Time-step sensitivity was then checked with time-step resolution given by fractions of the cardiac cycle, $T = 0.84$ s, for $T/168$, $T/84$, $T/42$. Cycle sensitivity was checked over three complete cardiac cycles.

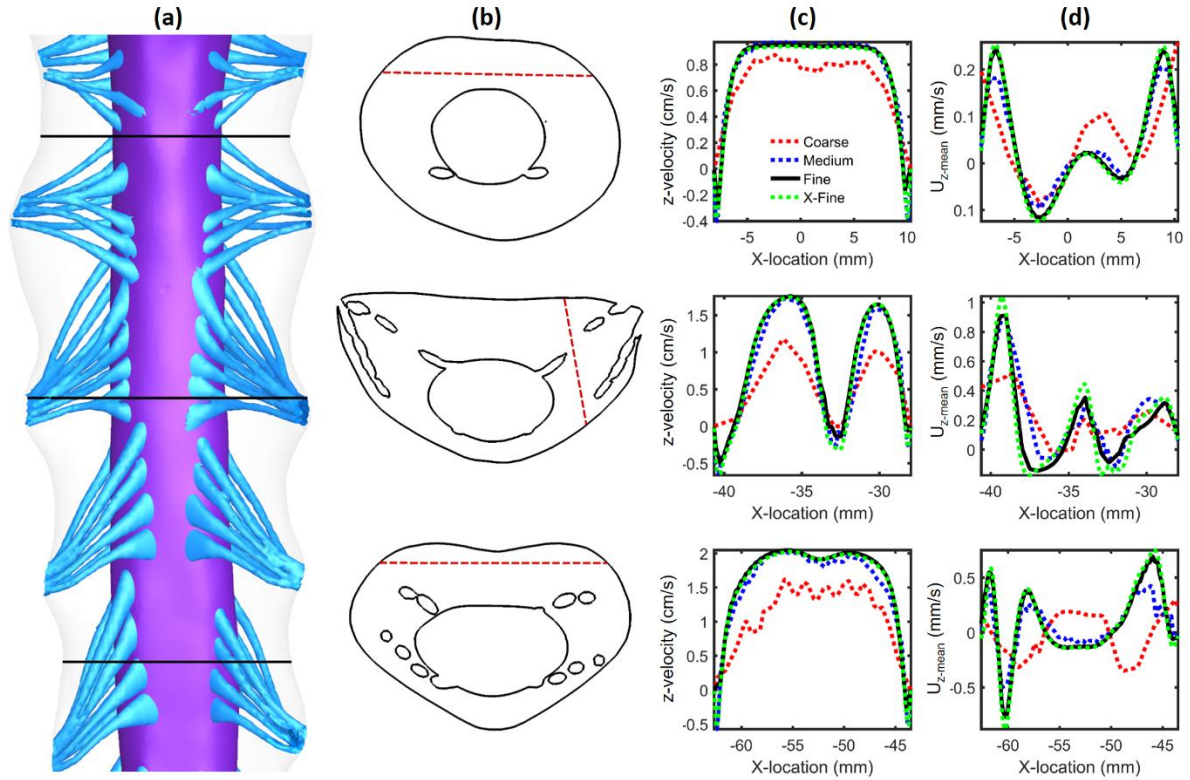


Figure 5.2. Numerical sensitivity study for velocity and cyclic mean velocity results. (a) 3D geometry of the sensitivity study and axial plane positions, (b) line location along each plane, (c) simulated peak systolic z-velocity component along each line for the four grids (coarse, medium, fine and X-fine), and (d) simulated cross-sectional mean velocity, U_{z-mean} , along each line for the four grids.

CFD Model Comparison with In Vivo MRI CSF Flow Measurements

Dural wall motion was set to reproduce the local CSF flow rate waveform measured by MRI along the spine. The simulated flow rates were compared to the MRI flow rates at three axial locations (**Figure 1b**). Percent error was defined as the maximum difference between the unsteady flow rate produced by the CFD model, $Q_{CFD}(t)$, and the corresponding flow rate measured by MRI, $Q_{MRI}(t)$, divided by the mean of the absolute value of CSF flow rate over the cardiac cycle,

$$\%error = \left| \frac{\max(Q_{CFD}(t) - Q_{MRI}(t))}{\text{mean}|Q_{MRI}|} \right|$$

Quantitative Solution Verification Using Factor of Safety Method

To further verify the numerical results, the following factor of safety method was applied as developed by Xing and Stern [151, 152]. The accuracy of this method has been evaluated for uncertainty estimates [153]. The use of the L2 norm and factor of safety method has an advantage over methods based on local error estimates, as applied above and in a number of previous CSF simulations [6, 76, 154, 155], as the former accounts for the errors across the whole solution domain and convergence of errors on three not two grids. As such, we present the methodology to assist researchers in verification of numerical results.

Let S_1 , S_2 , S_3 represent the X-fine, fine and medium grid solutions for velocity, respectively. The relative difference between the fine grid solution and correlation value, A , is calculated as,

$$\delta_{\%} = \left| \frac{A - S_1}{A} \right| \times 100\% \quad (10)$$

The solution verification study requires the use of the following equations,

$$\varepsilon_{21} = S_2 - S_1 \quad (11)$$

$$\varepsilon_{32} = S_3 - S_2 \quad (12)$$

$$R_G = \varepsilon_{21} / \varepsilon_{32} \quad (13)$$

$$P_G = \frac{\ln(\varepsilon_{32} / \varepsilon_{21})}{\ln(r_G)} \quad (14)$$

The grid refinement ratio r_G is 2. This value was specified in ANSYS by dividing the maximum mesh size by two for each simulation (See **Table 2**, mesh size values). Evaluation of the convergence ratio R_G , order of accuracy P_G for point variables on the velocity profiles can be problematic when the solution changes ε_{21} and ε_{32} both go to zero so that their ratio is ill-defined. This was overcome by using the following Separate L2 norms of ε_{21} and ε_{32} for R_G and P_G [156], i.e.,

$$\langle R_G \rangle = \|\varepsilon_{21}\|_2 / \|\varepsilon_{32}\|_2 \quad (15)$$

$$\langle p_G \rangle = \frac{\ln(\|\mathcal{E}_{32}\|_2 / \|\mathcal{E}_{21}\|_2)}{\ln(r_G)} \quad (16)$$

Where $\langle \rangle$ is used to denote a profile-averaged quantity (with ratio of solution changes based on L2 norms) and $\|\cdot\|_2$ is used to denote the L2 norm defined below,

$$\|\mathcal{E}_{32}\|_2 = \sqrt{\sum_{i=1}^n |S_{3,i} - S_{2,i}|^2} \quad (17)$$

$$\|\mathcal{E}_{21}\|_2 = \sqrt{\sum_{i=1}^n |S_{2,i} - S_{1,i}|^2} \quad (18)$$

In Equations (17) and (18), n is the number of points on the velocity profiles, which is the same for the three meshes. Monotonic convergence is achieved when $0 < \langle R_G \rangle < 1$. The ratio of the estimated order of accuracy to the theoretical order of accuracy is defined as,

$$P = \frac{\langle p_G \rangle}{P_{th}} \quad (19)$$

where, P_{th} is the nominal order of accuracy of the numerical schemes applied, which is set to be 2.

The estimated numerical error, δ_{RE} , and grid uncertainty, U_G , are defined as,

$$\delta_{RE} = \frac{\|\mathcal{E}_{21}\|_2}{r_G^{\langle p_G \rangle} - 1} \quad (20)$$

$$U_G = \begin{cases} [1.6P + 2.45(1-P)]|\delta_{RE}| & 0 < P \leq 1 \\ [1.6P + 14.8(P-1)]|\delta_{RE}| & P > 1 \end{cases} \quad (21)$$

Using δ_{RE} , the exact solution can be estimated as $S_{exact} = S_1 - \delta_{RE}$. Grid uncertainty U_G is an estimate of an error such that the interval $\pm U_G$ contains the true value of numerical error δ_{RE} at least

95 times out of 100, i.e., at the 95% confidence level. An uncertainty interval thus indicates the range of likely magnitudes of δ_{RE} . A lower U_G value indicates a more accurate solution.

Table 5.2. Numerical sensitivity studies — values show the maximum relative error for velocity in the z-direction for the three axial planes analyzed (Figure 2).

Sensitivity study	Parameter to study	Constant parameters	Maximum error (%)
Grid size	MS= 2 mm, GS= 0.06 M PS= 0.1 mm, PN= 3	TS=CT/84	68
	MS= 1 mm, GS= 0.6 M PS= 0.1 mm PN= 3	CN=2	15.7
	MS= 0.5 mm, GS= 3.7 M PS= 0.05 mm PN= 4		4.4
	MS= 0.25 mm, GS= 29.5 M PS= 0.025 mm, PN=6		
Time Step Size	CT/42	GS=3.7 M	51
	CT/84	CN=2	18
	CT/168		2.7
	CT/336		
Cycle number	1	GS=3.7 M	16.1
	2	TS=CT/84	3.7
	3		3.06
	4		

GS = Grid Size, PS = Prism Size, PN = Prism Number, MS = Mesh Size,

CN = Cycle Number, M = Million cells, CT = Cycle Time in seconds, TS = Time Step size

Factor of Safety Method Results

The factor of safety method gives additional confidence in the velocity results (**Table 3**). For the mean velocity profiles, grid uncertainties decreased with grid refinement for all three profiles (**Figure 2c and d**), although the magnitudes for Group 1 (X-fine, fine, medium) were the same order-of-magnitude as for Group 2 (fine, medium, coarse). A similar trend was observed for z-velocity, but the difference between grid uncertainties for Groups 1 and 2 were much greater. Grid uncertainties for Group 1 were one order-of-magnitude smaller than that for Group 2, which suggests that the z-velocity is much more sensitive to grid refinement than the mean velocity profile.

Table 5.3. Verification of results by factor of safety method — values show the global error for velocity in the z-direction for the three axial planes analyzed (Figure 2).

Parameter	Study group	Grid uncertainty (%S ₁)
Mean velocity, U_{z-mean}	Group 1 (X-fine, Fine, Medium)	0.72
		1.06
		0.34
	Group 2 (Fine, Medium, Coarse)	1.09
		1.02
		0.59
Z-Velocity	Group 1 (X-fine, Fine, Medium)	1.13
		2.69
		0.728
	Group 2 (Fine, Medium, Coarse)	10.64
		36.94
		1.5

Geometric and Hydrodynamic Quantification

Based on the 3D reconstruction and meshing, the following geometric and hydrodynamic parameters were calculated along the spine at 1 mm intervals using our previously described

methods[128]. Reynolds number based on hydraulic diameter was calculated as $Re = \frac{|Q_{max}| D_H}{\nu A_{cs}}$, where

$|Q_{max}|$ is the absolute value of the peak flow rate from the flow rate waveform at each cross section,

D_H is hydraulic diameter, A_{cs} is the cross-sectional area and ν is kinematic viscosity. Reynolds

number for external flow around NR was quantified as: $Re_{NR} = \frac{U_{\infty} D_{NR}}{\nu}$ where NR cylinder diameter,

D_{NR} , was given by the axial distribution of NR diameters along the spine provided by Sass et al.

2017[150] (ranging from 0.5 to 1.5 mm) and free-stream velocity, U_{∞} , was approximated based on the maximum value of the peak CSF velocity quantified for each axial slice. Stokes-Reynolds number

(Reynolds number based on the Stokes layer thickness $\delta = \sqrt{\frac{2\nu}{\omega}}$) was calculated as $Re_{\delta} = \frac{|Q_{max}| \delta}{\nu A_{cs}}$.

To assess possibility of instabilities in an oscillatory flow around cylinders, Keulegan-Carpenter

number was computed as: $K = \frac{U_{\infty} T}{D_{NR}}$ and the value of beta is given by, $\beta = \frac{Re_{NR}}{K} = \frac{D_{NR}^2}{\nu T}$. Flow

instabilities occur for values of $K > 2$ under a given β as shown experimentally by Honji (1981)[157]

and theoretically by Hall (1984)[158]. Womersley number was quantified as $\alpha = \frac{D_H}{2} \sqrt{\omega / \nu}$ where

$\omega = 2\pi / T$ is angular velocity. The following indicators of the possible presence of turbulent flow

were quantified, 1) Maximum Reynolds number $Re > 2300$ at each location along the spine, and 2)

Stokes-Reynolds number $Re_\delta > 550$ for conditional turbulence in oscillatory flow or for a given

Womersley number and $Re_\delta < 550$ for weak turbulence[159]. Mean cross sectional CSF velocity at

peak systolic and diastolic flow, \bar{U}_{peak} , was computed at 1 mm slice intervals along the spine where

$\bar{U}_{peak} = \frac{Q_{peak}}{A_{cs}}$, with Q_{peak} defined as the maximum flow rate at peak systole and diastole at each slice.

Quantification of steady-streaming CSF flow

Oscillatory flow (zero mean flow) can result in steady-streaming due to nonlinear cumulative effects of convective acceleration[160]. To help quantify steady-streaming of CSF, the cyclic mean

velocity in the z-direction, U_{z-mean} , was computed for each node in the computational mesh. A positive

value for U_{z-mean} indicates steady-streaming in the rostral direction. U_{z-mean} was visualized at multiple axial slices and for a mid-sagittal slice.

The axial distribution of steady-streaming, $U_{ss}(z)$, was estimated by computing the cross-sectional average of U_{z-mean} magnitude:

$$U_{ss}(z) = \frac{\sum_{cell} |U_{z-mean}(z)| V(z)}{\sum_{cell} V(z)} \quad (22)$$

Where V is cell volume and the summations were conducted over every cell in the cross section. $U_{ss}(z)$ was calculated for z-slices at 1 mm intervals along the spine. To understand the affect

of NR on steady-streaming, $U_{ss}(z)$ and U_{z-mean} were compared for cases with and without NR. To further quantify the magnitude of steady-streaming flow, a non-dimensional fraction of the specified flow rate amplitude was defined as:

$$Q_{ss(z)} = \frac{U_{ss}(z)A_{cs}}{2Q_{peak}} \quad (23)$$

where Q_{ss} was divided by two to obtain a unidirectional steady-streaming flow rate because the positive flow is always equal the negative flow for a closed SSS.

Results

Numerical Sensitivity Studies

Numerical sensitivity study was confirmed based on an assumed error threshold of <5% under increasing degrees of resolution. Maximum z-velocity error for the fine versus X-fine grid was 4.4% and medium versus fine grid was 15.7% (**Table 2** and **Figure 2**). U_{z-mean} error was similar (<5% between the fine versus X-fine grid). Thus, subsequent sensitivity studies were carried out with the fine grid. A time-step size of 0.01 seconds (T/84) produced a maximum error of 2.7% for z-velocity and was selected for future studies. Similarly, cycle sensitivity results for unsteady z-velocity showed that z-velocity variation after the first cycle was negligible (~3.6%). Thus, results for the final CFD study were analyzed based on the second cycle with a fine grid and time-step size of 0.01 seconds (T/84).

Reproduction of MRI-derived In Vivo CSF Flow Measurements

Results showed a maximum flow rate error of 2.3% (**Figure 3**). This degree of error is similar to previous CSF flow studies [161]. The flow rate waveforms applied to the model had a similar amplitude to previous in vivo MRI studies [64, 162-164]. For those studies, mean velocity at peak systole near C2 vertebral level was ~2.5 cm/s. In the present model, the mean velocity at C2 was ~2.4 cm/s with NR and stroke volume at that location was 0.77 cm³.

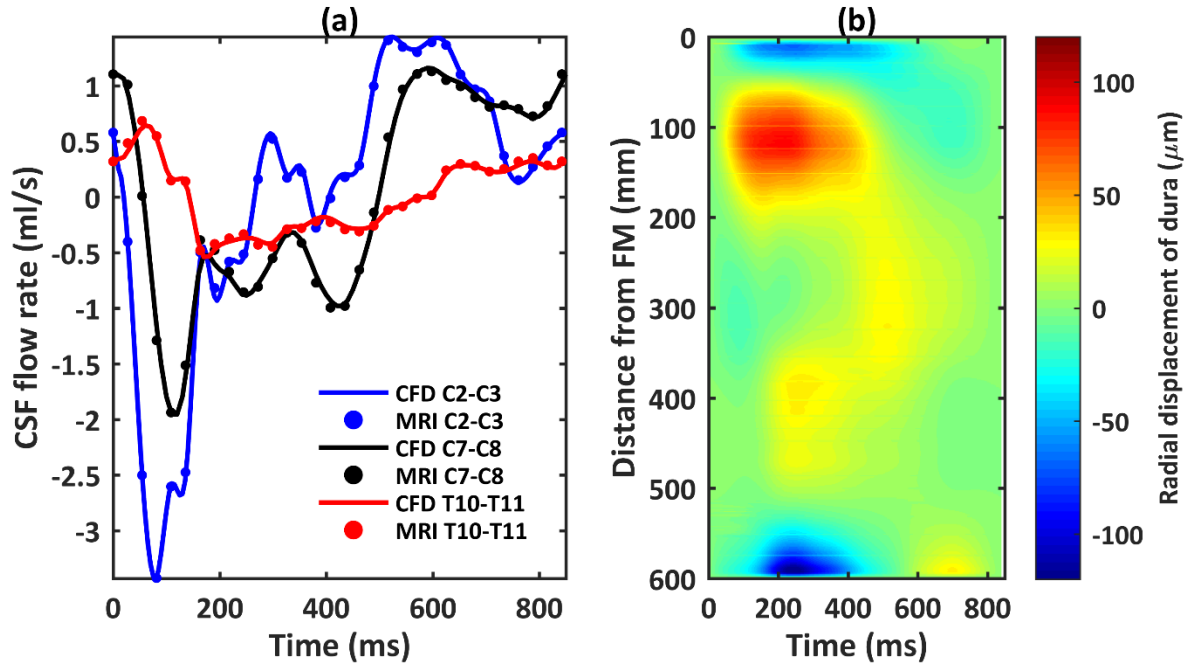


Figure 5.3. Comparison of numerical model axial flow rate distribution with subject specific PCMRI measurements. (a) CSF flow waveforms measured by PCMRI at three axial locations along the spine. Dots indicate experimental data and lines denote CFD results. Note: negative, or peak systolic, CSF flow is in the caudal direction. (b) Spatial-temporal distribution of the average dura radial displacement along the spine.

Hydrodynamic Parameters

Hydrodynamic results are reported in detail for the 3D model with NR only. CSF volume within the SSS from the FM to spinal sac was 97.3 ml at the beginning of cardiac systole ($t=0$). Spinal cord and NR volumes were constant at 19.9 and 5.8 ml, respectively. Peak CSF velocity showed maximum values in the cervical spine of 3.9 and 2.9 cm/s for the cases with and without NR, respectively (**Figure 4a**). Cross-sectional area was reduced with NR by up to 13.8% (**Figure 4b**). Maximum of the cross-sectional mean velocities, \bar{U}_{peak} , from MRI data (interpolated flow) were present at the cervical spine near the C4-C5 level (**Figure 3a**). Minimum \bar{U}_{peak} occurred in the lower thoracic spine about 40 cm below the FM (~T11-T12). Hydraulic diameter, omitting the filum terminale, had a minimum value of 3.4 mm occurring at a distance of 95 mm caudal to the FM within the cervical spine (**Figure 4c** – y-axis left). Hydraulic diameter was larger at both the FM and within the thoracic spine than elsewhere. Womersley number ranged from 22.96 to 1.64 (**Figure 4c** – y-axis right). Local maxima for Womersley number were present within the FM level ($\alpha = 23.0$) and at the thoracic spine ($\alpha = 16.1$). Womersley

number had local minima within the cervical spine and just rostral to the intrathecal sac. Maximum Re with NR was 184 (**Figure 4d**) and located in the cervical spine where the SSS had a relatively small hydraulic diameter and peak flow rate was maximum. Maximum Re_{NR} , Re_{δ} and Keulegan–Carpenter number was 78.2, 14.2 and 30.8 ($\beta = 3.8$), respectively (**Figure 4e and f**).

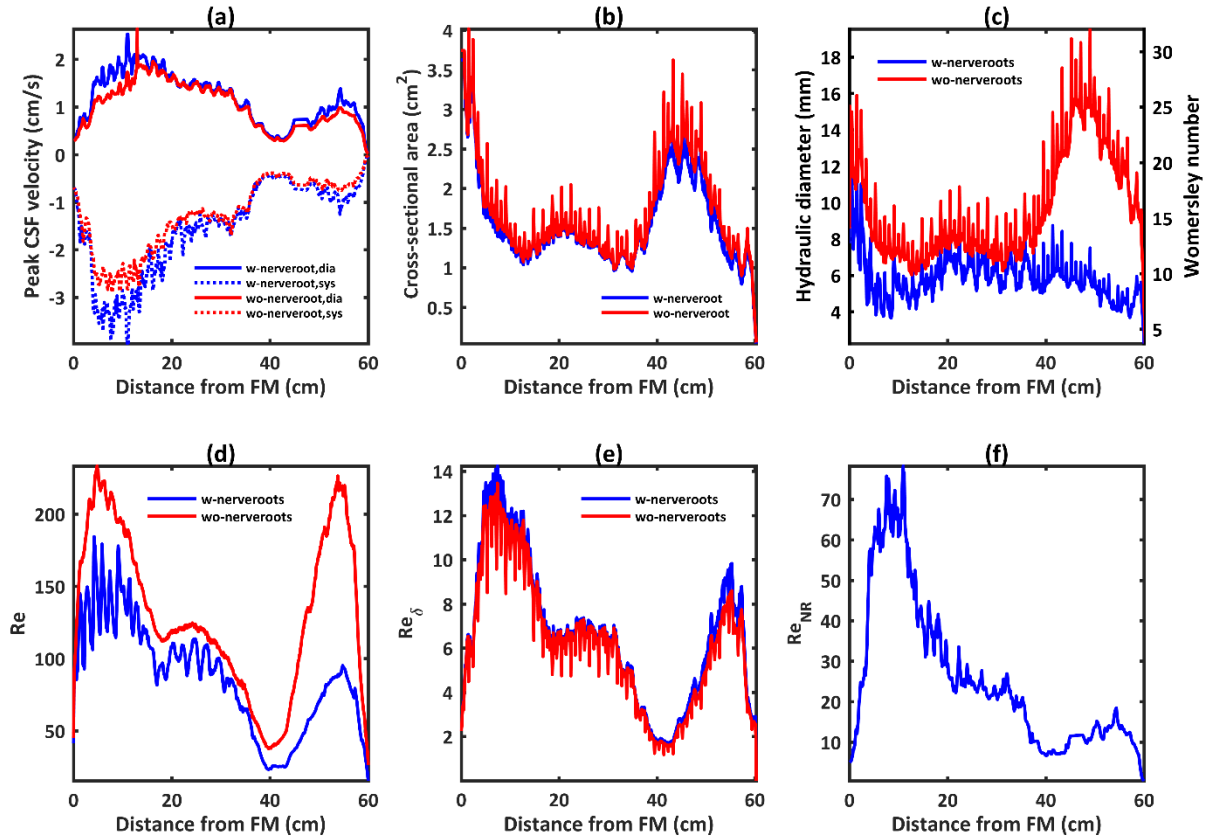


Figure 5.4. Hydrodynamic parameter distribution computed along the spine in terms of: (a) peak CSF velocity, (b) cross-sectional area (c) hydraulic diameter and Womersley number, α , (d) Reynolds number, for internal flow within a tube, Re , (e) Stokes-Reynolds number based on Stokes-layer thickness, Re_{δ} , (f) Reynolds number for external flow over a NR, Re_{NR} .

CSF flow, Velocities and Flow Features

Comparison of flow rates at the three MRI slice locations (**Figure 3a**) showed that CFD results were nearly identical to MRI measurements (error < 2.3%), verifying the dural motion inputs. Peak flow rates at C2-C3, C7-C8 and T10-T11 were 3.44, 1.95 and 0.53 ml/s, respectively. Stroke volumes at these locations were 0.77, 0.69 and 0.25 ml, respectively. Spatial-temporal distribution of dura radial

displacement over the cardiac cycle showed that maximum dural displacement was 122.52 μm and located at 595 mm below the FM (**Figure 3b**). Average dural displacement along the entire spine was 16.41 μm . Note, interpolated values of dural displacement should not be used for model validation purposes. The empirical data is only derived from MRI measurements at the three axial levels investigated.

Velocity profiles at $T = 90$ ms (peak systole, **Figure 5**) in the coronal, sagittal and axial planes exhibited peaks in the cervical spine. Note: peak systolic timing was obtained for CSF flow at C2-C3. Depending on the timing, the velocity profile changes due to non-uniform deformation of the dura. The axial distribution of peak CSF velocities over the entire cardiac cycle is shown in Figure 4a. As expected, spinal cord NR decreased nearby velocities and resulted in “jets” between dorsal and ventral NR pairs in the cervical spine (**Figure 5c**, C5-C6 level). Note, to better visualize results along the entire spine, **Figure 5** and similar figures are contracted at $\frac{1}{2}$ scale in the z-direction (maximum spine curvature with respect to the z-axis is <15 degrees). At peak flow (**Figure 6a**), the CSF velocity profile on the posterior side of the spinal cord and between NR showed a characteristic “m-shaped” profile (Figure 6b).

Recirculation and vortices occurred upstream, downstream, within and around dorsal and ventral NR bundles within the cervical spine depending on the location and phase of the cycle (**Figure 6c**). Vortices were not present in the thoracic and lumbar spine where the NRs are oriented in a streamwise direction. These vortices formed at time points corresponding to flow reversal (**Figure 6a** at T_1 , T_3 and T_4). Vortices did not form at peak flow rate (T_2) when flow streamlines were more uniformly axial.

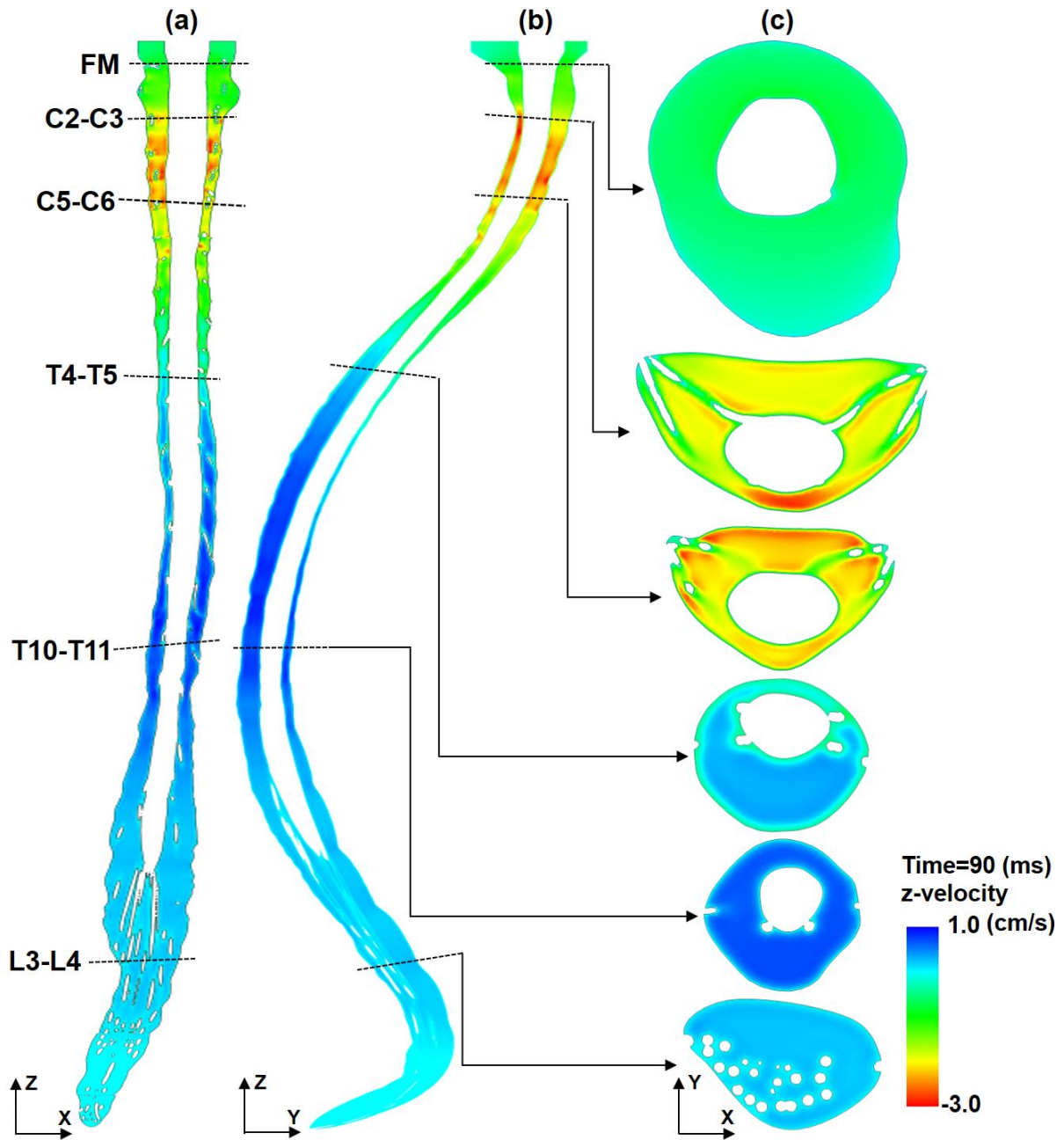


Figure 5.5. Thru-plane CSF velocity profiles simulated by CFD at $T=90$ ms for three different views: (a) coronal, (b) sagittal and (c) axial at six slice locations. Note: peak systolic timing was obtained for CSF flow at C2-C3. The axial distribution of peak CSF velocities over the entire cardiac cycle is shown in Figure 4a. Also, to help visualize the entire spine, z-scaling of the geometry is set at 0.5 with respect to x and y-dimensions. Thus, spine curvature appears greater than without scaling.

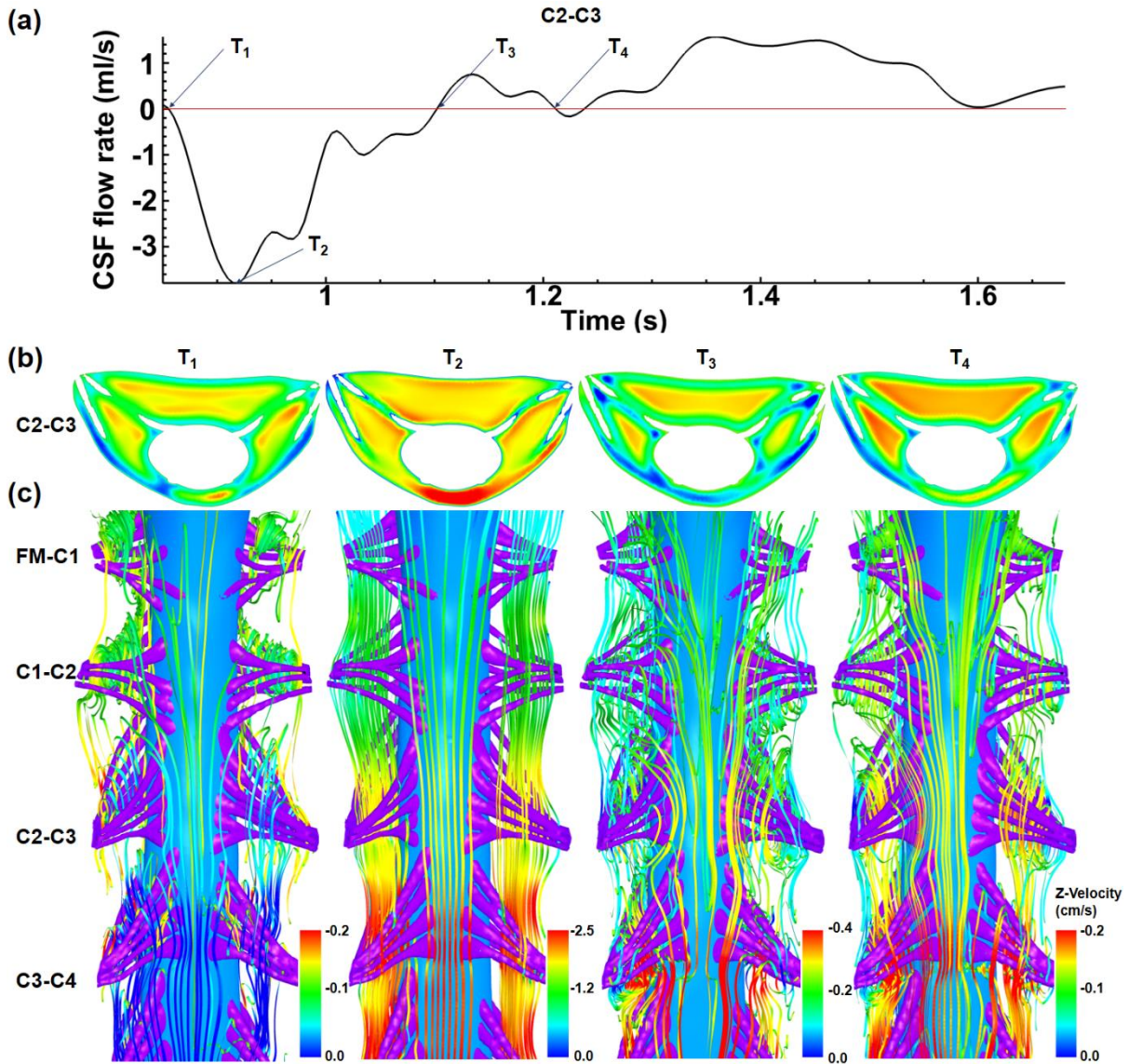


Figure 5.6. Vortices form around spinal cord NR in the cervical spine at time-points corresponding to CSF flow reversal. (a) CSF flow rate at C2-C3 section and (b) velocity contour for C2-C3 section and (c) streamlines showing vortices that form around NR pairs (FM-C1, C1-C2, C2-C3 and C3-C4) at four different time steps. The interfaces of these vortices are located upstream and downstream of NR pairs. Note: velocity scales are different for each time point.

Steady-streaming CSF Velocity Quantification

The presence of spinal cord NR was found to have a large impact on U_{z-mean} and $U_{ss}(z)$. Overall, NR resulted in greater steady-streaming velocity magnitude and more complex steady-

streaming velocity profiles (compare **Figure 7 and 8**). The coronal U_{z-mean} velocity profile (**Figure 7a**) indicated rostral streaming near NR. With NR present, the sagittal U_{z-mean} velocity profile (**Figure 7b**) exhibits a large region of caudally directed steady-streaming in the posterior SSS in the middle thoracic spine and anterior SSS in the cervical spine. In addition, streaming “pockets” were visualized on axial slices (**Figure 7c**) and were located laterally between dorsal and ventral NR at the interface of adjacent vortices (**Figure 6c**). These features changed considerably without NR present (**Figure 8a**). For example, CSF streaming pockets were still present (**Figure 8b**), albeit, located anterolaterally to the spinal cord and with a lesser steady-streaming velocity magnitude (**Figure 8c**). Similar to with NR, rostral-directed streaming was present in the dorsal thoracic SSS and somewhat in the ventral cervical SSS (**Figure 8b**). Relatively little steady-streaming was present in the lumbar spine.

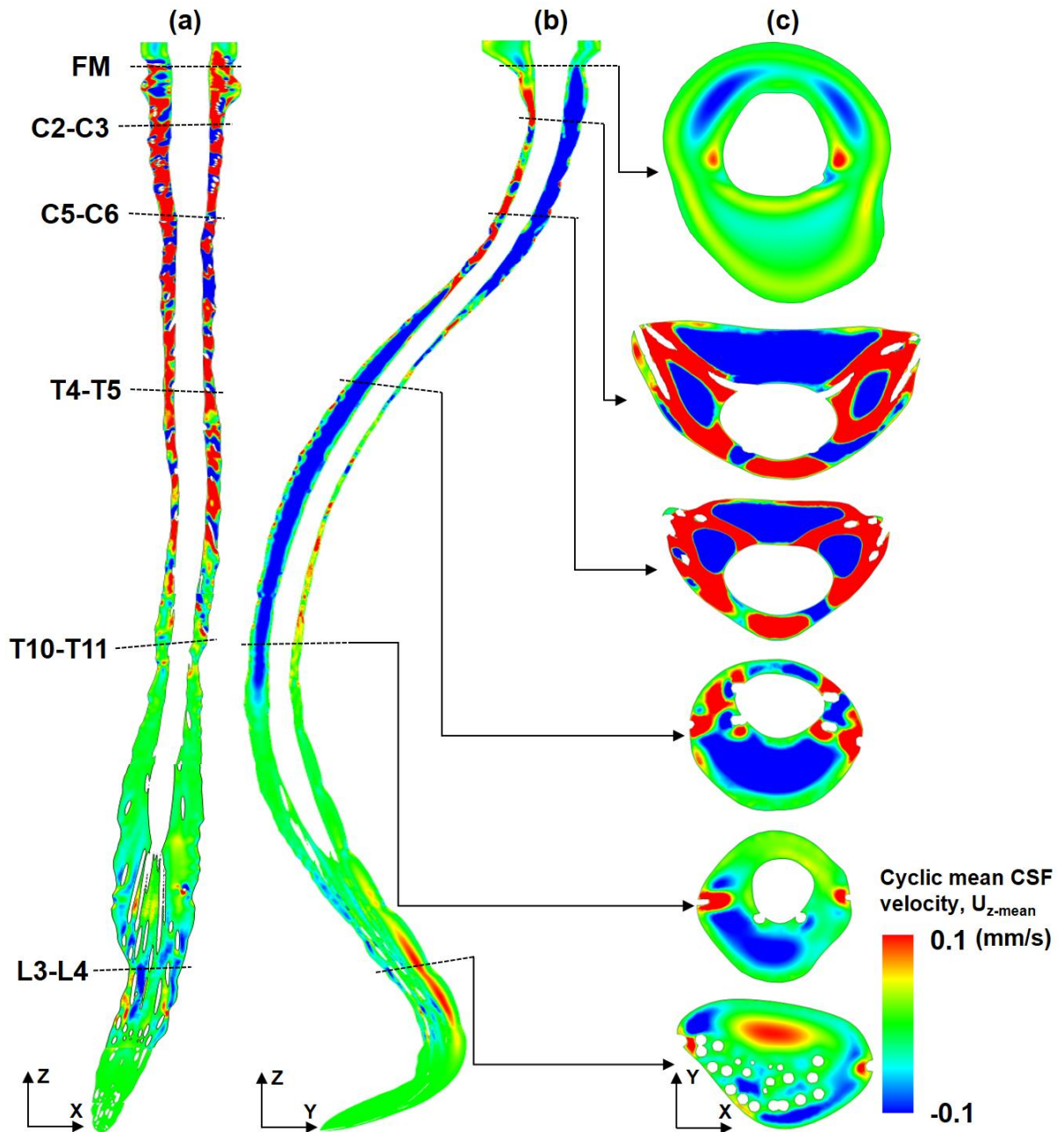


Figure 5.7. Presence of spinal cord NR result in a complex distribution of cyclic mean CSF velocities within the SSS. Cyclic mean CSF velocity profiles, U_{z-mean} , simulated by CFD for three different views: (a) coronal, (b) sagittal, (c) axial at six slice locations. Note: Cyclic mean CSF velocity is calculated based on one complete CSF flow cycle.

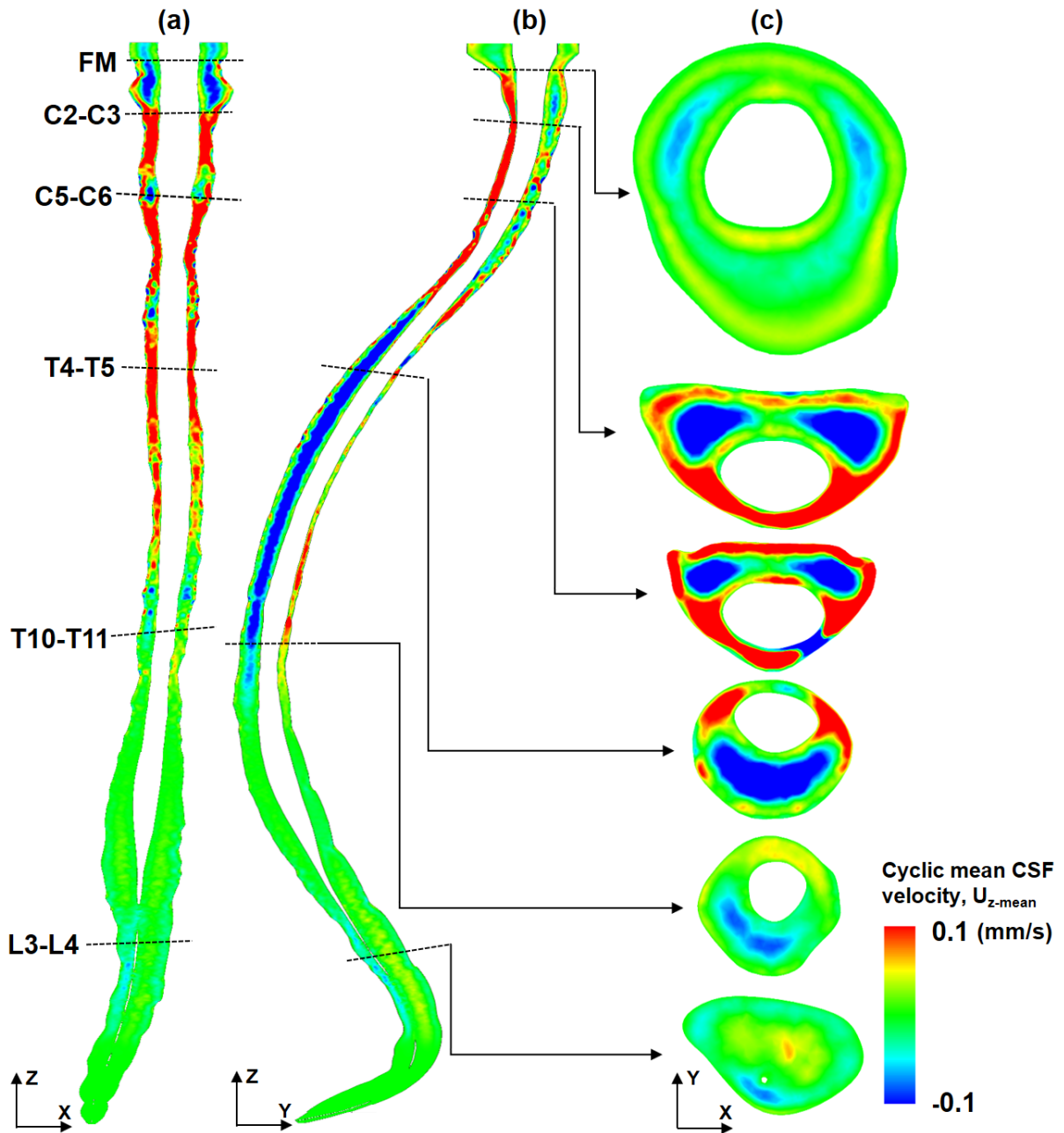


Figure 5.8. Cyclic mean CSF velocities decrease and change profiles without NR present in the numerical model. CSF cyclic mean velocity profiles, U_{z-mean} , for the case without spinal cord nerve roots at three different views: (a) coronal, (b) sagittal, (c) axial at six slice locations. Compare profiles to Figure 7 to see impact of NR.

The presence of NR increased steady-streaming CSF velocity magnitude, $U_{ss}(z)$, to a great degree within the cervical spine and to a lesser degree in the thoracic and lumbar spine (**Figure 9**). Average value for U_{ss} was 0.11 ± 0.12 and 0.05 ± 0.04 mm/s (mean \pm stdev) for the model with versus without NR (120% greater with NR). The region of greatest difference in U_{ss} values was the cervical spine that had up to 5X larger value of U_{ss} with NR compared to without. On closer inspection, it was noted that the local regions of elevated U_{ss} were located between spinal cord NR in the region located from C1 to T2 (see vertical dotted lines in **Figure 9**). These localized increases were not present elsewhere along the spine. Q_{ss} (**Figure 9** – right axis) showed a nearly identical trend as U_{ss} . The average value for Q_{ss} was 0.023 ± 0.026 and 0.012 ± 0.009 (mean \pm stdev) for cases with and without NR.

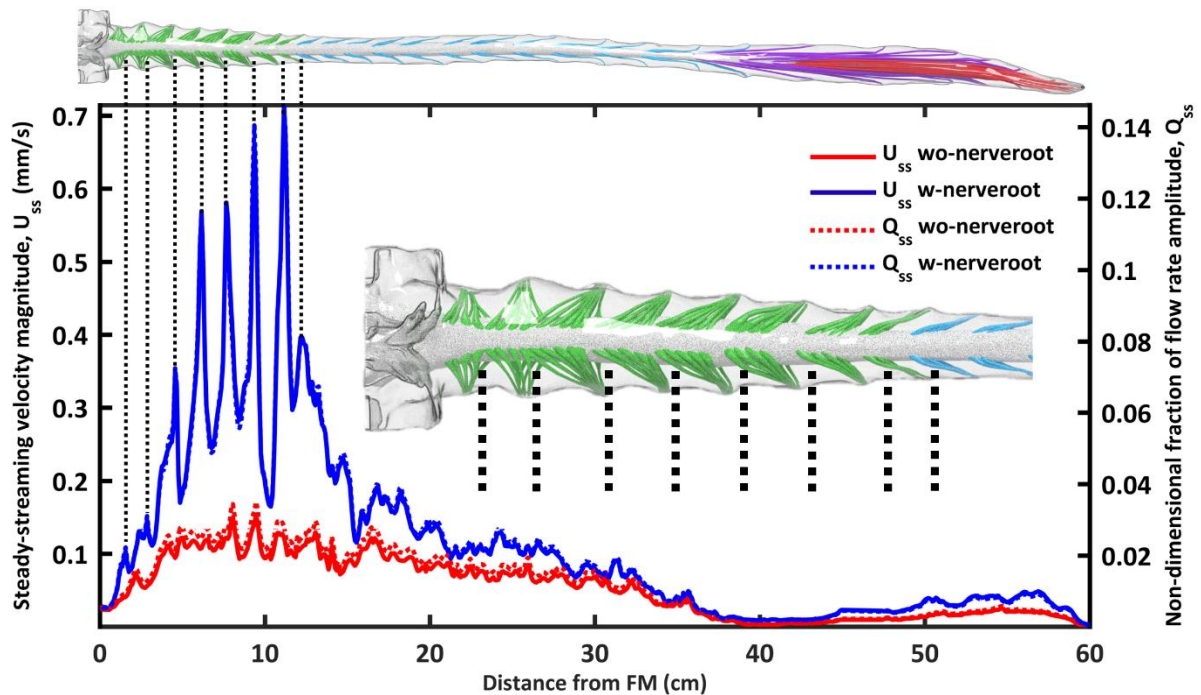


Figure 5.9. Steady-streaming velocity magnitude, U_{ss} , and non-dimensional fraction of flow rate amplitude, Q_{ss} , increases with NR compared to without NR. Dotted lines indicate that maximum U_{ss} occurs upstream / downstream of NRs in the cervical spine at the interface of adjacent vortices (see vortices in Figure 6c)

Discussion

The presence of spinal cord NR has an important impact on CSF flow dynamics in terms of velocities and steady-streaming effects.

Moving Boundary Mesh to Reproduce Subject Specific CSF Flow Distribution

Spatial-temporal interpolation of MRI-measured flow rates resulted in simulated velocities that were in opposing directions along the spine at some time points (**Figure 5a** and **b** plotted at T=90 ms). Maximum deformation of the dura was 122.52 μm and located in the cervical spine (**Figure 3b**). This value is lower than the threshold that is possible to detect by current 3T anatomic MR imaging resolution. Therefore, because dural motion was specified and verified based on CSF flow waveforms, uncertainty remains about the validity of the exact velocity profile results.

Spinal cord NR Impact CSF Hydrodynamics

The presence of NR decreased D_H , Re and α (**Figure 4**). NR increased cross-sectional mean velocity and area by up to 13.8%, as dictated by the reduction in cross-sectional flow area. Peak CSF velocities increased by up to 70%, indicating that the velocity increase was greater than what can be attributed to reduction in cross-sectional area with NR (**Figure 4b**). Axial distribution of these parameters had larger variation in the cervical spine due to the transverse orientation of NR that resulted in local reduction in SSS cross-sectional area (**Figure 1c** and **Figure 4b**). In the thoracic and lumbar spine, NR were oriented parallel to the flow direction and, therefore, had a smaller impact on axial variation in Re . Assessment of Re likely indicated laminar flow (<184 for model with NR). Re increased without NR present due to a larger hydraulic diameter in that case, in particular in the dural sac of the lumbar spine (**Figure 4c**).

The measured values for hydrodynamic parameters in this study are within the range of previously published studies [64, 165] (**Table 1**). In specific, maximum Re was reported to be 187 by Pahlavian et al. [76], 150-450 by Loth et al. [64] and 140 by Martin et al. [59] in CFD models of the cervical spine. These values support that CSF flow is likely laminar. These and the value measured for our subject, $Re < 250$, suggest that the flow, were it steady, would be laminar. Although it should be noted that SSS geometry is complicated with multiple levels of anatomic complexity that include tiny anatomic structures such as arachnoid trabeculae and denticulate ligaments. Anatomic complexity can lead to flow instabilities at $Re > 600$ in a stenosis [166], at Re in the range of 200 – 350 in aneurysms

[167, 168], in the heart [169] and within CSF in the SSS [139, 170]. Sources of flow instability related to nerve roots are discussed in the next section (Vortices Form Around Cervical Spinal Cord NR During CSF Flow Reversal). In addition, the unsteadiness of the flow presents a different set of turbulent transition criteria. The Stokes-Reynolds number, Re_δ , was less than 14.2, which is below the threshold of 550 for conditional turbulence in oscillatory flow [159]. On the other hand, the Womersley number was greater than 5, which places the flow in the weakly turbulent flow regime. Weak turbulence is characterized by instabilities that appear during flow acceleration and disappear during deceleration [159]. Generally, for pulsatile flow, the instabilities appear on deceleration and disappear during acceleration. This is due to the unfavorable pressure gradient in deceleration and a favorable pressure gradient in acceleration.

Velocity profiles showed similar presence of localized flow jets (**Figure 5**) similar to previously published studies [5, 73, 165]. However, the NR in the present study were modeled as anatomically realistic individual rootlet fibers. Previous studies [67, 76] idealized NR as airfoil- or rod-shaped structures.

Vortices Form around Cervical Spinal Cord NR during CSF Flow Reversal

The finding of transient vortices in the vicinity of NR during deceleration (**Figure 6c**) may be consistent with the appearance of instabilities in oscillatory flow around cylinders. Such instabilities have been documented in a number of experiments for large β and small K , and the critical Keulegan–Carpenter number for these limits has been calculated as: $K_{cr} = 5.778\beta^{-1/4}(1 + 0.205\beta^{-1/4})$ given by Hall [158]. Thus for the current results, for which $\beta = 3.8$, K_{cr} has a value of 1.18. The value for the current results, $K = 30.8$, is well above this threshold. However, the results do not conform to the large β and small K limits. Therefore, the occurrence of Honji-type instabilities [157] in the SSS is uncertain. If such instabilities exist, the flow rate waveform applied in our study had multiple points of flow reversal and, therefore, multiple periods during which vortex formation could affect mixing. Honji rolls have also been shown to induce transverse streaming [171], which would tend to increase longitudinal dispersion. We hypothesize that this and other factors causing flow reversal and vortical structures, e.g., medical device interventions or abdominal maneuvers, etc., could be leveraged to increase flow mixing to a therapeutic degree, in particular within the cervical spine. Further, the presence of adjacent vortices may be leveraged to increase axial solute transport within the SSS due to “blinking” vortex formation [172, 173].

The observed vortical structures around NR in our model (**Figure 6**) are in a different location than the vortices reported by Pahlavian et al.[76]and Tangen et al.[132] who found vortices located between axial NR (e.g. between C1 and C2 NR). The difference in vortex location is likely due to the more idealized NR geometry applied by Pahlavian et al. that modeled NR as airfoil-shaped structures with a greater thickness than the current study. Also, Tangen et al. had all NR in the model oriented relatively orthogonal to the primary flow direction (see Figure 4, Tangen et al.). This resulted in vortex formation throughout the spine. In our model, vortices were only observed in the cervical spine where NR were oriented relatively orthogonal to the primary flow direction (**Figure 6c**) and did not appear in the lumbar or thoracic spine (**Figure 1c**). It should be noted, our current model lacked denticulate ligaments located between NR pairs. These ligaments may impact flow to some degree and therefore could alter where vortices are located in the present model.

NR Increase Steady-streaming CSF Dynamics

NR increased steady-streaming velocity magnitude, $U_{ss}(z)$, to a great degree within the cervical spine and to a lesser degree in the thoracic and lumbar spine (**Figure 9**). Local elevation of U_{ss} was located within the spaces above or below NR (see spikes in the blue curve for the case with NR, **Figure 9**). These values coincided with more complex mean z-velocity profiles and increased the value of U_{z-mean} for the case with NR (**Figure 7**) compared to without NR (**Figure 8**). We hypothesize that these regions are due to adjacent “blinking” vortices [173, 174] that touch in the space above or below NR. It may be possible to leverage the location of this increased steady-streaming transport to assist solute spread in the SSS (e.g. inject medication at this location).

To put numbers in context, the maximum value of U_{ss} was only 0.15 mm/s without NR and 0.71 mm/s with NR (**Figure 9**) compared to mean velocities (at peak systole) up to ~25 mm/s. Thus, for the presented model boundary conditions, U_{ss} was more than 35X smaller than transient velocities. In addition to steady-streaming, Tangen et al. [67, 132] found CSF pulsation magnitude to play an important role on SSS transport. CSF pulsation magnitude in combination with flow reversals might be optimized to increase SSS mixing.

U_{z-mean} profiles (Figure 7 and 8) show that NR impact the distribution of cyclic mean CSF velocities around the spinal cord (axial orientation), but the overall streaming structures in the sagittal orientation are similar both with and without NR. For example, the caudal directed flow in the posterior thoracic

spine with NR (**Figure 7b** – negative values) was still present in the model without NR (**Figure 8b**). Also, in the coronal orientation (**Figure 7a** and **8a**), rostral-streaming flow was located laterally with and without NR present. Thus, since the overall posterior versus anterior steady-streaming flow profiles were relatively unaffected by presence of NR, it is possible that posterior versus anterior steady-streaming profiles may be due to eccentricity of the flow cross-section and spine curvature. However, NR did affect steady-streaming velocity profiles lateral to the spinal cord (Figure 7c versus 8c). We hypothesize that changing eccentricity and spinal curvature (kyphosis / lordosis) could be applied strategically to direct steady-streaming solute transport. Steady-streaming of CSF flow has been previously reported by Kuttler et al.[133] in an eccentric SSS. However, quantitative results were not provided in that study and therefore are not comparable to the present work. Kuttler applied the steady-streaming velocity field as a “frozen flow field” and used it with the molecular diffusion equation to solve for drug transport along the SSS. This approach should be tested against in vitro experiments for validation.

Limitations

This study included one healthy adult volunteer as a platform to analyze the impact of NR on the CSF flow field. As such, the results are subject-specific. We expect that the exact values could change considerably with alterations in flow waveform shape and amplitude as well as overall SSS geometry for different subjects. Shifting of the brain and/or spinal cord position due to posture changes was not analyzed. This study did not take into account the impact of other fine structures within the SSS, such as arachnoid trabeculae, blood vessels and denticulate ligaments.

We sought to verify the model with in vivo subject specific measurements of CSF flow rate at three axial locations along the spine. Results showed <2.3% error. A more accurate model would measure flow rate at additional axial levels. Our approach was to deform the dura to match MRI-derived CSF flow. In reality, it is possible that the dura does not deform at all, but rather, veins within the CSF are compressed. With current MR imaging techniques it is difficult to verify what is the exact location of deformation. The MRI measurements conducted in this study did not allow direct validation of steady-streaming velocity results as these were <1 mm/s. This value is below MRI velocity detection limits that typically are set at 5 cm/s for phase-contrast MR imaging studies.

A source of error in the comparison of U_{ss} between cases with and without NR is that cross sectional area was reduced with NR, which increased the cross sectional mean velocities (given that CSF flow rate was imposed identically across the two simulations). Maximum percent area of the SSS

occupied by the NR was 13.8% (average percent NR area over the entire SSS was 5.5%). Therefore comparison of Q_{ss} , which is normalized by the imposed flow rate, is more valid. Q_{ss} increased a maximum of 434% with NR compared to without NR (average increase in Q_{ss} was 91%). This supports that the relatively small change in SSS cross-sectional area due to NR does not on its own account for the relatively large increase in Q_{ss} with NR.

The z-slice orientation through the model was orthogonal to the z-axis. Thus, since the spine has curvature, the values for U_{ss} are not computed exactly in the streamwise direction. We estimated that the maximum angle of the spine with respect to the z-axis is <15 degrees (omitting lumbar spine where nearly zero flow velocities were present). This would result in a maximum U_{ss} error of 3.4%. Note: To help visualize the entire SSS, **Figure 5, 7 and 8** are scaled at 0.5X in the z-axis, making the spine curvature appear more curved than actual.

Conclusion

A subject-specific model of the complete SSS with anatomically realistic NR and accurate reproduction of non-uniform flow rate was used to investigate the impact of NR on CSF dynamics. NR were found to alter CSF dynamics in terms of velocity field, steady-streaming and vortical structures. Vortices occurred in the cervical spine upstream and downstream of NR during CSF flow reversal. Steady-streaming increased with NR, in particular within the cervical spine. These findings suggests that future studies should investigate how solute transport within the SSS could be increased and/or controlled by: a) delivery of solutes either upstream or downstream of NR, b) control of CSF pulse magnitude and/or number of flow reversals per cardiac cycle, c) changing eccentricity or spinal curvature (kyphosis / lordosis).

Chapter 6: Impact of Neurapheresis system on intrathecal cerebrospinal fluid dynamics: a computational fluid dynamics study

Abstract

It has been hypothesized that early and rapid filtration of blood from cerebrospinal fluid (CSF) in post-subarachnoid hemorrhage patients may reduce hospital stay and related adverse events. In this study, we formulated a subject-specific computational fluid dynamics (CFD) model to parametrically investigate the impact of a novel dual-lumen catheter-based CSF filtration system, the NeurapheresisTM system (Minnetronix Neuro, Inc., St. Paul, MN), on intrathecal CSF dynamics. The operating principle of this system is to remove CSF from one location along the spine (aspiration port), externally filter the CSF routing the retentate to a waste bag, and return permeate (uncontaminated CSF) to another location along the spine (return port). The CFD model allowed parametric simulation of how the Neurapheresis system impacts intrathecal CSF velocities and steady-steady streaming under various Neurapheresis flow settings ranging from 0.5 to 2.0 ml/min and with a constant retentate removal rate of 0.2 ml/min. simulation of the Neurapheresis system were compared to a lumbar drain simulation with a typical CSF removal rate setting of 0.2 ml/min. Results showed that the Neurapheresis system at a maximum flow of 2.0 ml/min increased average steady-streaming CSF velocity 2X in comparison to lumbar drain (0.190 ± 0.133 versus 0.093 ± 0.107 mm/s, respectively). This affect was localized to the region within the Neurapheresis flow-loop. The mean velocities introduced by the flow-loop were relatively small in comparison to normal cardiac-induced CSF velocities.

Introduction

Subarachnoid hemorrhage (SAH) is a severe and often-fatal incident [175], in which blood is released into the cerebrospinal fluid (CSF) due to intracranial insult, ruptured intracranial aneurysm, and/or other head trauma. Permanent disability, stroke, hydrocephalus, and even death can occur if the blood flow is not re-established. Standard of care for SAH patients typically involves: a) securement of the aneurysm, b) pharmacologic therapies targeted at neural protection (such as calcium-channel blockers, e.g. nimodipine), c) attempt to control the relationship between cerebral perfusion (via hypertension, hypervolemia, and hemodilution therapy, collectively termed “triple-H” [176]), and d) relief of high intracranial pressure (ICP) via pharmacologic and interventional approaches. After securement of a ruptured aneurysm, the body is susceptible to inflammation related complications as it

breaks down and reabsorbs any remaining blood from the subarachnoid space. As such, patients are closely observed in the hospital for 10-14 days to monitor for high ICP, cerebral vasospasm, edema and hydrocephalus.

It has been hypothesized that early and rapid filtration of blood and blood breakdown byproducts (e.g. hemoglobin and other inflammatory mediators) post-SAH may reduce the incidence of stroke, cerebral vasospasm [177], hydrocephalus / permanent shunting, and/or shorten hospital course[178-181]. **Table 1** summarizes clinical studies involving removal of blood from the CSF in terms of clearance modalities, population, and observed outcomes. Reduction in the incidence of these complications would, in principle, reduce length of stay, decrease utilization of hospital resources, improve clinical functional outcomes, and have an overall reduction of healthcare economic burden. This hypothesis has been studied utilizing various blood removal techniques such as intracranial cisternal drainage [182, 183], cisternal lavages [184, 185], external-ventricular drains, lumbar drains [186-193], or a combination of drainage scenarios[194, 195]. Cisternal lavages involve irrigation of the cranial cisterns and ventricles with artificial CSF intended to flush out blood. Cisternal lavage may be combined with administration of thrombolytic agents directly to the site of clot formation[196-199]. Vibratory motion of the head coupled with cisternal lavage has been investigated a potential method to improve blood clearance rates[200, 201]. Another study developed a simplified in vitro model of the basal cistern from medical images, and demonstrated that head ‘shaking’ can accelerate clearance due to increased mixing[202]. At present, there is no consensus on the best protocol for blood clearance to mitigate post-aneurysm securement complications.

Table 6.1. Summary of clinical studies focused on clearance of blood from the CSF post-subarachnoid hemorrhage.

Author	Study inhabitants	Primary outcome measure	Primary outcome (Percent (%))
Maeda et al.[191]	LD=34 vs. EVD=17	Favorable outcome	LD=64.7, EVD=23.5
Klimo et al.[189]	LD=81 vs. Control=86	Vasospasm risk reduction	LD FG3=68, LD FG3+4 =49
Al-Tamimi et al.[186]	LD=105 vs. Control=105	Prevalence of DIND	LD=21, Control=35
Park et al.[193]	LD=126 vs. Control=8	Vasospasm	LD=19, Control=42
Kwon et al.[190]	LD=47 vs. Control=60	Vasospasm	LD=23, EVD=63
Kawamoto et al.[201]	CI + Shake=114 vs. CI=116	Vasospasm	CI + Shake=14, CI=26
Mizoi et al. [198]	CI + IT tPA=30 vs. CI=75	Vasospasm	CI + IT tPA=13, CI=15

Key: CI = Cisternal infusion, DIND = Delayed Ischemic Neurological Deficits, EVD = external-ventricular drain, IT tPA = Intrathecal injection of tissue-type plasminogen activator, LD = Lumbar drain, Shake = head shake during procedure, Fixed = head held in fixed position during procedure.

A computational model of CSF filtration could help understand and optimize blood clearance from the CSF system . At present, only one published computational model of CSF filtration using an anatomically idealized geometry has been brought forth by Tangen et al. [18] . This novel study provided information about the potential of CSF filtration to assist with blood removal. Empirical models limit our ability to investigate CSF filtration technologies, highlighting the need for a computational tool. Human clinical trials have been conducted (PILLAR trial [203, 204]), but these studies lack real-time visualization of blood distribution and are only able to sample CSF from select locations. A rabbit model for filtration of cryptococcal meningitis from CSF has been brought forth, but requires modifications to the system and approach due to a small subarachnoid space [205]. Also, in principle, a nonhuman primate experimental model of SAH could be developed, but such primate studies are expensive, only available at limited research centers, and have different CSF dynamics than humans [91, 92, 150, 206].

Thus, the present study objective was to formulate a computational model of CSF filtration incorporating a novel dual-lumen CSF flow looping catheter, also termed “Neurapheresis” therapy (**Figure 1**) [205]. In brief, Neurapheresis therapy involves aspiration of CSF from the lumbar spinal subarachnoid space (SSS), filtration of CSF pathogens specific to the disease, removing it to a waste bag, and then return of the CSF to the SSS at the thoracic spine. The different location of the aspiration and return port results in an induced CSF flow between the ports. We sought to first investigate the impact of the Neurapheresis system on CSF flow velocities and steady-streaming, as it is not yet known what impact Neurapheresis therapy has on these parameters under different operating conditions and how it compares to lumbar drain devices for SAH blood removal.

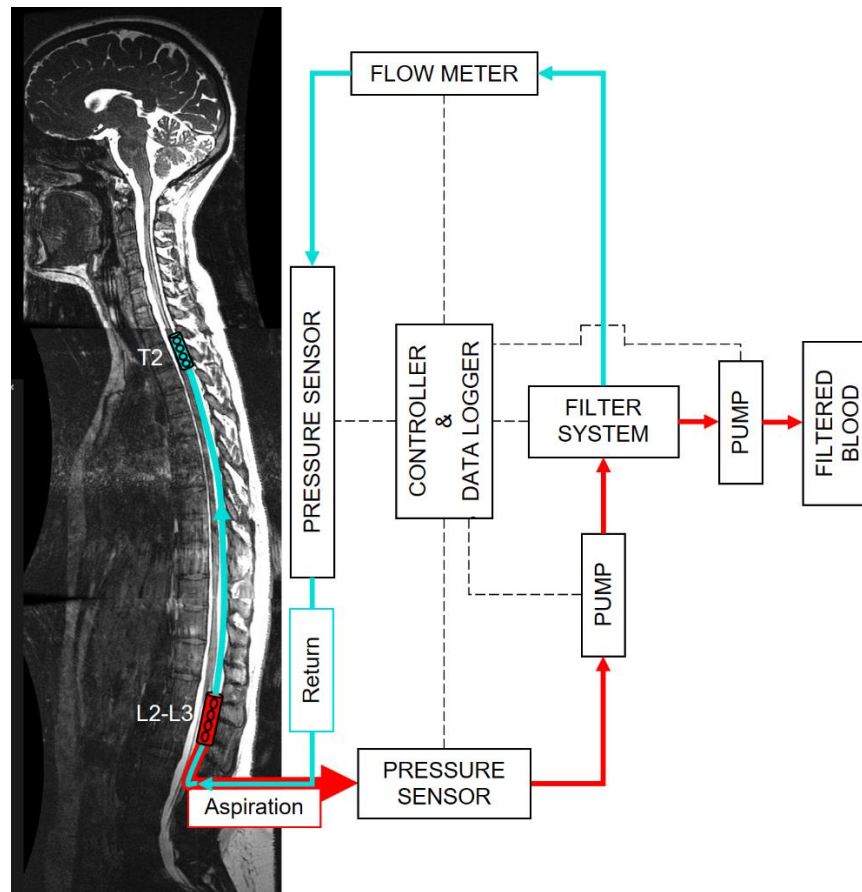


Figure 6.1. Schematic of the neurapheresis filtration system. CSF is removed from the lumbar spine at the aspiration port of a dual lumen intrathecal catheter. Blood is then removed from the CSF by the external filtration system. The filtered fluid is then returned to the CSF system in the upper thoracic spine via the dual lumen catheter. Note: the flow rate of fluid returned to the system is slightly less than that aspirated due to the loss of volume removed by the filtration system. The loss in fluid is compensated for by production of CSF within the ventricles.

Methods and Materials

To study the impact of the CSF filtration system (**Figure 1**), a CFD model was built to represent SSS anatomy with the Neurapheresis dual-lumen catheter located at the midline of the dorsal subarachnoid space (**Figure 2**). In summary, the CFD model involved: 1) specification of the SSS geometry based on anatomic MR imaging and dual-lumen catheter shape, 2) specification of flow boundary conditions, 3) analysis of CSF velocities with Neurapheresis therapy applied and, for comparison, with lumbar drain alone.

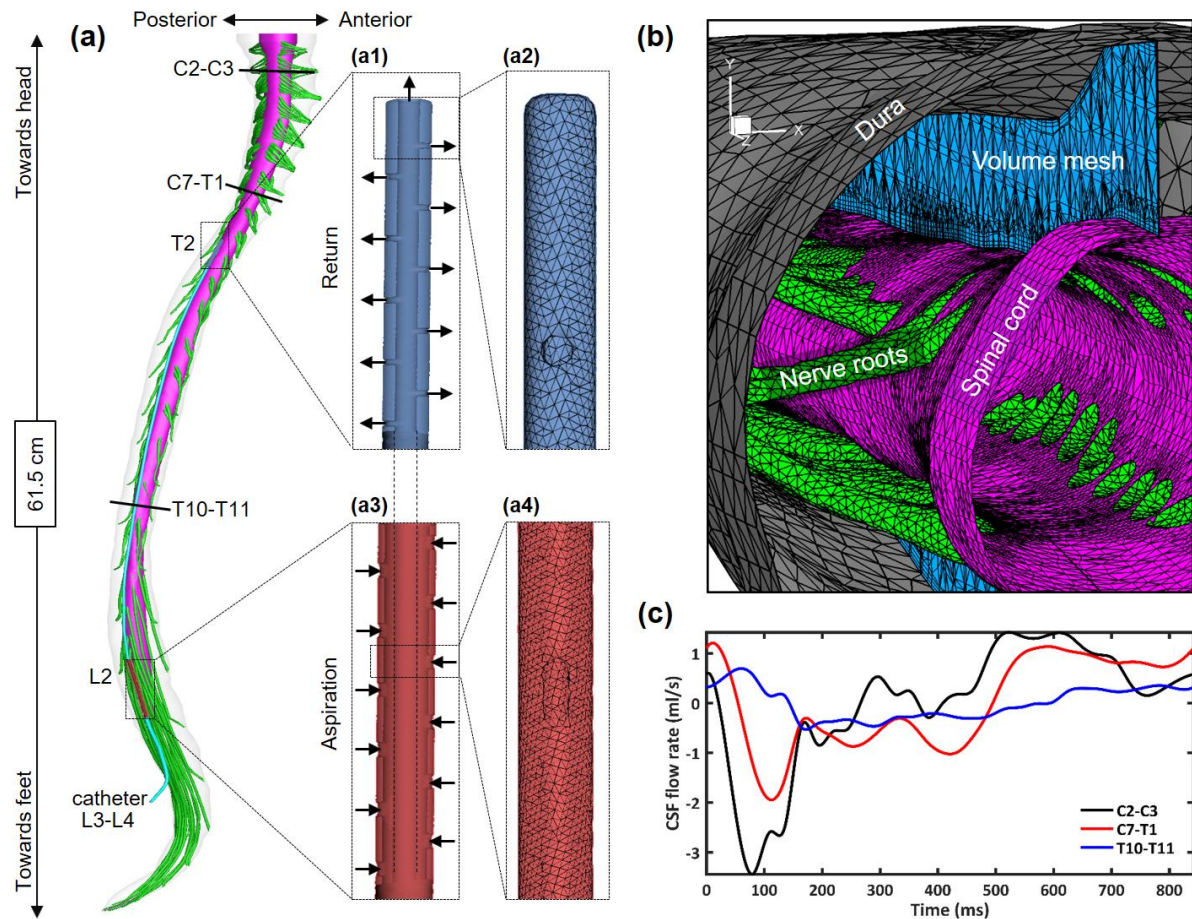


Figure 6.2. (a) overview of three-dimensional CFD model of the subarachnoid space with inserted Neurapheresis catheter. (a1–a4) Details of computational meshes for the Neurapheresis catheter: (a1) Magnified view of the return port with arrows indicating flow direction. (a2) Magnified view of the surface mesh near the return port catheter tip. (a3) Magnified view of the aspiration port with arrows indicating flow direction. (a4) Magnified view of the surface mesh near the aspiration port. (b) Volumetric and surface mesh visualization with zoom of the upper cervical spine. (c) Subject-specific CSF flow rates imposed by the computational model based on in vivo phase-contrast MRI measurements obtained at C2-C3, C7-T1, and T10-T11 vertebral levels.

Specification of Model Geometry

For the model geometry, we utilized a previously developed anatomically realistic open-source 3D intrathecal space model with spinal cord nerve rootlets [150]. In brief, the magnetic resonance imaging (MRI) protocol and image segmentation methods used to form the anatomic boundaries for the model are described in detail by Khani et al.[91, 92] and Sass et al.[150]. In brief, T2-weighted anatomic MRI was acquired for a 23-year-old female volunteer using a 3T MRI system (**Figure 1**). The MR images were manually segmented by an expert trained operator to define the spinal cord and dura geometry along the spinal axis. 31 pairs of idealized dorsal and ventral spinal cord nerve roots were added to the model based on the MR imaging and review of the literature related to cadaveric measurements of nerve root radicular line, descending angle, and other geometric features[150].

A dual-lumen catheter geometry was added to the posterior SSS at the L3-L4 level and positioned at the midline (**Figure 2**). The posterior SSS was chosen for catheter placement since the catheter would be inserted posteriorly via a lumbar puncture needle. Also, the dorsal subarachnoid space posterior to the cord is wider than the ventral subarachnoid space. Thus, the catheter is most likely to naturally position within that region of the SSS. The catheter termination was located at the T2 vertebral level. The catheter has a 5 French outer diameter that tapers to approximately 3 French near the distal (thoracic placed) end. The catheter had two series of holes located 300 mm apart, designed for redundancy to avoid the case of blockage or clogging. The holes located near the catheter termination (T2) allowed fluid to return from the filtration system and enter the SSS (return, **Figure 2a1** and **a2**). The proximal holes located near L2 allowed aspiration of fluid from the SSS to the filtration system (**Figure 2a3** and **a4**).

An unstructured tetrahedral computational mesh of the SSS and dual lumen catheter was generated using the ANSYS ICEM software (ANSYS Inc., version 19.1, Canonsburg, PA, USA) (**Figure 2b**). The computational mesh was refined near the catheter return and aspiration ports to have a final mesh of 14.8 M cells.

Specification of CFD Model Flow Boundary Conditions

Flow boundary conditions were specified to reproduce subject-specific non-uniform CSF flow along the spine (**Figure 2c**) and the catheter system aspiration and return flow rates. Thus, we applied our previously developed method for non-uniform dura deformation to reproduce subject-specific CSF flow along the spine [91, 92]. In brief, this method involved a user-defined function that introduces spring-based mesh deformation of cells near the dura to reproduce the local CSF flow waveforms that are measured by MRI. Stroke volume was 0.76 mL per cardiac cycle at the C2-C3 level with a non-uniform decline in amplitude caudally along the spine (**Figure 2c**).

Boundary conditions were applied to represent the catheter flow at the aspiration and return port under varying flow rates while maintaining a fixed difference between the two, called the waste rate, of 0.2 ml/min (**Table 2**). “Maximum Flow” represented Neurapheresis flow with an aspiration and return flow rate of -2.0 and +1.8 ml/min, respectively. The net direction of the induced flow was craniocaudal (\downarrow), where negative values represent fluid removal from the system and vice versa. The return rate was not identical to aspiration, as blood is filtered out of the CSF and diverted to waste (**Figure 1**) and therefore, return flow rate is equal to the aspiration flow rate minus the waste rate. Also, it is expected that for safety reasons, the magnitude of CSF volume removal should not exceed CSF production rate that is estimated to be ~500 ml/day or 0.35 ml/min [117]; in practice this is often translated to a lumbar drainage rate of ~10 ml/hr to remain below this production rate. “Low Flow” was similar to Maximum Flow except with a 4X reduced aspiration rate of -0.5 ml/min and a corresponding 6X reduced return rate (0.3 ml/min) to maintain a waste rate of 0.2 ml/min. To help understand the impact of induced flow direction, aspiration and return locations were inverted in “Reverse Flow”. In “Dynamic Mesh Off”, we turned off the dynamic mesh motion to help understand the individual impact of CSF pulsation compared to Neurapheresis therapy on its own. “No Flow” was conducted with the induced flow turned off to show the effect of the presence of the catheter alone. “Lumbar Drain” was applied to represent a lumbar drain with a typical aspiration rate of 0.2 ml/min. For that case, the catheter geometry remained within the SSS, but the return port was turned off, thus only allowing CSF to be drained from the port at the lumbar region. This case provides a baseline for the cases with nonzero return flow.

Table 6.2. Average steady-streaming velocity magnitude, $U_{ss}(z)$, and non-dimensional fraction of flow rate amplitude, $Q_{ss}(z)$, for the simulations analyzed.

Name	Mean \pm std (mm/s)	Mean \pm std
Maximum Flow	0.190 \pm 0.133	0.154 \pm 0.138
Low Flow	0.105 \pm 0.103	0.063 \pm 0.030
No Flow	0.088 \pm 0.108	0.041 \pm 0.026
Lumbar Drain	0.093 \pm 0.107	0.048 \pm 0.023
Dynamic Mesh Off	0.130 \pm 0.135	0.129 \pm 0.155
Reverse Flow	0.174 \pm 0.115	0.143 \pm 0.139

The simulated transient flows resulted in a net flow into the SSS of 0.2 ml/min from the cranial opening due to the difference in aspiration and return flow rates (for all cases except No Flow). This flow rate of 0.2 ml/min is approximately equivalent to the assumed CSF production rate. The model outlet was specified as a zero pressure outlet with fluid free to enter / exit at the outlet. We did not simulate how decreasing SSS volume would affect intracranial pressure. The focus of this study was on the flow-loop's affect on transient CSF velocities and steady streaming within the spine.

CSF was modeled as an incompressible fluid with a density of 993.8 kg/m³ and viscosity of 0.693 mpa.s (equivalent to water at body temperature) [62, 149]. Unsteady CSF velocity field was computed using ANSYS Fluent 19.1 (ANSYS Inc., version 19.1, Canonsburg, PA, USA) by solving the continuity equation (Eq. 1), and Navier–Stokes equation (Eq.25) where ρ is the density, μ is the viscosity, $\vec{u}(\vec{x}, t)$ is the velocity vector and p is the pressure field.

$$\vec{\nabla} \cdot [\rho \vec{u}(\vec{x}, t)] = 0 \quad (24)$$

$$\rho \frac{\partial \vec{u}}{\partial t} + \rho \vec{u} \cdot \vec{\nabla} \vec{u} = -\vec{\nabla} p + \vec{\nabla} \cdot \mu \vec{\nabla} \vec{u} \quad (25)$$

Details on mesh, cycle, and time-step independence studies for this model with non-uniform dura deformation and anatomically realistic nerve roots is provided in our previous research [92]. Results were obtained for the second flow cycle with a time-step size of 0.01 s (total cardiac cycle = 0.85 s), second-order momentum and pressure gradient solver, and convergence criteria of 1E-06 for velocity, continuity and momentum.

Analysis of CSF Velocities

CSF flow was quantified in terms of axial distribution of Reynolds number, $Re(z)$, and velocity contours around the catheter aspiration and return ports. $Re(z)$ was calculated as

$$Re(z) = \frac{|Q_{max}(z)| D_H(z)}{\nu A_{cs}(z)},$$

where $D_H(z)$ is hydraulic diameter, $|Q_{max}(z)|$ is the absolute value of the peak flow rate, $A_{cs}(z)$ is the cross-sectional area at each 1 mm slice along the z-axis and ν is kinematic viscosity. Velocity streamlines were visualized based on line sources located within the catheter lumen proximal to the return and aspiration holes.

As detailed in our previous study [92] and by others[160], oscillatory flow within an eccentric annulus can result in steady-streaming CSF velocities due to convective acceleration. To visualize steady-streaming along the spinal axis, the cyclic mean z-velocity, U_{z-mean} , at each node was calculated. The cross-sectional steady-streaming velocity magnitude was also calculated as:

$$U_{ss}(z) = \frac{\sum_{cell} |U_{z-mean}(z)| V(z)}{\sum_{cell} V(z)} \quad (26)$$

Where $|U_{z-mean}(z)|$ is the absolute value of U_{z-mean} in the z-direction and $V(z)$ is the cell volume at each axial location along the z-axis. To see the effect of different Neurapheresis scenarios, $U_{ss}(z)$ and U_{z-mean} were compared for all cases (**Table 3**). $U_{ss}(z)$ is impacted by the cross-sectional area. Thus, as described in our previous study, a non-dimensional fraction of flow rate amplitude, $Q_{ss}(z)$, was computed as:

$$Q_{ss}(z) = \frac{U_{ss}(z)A_{cs}}{2Q_{max}(z)} \quad (27)$$

In this study, the Neurapheresis therapy itself was called “Steady” flow, because steady-streaming only relates to time average flow produced within an oscillatory flow field. Since the Neurapheresis catheter only makes a static flow field, it is by nature, just a “steady” flow driven by source and drain.

Results

CSF Flow Velocities

For Maximum Flow, maximum Re was 180 and located within the cervical spine (**Figure 3a**). Visualization of unsteady CSF velocity contours in the sagittal plane (**Figure 3b**) showed that peak CSF velocities occurred in the cervical spine. Unsteady CSF velocity magnitudes were nearly identical across all cases (not shown). CSF velocity profiles near the aspiration and return ports showed that most of the flow into and out of the domain originated from the first four holes at the return port and the first two holes at the aspiration port, respectively (**Figure 3b1 to 3b4**).

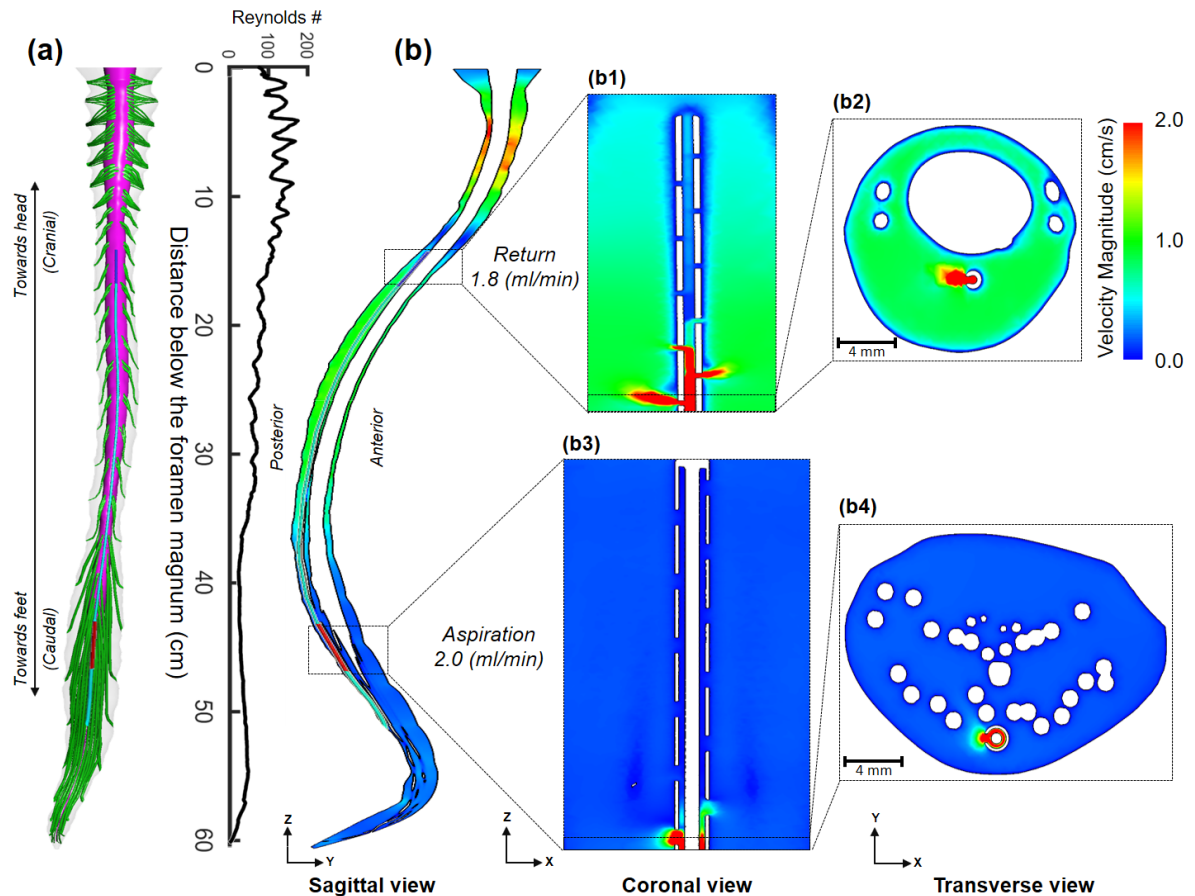


Figure 6.3. (a) Reynolds number distribution computed along the spine for the Maximum Flow simulation. (b) Visualization of sagittal velocity magnitude profiles simulated by CFD at 0.06s time-point (**Figure 2c**). (b1) Magnified coronal view of the return port. (b2) Magnified transverse view of the CSF flow field near the return port showing diffusivity of the returned flow near the first hole (b3) Magnified view of the aspiration port. (b4) Magnified transverse view of the CSF flow field near the aspiration port. Note: To help visualize the entire spine, z-scaling of the geometry is set at 0.5 with respect to x and y-dimensions. Thus, spine curvature appears greater than without scaling.

Steady-streaming CSF Velocity Quantification

The Neurapheresis flow loop altered U_{z-mean} velocity profiles within the catheter flow loop region, depending on rate and direction (Figure 4). U_{z-mean} velocity profiles were affected little outside of the flow loop region (above the return port and below the aspiration port) for all cases analyzed. Lumbar Drain had a lower impact on steady streaming in comparison to Maximum Flow, Low Flow, and Reverse Flow. No Flow was most similar to Lumbar Drain. Neurapheresis flow reversal (Reverse Flow) drastically altered the direction of U_{z-mean} . The sagittal U_{z-mean} velocity profiles for Maximum Flow, Low Flow, No Flow, and Lumbar drain (**Figure 4**) showed a region of caudally directed (\downarrow) U_{z-mean} in the posterior SSS in the middle thoracic spine and in the anterior SSS in the cervical spine. Reverse Flow showed a similar trend, but with an opposite cranial direction (\uparrow) within the catheter region. Dynamic Mesh Off showed similar U_{z-mean} values within the catheter region, but U_{z-mean} was decreased in the region cranial to the return port compared to Maximum Flow.

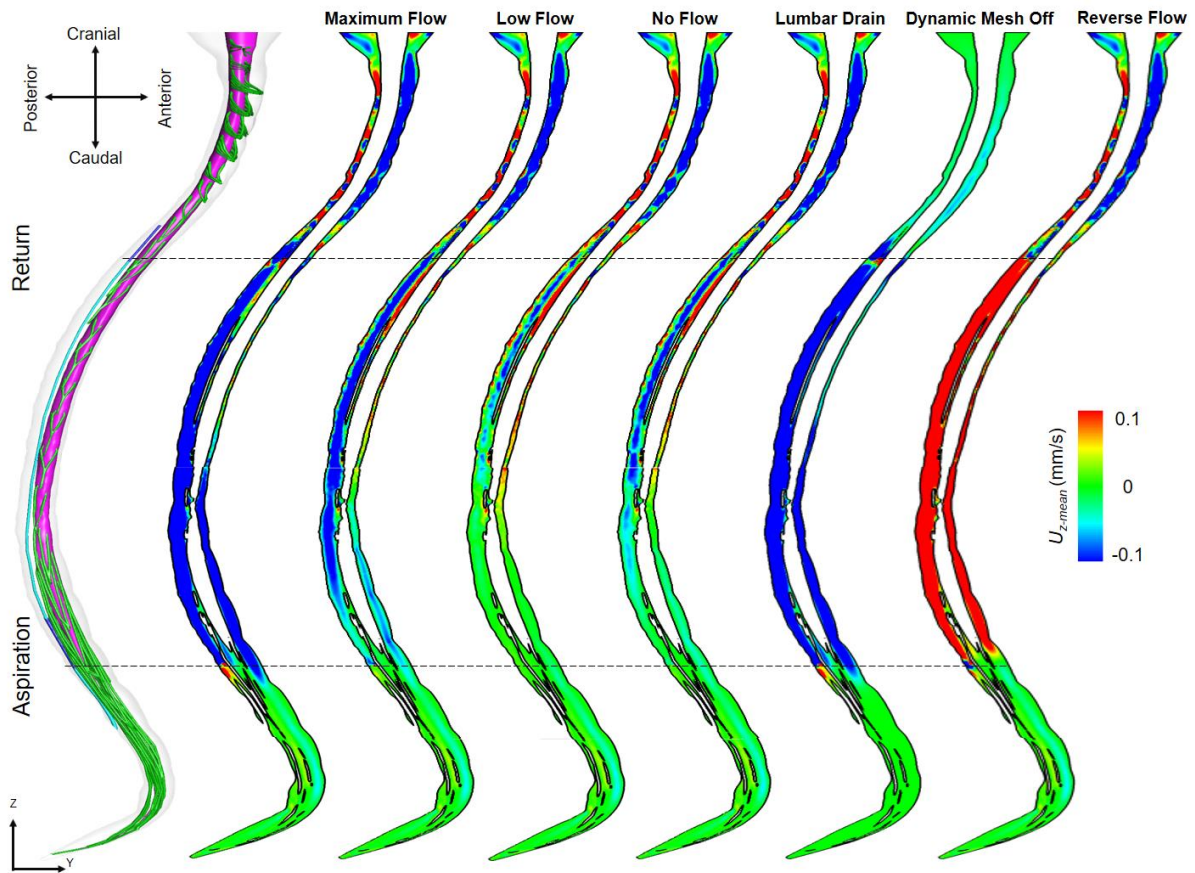


Figure 6.4. Visualization of mid-sagittal steady-streaming CSF velocity profiles for all cases analyzed (**Table 2**). Steady-streaming CSF velocities, U_{z-mean} , increase with Neurapheresis therapy (Maximum Flow, Low Flow, Reverse Flow, and Dynamic Mesh Off) compared to lumbar drain (Lumbar Drain) and with Neurapheresis therapy off (No Flow). Placement of return and the aspiration ports shown with dotted lines for reference. Note: To help visualize the entire spine, z-scaling of the geometry is set at 0.5 with respect to x and y-dimensions. Thus, spine curvature appears greater than without scaling.

In comparison to Lumbar Drain, the cases for Maximum Flow, Low Flow, and Reverse Flow resulted in greater $U_{ss}(z)$ and $Q_{ss}(z)$ (Figure 5). For all cases with Neurapheresis flow applied, the increase in steady streaming had little impact outside of the catheter region. Greater Neurapheresis flow rate increased $U_{ss}(z)$ within the flow-loop region (Figure 5a). Average value for $U_{ss}(z)$ was 0.19 ± 0.13 and 0.09 ± 0.11 mm/s (mean \pm stdev) for Maximum Flow versus No Flow (Table 3). The region of greatest difference in $U_{ss}(z)$ values was located between the return and the aspiration ports in the thoracic and lumbar spine (T2-L2) that had up to 3X larger value of $U_{ss}(z)$ in Maximum Flow

compared to No Flow. $Q_{ss}(z)$ (Figure 5b) showed a trend similar to $U_{ss}(z)$ for Lumbar Drain compared to Low Flow. The average value for $Q_{ss}(z)$ was 0.154 ± 0.138 and 0.041 ± 0.026 for Maximum Flow and No Flow (**Table 3**).

Table 6.3. Specification of flow rates at the Neurapheresis catheter aspiration and return port.

Name	Type	Flow Direction	Aspiration (ml/min)	Return (ml/min)
Maximum Flow	Neurapheresis flow at maximum rate	↓	-2.0	+1.8
Low Flow	Neurapheresis flow at low rate	↓	-0.5	+0.3
No Flow	Neurapheresis therapy off	N/A	0.0	0.0
Lumbar Drain	Lumbar drain	↓	-0.2	0.0
Dynamic Mesh Off	Neurapheresis flow at maximum rate with No CSF pulsation	↓	-2.0	+1.8
Reverse Flow	Neurapheresis flow with reverse loop	↑	+1.8	-2.0

Key: + represents flow into the control volume, - represents flow out of the control volume, ↓ indicates flow loop applied in the craniocaudal direction, ↑ indicates flow loop applied in the caudocranial direction.

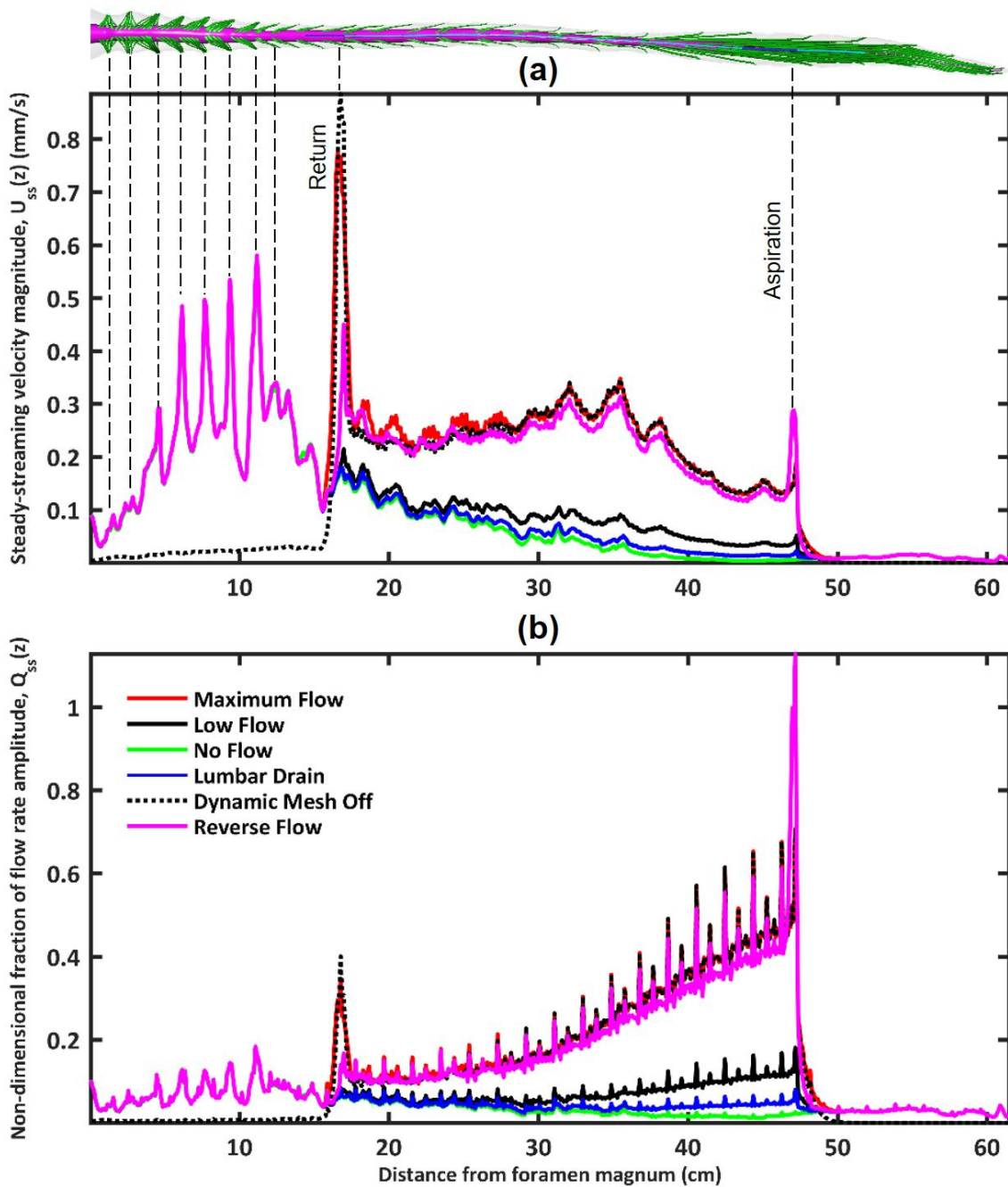


Figure 6.5. (a) Steady-streaming velocity magnitude, U_{ss} , and (b) non-dimensional fraction of flow rate amplitude, Q_{ss} , increases with Neurapheresis Therapy compared to lumbar drain only between the return and the aspiration ports. Dotted lines indicate that maximum U_{ss} occurs close to the aspiration and the return ports and at the cervical spine near the intersection of spinal cord nerve roots into the dura.

Discussion

The objective of the present study was to apply CFD modeling to investigate the impact of a dual-lumen CSF filtration catheter system, Neurapheresis therapy (**Figure 1**) [205], on intrathecal CSF velocities. The operating principle of this system is to introduce an intrathecal flow loop by a dual lumen catheter that removes CSF in the lumbar spine at an aspiration port, filters the CSF externally, and returns CSF to the upper thoracic spine via the same catheter. The return flow rate is not identical to the aspirated flow because some material is filtered out; in the case of SAH, that material is blood. We sought to parametrically quantify how the catheter system, operating under varying flow rates and flow directions, impacts intrathecal CSF velocities and steady-streaming flow dynamics [92] and compared results to a lumbar drain operating under a typical drain rate. The lumbar drain was selected for comparison because it is used in select centers for CSF blood removal post SAH (**Table 1**). CFD modeling was utilized to predict the catheter impact on CSF dynamics because invasive parametric studies are not feasible to conduct on SAH patients. Also, non-invasive measurement of CSF flow velocities by phase contrast MRI [207] are not accurate enough to quantify the relatively small alterations in net CSF flow velocities introduced by the flow loop system or lumbar drain.

Physiologic Performance Considerations

Neurapheresis therapy was found to have nearly zero impact on CSF velocities in comparison to normal cardiac-induced physiologic CSF movement. Therefore, it is not expected that these alterations to CSF velocities would, on their own, have ramifications to the normal physiology. Previous research has shown that peak cardiac-induced CSF velocities in healthy people range from 2-4 cm/s within the intrathecal space [88, 165, 208, 209]. Our findings show that Neurapheresis therapy induced CSF velocities (U_{z-mean}) do not exceed 0.08 cm/s for the Maximum Flow (**Figure 4**). These scale proportionately smaller for the Low Flow case. As such, these cross-sectional average velocities are 1 to 2 orders of magnitude smaller than normal peak cardiac-induced CSF velocities. Thus, for the boundary conditions applied in our study, it is likely that the impact of Neurapheresis flow is a relatively small change superimposed on normal cardiac pulsations. More information on Neurapheresis system safety in humans will be available following publication of the PILLAR trial (publication pending) and the ongoing Neurapheresis “PILLAR XT” clinical trial [204, 210].

Impact of Neurapheresis Flow on CSF Dynamics

Neurapheresis therapy increased U_{z-mean} and $U_{ss}(z)$ greatly within the space between the return and the aspiration ports and to a lesser degree everywhere else in the model (**Figure 4 and 5**). Local elevation of $U_{ss}(z)$ occurred near the first few return port holes that expelled >80% of the returning CSF (see the spikes highlighted with dotted lines in **Figure 5**). $U_{ss}(z)$ was much higher for the Maximum Flow compared to No Flow (**Figure 5**). To put the numbers in context, the maximum value of $U_{ss}(z)$ within the region between the infusion ports was only 0.17 mm/s without Neurapheresis therapy (No Flow) and 0.77 mm/s with Neurapheresis therapy (Maximum Flow) compared to peak cardiac-related CSF velocities that ranged up to ~25 mm/s. Thus, for the presented model boundary conditions, Neurapheresis therapy induced steady streaming velocities, $U_{ss}(z)$, were more than 35X smaller than normal physiologic cardiac related CSF velocities.

The effect of Neurapheresis system on steady-streaming was localized to the SSS region between the aspiration and return ports. Titration of Neurapheresis procedure rate showed a corresponding decrease in U_{z-mean} profiles and Reverse Flow showed a relatively equal, but opposite, effect on steady streaming compared to Maximum Flow between the aspiration and return ports (**Figure 4 and Figure 5**). All cases analyzed had nearly zero impact on streaming structures outside that region (above and below the ports). However, within the region above the return port, there is considerable steady streaming that is naturally introduced by the presence of vortices that form around spinal cord nerve roots due to CSF oscillations [76, 92]. This can be observed by comparing Maximum Flow to Dynamic Mesh Off (**Figures 4 and 5**). Further research is needed to understand how Neurapheresis flow impacts advection and removal of specific solutes from the CSF and what impact the waste and CSF production rate may have on results.

Comparison of Results to Previous Studies in the Literature

To our knowledge, one study has been previously conducted by Tangen et al. [18] to examine CSF filtration. For that study, Tangen et al. used a bench top and multi-phase CFD model to assess the efficacy of different lumbar drainage rates and patient orientations (incline, supine, upright) on blood removal from the CSF. The model used an anatomically idealized CSF system with cylindrical shaped spinal cord nerve roots and a rectangular-shaped intracranial compartment. They found that forced purification (lumbar to intracranial flow loop) in the upright position maximized blood clearance. CFD

results compared favorably with in vitro experiments with a similar geometry. It is not possible to compare our CFD model results to Tangen et al., since our focus was on the impact of Neurapheresis flow on intrathecal CSF velocities and steady-streaming transport and not on its affect on solute removal.

Prior literature has applied various geometric and flow boundary conditions. Our CSF velocity profiles showed similar flow fields (**Figure 3**) to previously published studies with spinal cord nerve roots [67, 76, 170, 211]. Additionally, the present model with a catheter, showed nearly identical results to our previous model having the same geometry, but without a catheter in place [92]. However, the previous studies incorporating spinal cord nerve roots did not investigate the impact of Neurapheresis flow or lumbar drain on CSF velocities. In both studies, we also utilized an anatomically realistic open-source 3D intrathecal space model with spinal cord nerve rootlets [150] and a non-uniform moving boundary motion of the dura to replicate subject-specific CSF flow along the SSS. An advantage of the open-source model is that it will allow direct comparison of CFD results of other researchers who use the model in the future. Future work may include building upon the model to understand impact on solute removal, validation of results against in vitro experiments, and comparison of CFD results using different solvers.

Potential Benefit of Neurapheresis System Computational Model for CSF Filtration Protocol and Device Development

The CFD model presented offers a platform to understand intrathecal device behavior as well as envision alternative Neurapheresis system protocols and devices. For example, the presented platform can help quantify how different catheter designs and implantation locations may affect CSF velocities. This model also allows alteration of the SSS geometry and CSF flow pulsation along the spine to determine their individual affects. These alterations are not possible to conduct within humans and are also difficult, if not impossible, within animal models. Our initial study design was to investigate Neurapheresis therapy under a variety of flow rates and different flow loop directions and compare results to a typical lumbar drain. Future studies are possible to conduct according to potentially-clinically relevant questions and/or CSF filtration device designs.

Limitations

Our focus was only on the SSS, since the Neurapheresis system was located within that space. Therefore, this study did not take into account the impact of the cranial SSS. This model also lacks some of the fine anatomical structures such as arachnoid trabeculae, blood vessels and denticulate ligaments. In addition, the catheter was positioned in the posterior SSS, because it is the most likely location where a catheter would be inserted. We did not investigate the impact of the catheter location around the spinal cord. Research has shown that catheter position can affect local solute distribution around the spinal cord on a small time scale (~ 1 s) [135]. It is unclear if these differences would propagate on a longer time scale.

We sought to verify the model with in vivo subject specific measurements of CSF flow rate at three axial locations along the spine. Our approach was to deform the dura to match MRI-derived CSF flow. In reality, it is possible that the dura does not deform at all, but rather, veins within the CSF are compressed. With current MR imaging techniques it is difficult to verify what is the exact location of deformation. Differences in the CSF pulse source location could, in principle, alter the results. Further study needs to be done to validate results against MRI data. There is nearly zero validation of results with in vivo data at this point.

The MRI measurements used for this study did not allow direct validation of steady-streaming velocity results as these were < 1 mm/s. Thus, the presented CSF velocity results are predictions to help elucidate the CSF velocities and steady-streaming flow patterns introduced by a CSF filtration device. Also, our modeling approach did not include respiratory component to CSF pulsations [120, 212, 213] because the MRI scanning time did not allow measurement of this parameter in addition to the other parameters used to formulate the model.

The present study focused on the impact of Neurapheresis system on CSF flow velocities (advection) within the spine and how that compares with a lumbar drain. For these simulations, we did not investigate the impact of concentration gradients on movement of actual solutes such as blood products or inflammatory cells and exudates. We also did not include how blood may alter CSF viscosity. CSF viscosity alterations and blood coagulation could change the results. The amount of blood in the CSF assumed in the model is small compared to the CSF volume (~ 300 mL) and not likely to significantly alter the viscosity. Further, as blood is slowly filtered out of the CSF, it is expected that CSF viscosity within the system could be time varying. The effect of gravity was not considered in this study since the density and viscosity of CSF was considered to be uniform in the model and the patient

was assumed to be in the supine position. However, in principle, gravity can have an impact on CSF viscosity distribution within the model. Taylor dispersion may affect how quickly blood is cleared from the CSF by enhancing solute spread within the cervical spine and also toward the aspiration port, as well as away from the aspiration port. Thus, consideration of advection only may overestimate actual blood clearance time.

Conclusion

Neurapheresis therapy may prove to assist removal of blood from CSF following SAH or enhance removal of other unwanted solutes. A subject-specific CFD model of intrathecal CSF dynamics was used to parametrically predict the impact of the Neurapheresis device on CSF dynamics under varying flow conditions. Results were compared to a typical lumbar drain used for blood removal from CSF. Neurapheresis therapy was found to significantly increase steady-streaming velocity magnitude compared to a lumbar drain. This effect was localized to the region within the Neurapheresis flow-loop. The mean velocities introduced by the flow-loop were small in comparison to normal cardiac-induced CSF velocities. Future multi-phase simulations will be conducted to simulate multi-phase solute transport for blood or other CSF solutes within the intrathecal space and validate model results against in vitro and/or in vivo measurements.

Chapter 7: Conclusion

In combination, this research presents an anatomically detailed and numerically and experimentally verified model for testing and optimization of CNS therapeutics and CSF filtration. An overall summary of key findings of this research is.

- 1) Non-uniform moving boundary method can reproduce in vivo CSF flow rate distribution and waveform along the spinal SAS of a cynomolgus monkey.
- 2) Methods presented demonstrate a reliable method for CSF quantification in NHPs
- 3) Steady-streaming increased with NR, in particular within the cervical spine.
- 4) Vortices occurred in the cervical spine upstream and downstream of NR during CSF flow reversal.
- 5) Neurapheresis therapy was found to significantly increase steady-streaming velocity magnitude compared to a lumbar drain.

For summary, in the first step, a subject specific CFD model was built based on a non-uniform moving boundary method to accurately reproduce in vivo CSF flow rate distribution and waveform along the spinal SAS of a cynomolgus monkey. Maximum error measured at peak CSF flow rate in the numerical model was <3.6%. Deformation of the dura ranged up to a maximum of 135 μm . MRI measurements of CSF space geometry and flow were successfully acquired to define the numerical domain and boundary conditions. For the single cynomolgus monkey analyzed, results showed that CSF flow was laminar with a peak Reynold's number of ~ 150 and average Womersley number of ~ 5.4 . Geometric analysis indicated that total spinal CSF space volume was ~ 8.7 ml. Average hydraulic diameter, wetted perimeter and SAS area was 2.9 mm, 37.3 mm and 27.2 mm^2 , respectively. CSF PWV along the spine was quantified to be 1.2 m/s and did not appear to have a significant degree of wave reflection at the spine termination. Maximum CSF flow movement was present at the C4-C5 vertebral level. In combination, these results represent the first CFD simulation of spinal CSF hydrodynamics in a monkey.

In the second step, a detailed geometric and hydrodynamic characterization of intrathecal CSF was performed for eight cynomolgus monkey (*Macaca fascicularis*) with reliability assessed between baseline and a two-week follow-up time point. Results showed laminar CSF flow along the entire spine with maximum CSF flow rate at the C3-C4 vertebral level and peak systolic CSF flow rate and stroke volume at C3-C4. The methods presented demonstrate a reliable method for CSF quantification in NHPs, which may extend in future studies to *Homo sapiens*.

In the third step, a subject-specific model of the complete SSS with anatomically realistic NR and accurate reproduction of non-uniform flow rate was used to investigate the impact of NR on CSF dynamics. NR were found to alter CSF dynamics in terms of velocity field, steady-streaming and vortical structures. Vortices occurred in the cervical spine upstream and downstream of NR during CSF flow reversal. Steady-streaming increased with NR, in particular within the cervical spine. These findings suggests that future studies should investigate how solute transport within the SSS could be increased and/or controlled by: a) delivery of solutes either upstream or downstream of NR, b) control of CSF pulse magnitude and/or number of flow reversals per cardiac cycle, c) changing eccentricity or spinal curvature (kyphosis / lordosis).

Finally, a subject-specific CFD model of intrathecal CSF dynamics was used to parametrically predict the impact of the CSF filtration device (Neurapheresis therapy) on CSF dynamics under varying flow conditions. Results were compared to a typical lumbar drain used for blood removal from CSF. Neurapheresis therapy was found to significantly increase steady-streaming velocity magnitude compared to a lumbar drain. This effect was localized to the region within the Neurapheresis flow-loop. The mean velocities introduced by the flow-loop were small in comparison to normal cardiac-induced CSF velocities. Future multi-phase simulations will be conducted to simulate multi-phase solute transport for blood or other CSF solutes within the intrathecal space and validate model results against in vitro and/or in vivo measurements.

References

1. Wostyn P, Audenaert K, De Deyn PP. More advanced Alzheimer's disease may be associated with a decrease in cerebrospinal fluid pressure. *Cerebrospinal fluid research*. 2009;6(1):1.
2. Takizawa K, Matsumae M, Hayashi N, Hirayama A, Yatsushiro S, Kuroda K. Hyperdynamic CSF motion profiles found in idiopathic normal pressure hydrocephalus and Alzheimer's disease assessed by fluid mechanics derived from magnetic resonance images. *Fluids and Barriers of the Cns*. 2017;14. doi: ARTN 29
10.1186/s12987-017-0077-y. PubMed PMID: WOS:000413216800001.
3. Martin BA, Labuda R, Royston TJ, Oshinski JN, Iskandar B, Loth F. Spinal Subarachnoid Space Pressure Measurements in an In Vitro Spinal Stenosis Model: Implications on Syringomyelia Theories. *J Biomech Eng-T Asme*. 2010;132(11). doi: Artn 111007
Doi 10.1115/1.4000089. PubMed PMID: ISI:000283740800007.
4. Yeo J, Cheng S, Hemley S, Lee BB, Stoodley M, Bilston L. Characteristics of CSF Velocity-Time Profile in Posttraumatic Syringomyelia. *American Journal of Neuroradiology*. 2017;38(9):1839-44. doi: 10.3174/ajnr.A5304. PubMed PMID: WOS:000409827200033.
5. Bunck AC, Kroeger JR, Juettner A, Brentrup A, Fiedler B, Crelier GR, et al. Magnetic resonance 4D flow analysis of cerebrospinal fluid dynamics in Chiari I malformation with and without syringomyelia. *European radiology*. 2012;22(9):1860-70.
6. Pahlavian SH, Loth F, Luciano M, Oshinski J, Martin BA. Neural Tissue Motion Impacts Cerebrospinal Fluid Dynamics at the Cervical Medullary Junction: A Patient-Specific Moving-Boundary Computational Model. *Ann Biomed Eng*. 2015;43(12):2911-23. doi: 10.1007/s10439-015-1355-y. PubMed PMID: 26108203; PubMed Central PMCID: PMC4626272.
7. Otto C. Fluid shifts in microgravity: The visual impairment and intracranial pressure syndrome in US astronauts. *Invest Ophth Vis Sci*. 2016;57(12). PubMed PMID: WOS:000394210605020.
8. Bradley Jr WG, Scalzo D, Queralt J, Nitz WN, Atkinson DJ, Wong P. Normal-pressure hydrocephalus: evaluation with cerebrospinal fluid flow measurements at MR imaging. *Radiology*. 1996;198(2):523-9.
9. Rassoli A, Nabaei M, Fatourae N, Nabaei G. Numerical modeling of the brain hypothermia by cooling the cerebrospinal fluid. *Tehran University Medical Journal*. 2017;75(1):31-8.
10. Kumar P, Srivatsava MV, Singh S, Prasad HK. Filtration of cerebrospinal fluid improves isolation of mycobacteria. *J Clin Microbiol*. 2008;46(8):2824-5. doi: 10.1128/JCM.00210-08. PubMed PMID: 18524968; PubMed Central PMCID: PMC2519457.
11. Urwin SC, Hunt P. Cerebrospinal fluid filtration in Guillain-Barre syndrome. *Anaesthesia*. 2000;55(5):503-4. PubMed PMID: 10792888.
12. Finsterer J, Mamoli B. Cerebrospinal fluid filtration in amyotrophic lateral sclerosis. *Eur J Neurol*. 1999;6(5):597-600. PubMed PMID: 10457394.
13. Brizzi M, Thoren A, Hindfelt B. Cerebrospinal fluid filtration in a case of severe pneumococcal meningitis. *Scand J Infect Dis*. 1996;28(5):455-8. PubMed PMID: 8953673.
14. Luciano MG, Dombrowski SM, Qvarlander S, El-Khoury S, Yang J, Thyagaraj S, et al. Novel method for dynamic control of intracranial pressure. *J Neurosurg*. 2017;126(5):1629-40. doi: 10.3171/2016.4.JNS152457. PubMed PMID: 27419825.
15. Stockman HW. Effect of anatomical fine structure on the dispersion of solutes in the spinal subarachnoid space. *J Biomech Eng*. 2007;129(5):666-75. doi: 10.1115/1.2768112. PubMed PMID: 17887892.
16. Stockman HW. Effect of anatomical fine structure on the flow of cerebrospinal fluid in the spinal subarachnoid space. *J Biomech Eng*. 2006;128(1):106-14. PubMed PMID: 16532623.
17. Tangen KM, Hsu Y, Zhu DC, Linninger AA. CNS wide simulation of flow resistance and drug transport due to spinal microanatomy. *Journal of Biomechanics*. 2015;48(10):2144-54. doi: 10.1016/j.jbiomech.2015.02.018. PubMed PMID: WOS:000358459800063.

18. Tangen K, Narasimhan NS, Sierzega K, Preden T, Alaraj A, Linninger AA. Clearance of Subarachnoid Hemorrhage from the Cerebrospinal Fluid in Computational and In Vitro Models. *Ann Biomed Eng.* 2016. doi: 10.1007/s10439-016-1681-8. PubMed PMID: 27384938.
19. Tangen K, Linninger A, Narasimhan NS. Clearance of subarachnoid hemorrhage from the central nervous system via lumbar drain - a bench-top and computational study. *Cerebrovasc Dis.* 2016;41:202-. PubMed PMID: WOS:000376023700264.
20. Mokri B. The Monro-Kellie hypothesis: applications in CSF volume depletion. *Neurology.* 2001;56(12):1746-8. PubMed PMID: 11425944.
21. Johnston M, Zakharov A, Koh L, Armstrong D. Subarachnoid injection of Microfil reveals connections between cerebrospinal fluid and nasal lymphatics in the non-human primate. *Neuropath Appl Neuro.* 2005;31(6):632-40. doi: 10.1111/j.1365-2990.2005.00679.x. PubMed PMID: WOS:000233170800008.
22. Davson H, Segal MB. *Physiology of the csf and blood-brain barriers*: CRC Press; 1995. [1040] pages p.
23. Segal MB. Extracellular and Cerebrospinal Fluids. *Journal of Inherited Metabolic Disease.* 1993;16(4):617-38. doi: Doi 10.1007/Bf00711896. PubMed PMID: WOS:A1993LT28800003.
24. Iliff JJ, Lee H, Yu M, Feng T, Logan J, Nedergaard M, et al. Brain-wide pathway for waste clearance captured by contrast-enhanced MRI. *J Clin Invest.* 2013;123(3):1299-309. doi: 10.1172/JCI67677. PubMed PMID: 23434588; PubMed Central PMCID: PMC3582150.
25. Khani M, Sass LR, Xing T, Keith Sharp M, Baledent O, Martin BA. Anthropomorphic Model of Intrathecal Cerebrospinal Fluid Dynamics Within the Spinal Subarachnoid Space: Spinal Cord Nerve Roots Increase Steady-Streaming. *J Biomech Eng.* 2018;140(8). doi: 10.1115/1.4040401. PubMed PMID: 30003260; PubMed Central PMCID: PMC6056198.
26. Oreskovic D, Klarica M. The formation of cerebrospinal fluid: Nearly a hundred years of interpretations and misinterpretations. *Brain Res Rev.* 2010;64(2):241-62. doi: 10.1016/j.brainresrev.2010.04.006. PubMed PMID: WOS:000282412900001.
27. Davson H, Segal MB. *Physiology of the CSF and blood-brain barriers*. Boca Raton: CRC Press; 1996. 822 pages p.
28. Cserr HF. Physiology of Choroid Plexus. *Physiol Rev.* 1971;51(2):273-&. PubMed PMID: WOS:A1971J087800002.
29. Cushing H. Studies on the Cerebro-Spinal Fluid : I. Introduction. *J Med Res.* 1914;31(1):1-19. PubMed PMID: 19972189; PubMed Central PMCID: PMC2094441.
30. Yamada S, Kelly E. Cerebrospinal Fluid Dynamics and the Pathophysiology of Hydrocephalus: New Concepts. *Semin Ultrasound Ct.* 2016;37(2):84-91. doi: 10.1053/j.sult.2016.01.001. PubMed PMID: WOS:000374615100003.
31. Milhorat TH, Hammock MK, Davis DA, Fenstermacher JD. Choroid-Plexus Papilloma .1. Proof of Cerebrospinal-Fluid Overproduction. *Childs Brain.* 1976;2(5):273-89. PubMed PMID: WOS:A1976CU39300001.
32. Milhorat TH. Choroid Plexus and Cerebrospinal Fluid Production. *Science.* 1969;166(3912):1514-&. doi: DOI 10.1126/science.166.3912.1514. PubMed PMID: WOS:A1969E871300022.
33. Milhorat TH, Hammock MK, Chien T, Davis DA. Normal Rate of Cerebrospinal-Fluid Formation 5 Years after Bilateral Choroid Plexectomy - Case-Report. *Journal of Neurosurgery.* 1976;44(6):735-9. doi: DOI 10.3171/jns.1976.44.6.0735. PubMed PMID: WOS:A1976BS17600011.
34. Bulat M, Klarica M. Recent insights into a new hydrodynamics of the cerebrospinal fluid. *Brain Res Rev.* 2011;65(2):99-112. doi: 10.1016/j.brainresrev.2010.08.002. PubMed PMID: WOS:000286850100001.
35. Martin BA, Pahlavian SH. *Anatomy and Physiology of Cerebrospinal Fluid Dynamics. Nervous System Drug Delivery*: Elsevier; 2019. p. 73-89.

36. Henry-Feugeas MC, Idy-Peretti I, Baledent O, Poncelet-Didon A, Zannoli G, Bittoun J, et al. Origin of subarachnoid cerebrospinal fluid pulsations: a phase-contrast MR analysis. *Magnetic Resonance Imaging*. 2000;18(4):387-95. doi: Doi 10.1016/S0730-725x(99)00142-3. PubMed PMID: WOS:000086611400004.
37. Avezaat CJJ, Vaneijndhoven JHM, Wyper DJ. Cerebrospinal-Fluid Pulse Pressure and Intracranial Volume-Pressure Relationships. *J Neurol Neurosur Ps*. 1979;42(8):687-700. doi: DOI 10.1136/jnnp.42.8.687. PubMed PMID: WOS:A1979HH68600002.
38. Portnoy HD, Chopp M. Cerebrospinal-Fluid Pulse-Wave Form Analysis during Hypercapnia and Hypoxia. *Neurosurgery*. 1981;9(1):14-27. doi: Doi 10.1227/00006123-198107000-00004. PubMed PMID: WOS:A1981MB19400004.
39. Williams B. Simultaneous cerebral and spinal fluid pressure recordings. I. Technique, physiology, and normal results. *Acta Neurochir (Wien)*. 1981;58(3-4):167-85. PubMed PMID: 7315549.
40. Papisov MI, Belov VV, Gannon KS. Physiology of the intrathecal bolus: the leptomeningeal route for macromolecule and particle delivery to CNS. *Mol Pharm*. 2013;10(5):1522-32. doi: 10.1021/mp300474m. PubMed PMID: 23316936; PubMed Central PMCID: PMC3646927.
41. Hocking G, Wildsmith JAW. Intrathecal drug spread. *Brit J Anaesth*. 2004;93(4):568-78. doi: 10.1093/bja/aeh204. PubMed PMID: WOS:000223939300014.
42. Miracle AC, Fox MA, Ayyangar RN, Vyas A, Mukherji SK, Quint DJ. Imaging Evaluation of Intrathecal Baclofen Pump-Catheter Systems. *American Journal of Neuroradiology*. 2011;32(7):1158-64. doi: 10.3174/ajnr.A2211. PubMed PMID: WOS:000294275100002.
43. Heidari Pahlavian S, Bunck AC, Thyagaraj S, Giese D, Loth F, Hedderich DM, et al. Accuracy of 4D Flow Measurement of Cerebrospinal Fluid Dynamics in the Cervical Spine: An In Vitro Verification Against Numerical Simulation. *Ann Biomed Eng*. 2016;44(11):3202-14. Epub 2016/11/04. doi: 10.1007/s10439-016-1602-x. PubMed PMID: 27043214; PubMed Central PMCID: PMC5050060.
44. Yildiz S, Thyagaraj S, Jin N, Zhong XD, Pahlavian SH, Martin BA, et al. Quantifying the influence of respiration and cardiac pulsations on cerebrospinal fluid dynamics using real-time phase-contrast MRI. *J Magn Reson Imaging*. 2017;46(2):431-9. doi: 10.1002/jmri.25591. PubMed PMID: WOS:000405638200011.
45. Martin BA, Kalata W, Loth F, Royston TJ, Oshinski JN. Syringomyelia hydrodynamics: An in vitro study based on in vivo measurements. *J Biomech Eng-T Asme*. 2005;127(7):1110-20. doi: Doi 10.1115/1.2073687. PubMed PMID: ISI:000234259600008.
46. Martin BA, Loth F. The influence of coughing on cerebrospinal fluid pressure in an in vitro syringomyelia model with spinal subarachnoid space stenosis. *Cerebrospinal Fluid Res*. 2009;6:17. doi: 10.1186/1743-8454-6-17. PubMed PMID: 20043856; PubMed Central PMCID: PMC2806373.
47. Martin BA, Labuda R, Royston TJ, Oshinski JN, Iskandar B, Loth F. Spinal subarachnoid space pressure measurements in an in vitro spinal stenosis model: implications on syringomyelia theories. *J Biomech Eng*. 2010;132(11):111007. doi: 10.1115/1.4000089. PubMed PMID: 21034148.
48. <http://www.minnetronix.com/>.
49. Van Rompay KKA. Evaluation of antiretrovirals in animal models of HIV infection. *Antiviral Research*. 2010;85(1):159-75. doi: 10.1016/j.antiviral.2009.07.008.
50. Uno Y, Uehara S, Kohara S, Murayama N, Yamazaki H. Polymorphisms of CYP2D17 in cynomolgus and rhesus macaques: An evidence of the genetic basis for the variability of CYP2D-dependent drug metabolism. *Drug Metabolism and Disposition*. 2014;42(9):1407-10. doi: 10.1124/dmd.114.059220.
51. Jose DA, Luciano P, Vicente V, Juan Marcos AS, Gustavo F-C. Role of Catheter's Position for Final Results in Intrathecal Drug Delivery. Analysis Based on CSF Dynamics and Specific Drugs Profiles. *The Korean journal of pain*. 2013;26(4):336. doi: 10.3344/kjp.2013.26.4.336.

52. Flack SH, Bernardis CM. Cerebrospinal fluid and spinal cord distribution of hyperbaric bupivacaine and baclofen during slow intrathecal infusion in pigs. *Anesthesiology*. 2010;112(1):165. doi: 10.1097/ALN.0b013e3181c38da5.
53. Khani M, Lawrence BJ, Sass LR, Gibbs CP, Fluid JJ, Oshinski JN, et al. Characterization of intrathecal cerebrospinal fluid geometry and dynamics in cynomolgus monkeys (*macaca fascicularis*) by magnetic resonance imaging.(Research Article)(Report). *PLoS ONE*. 2019;14(2):e0212239. doi: 10.1371/journal.pone.0212239.
54. Simoens S, Huys I. Market access of Spinraza (Nusinersen) for spinal muscular atrophy: intellectual property rights, pricing, value and coverage considerations. *Gene Ther*. 2017;24(9):539-41. Epub 2017/09/08. doi: 10.1038/gt.2017.79. PubMed PMID: 28880019.
55. Simpson K, Baranidharan G, Gupta S. *Spinal Interventions in Pain Management*: OUP Oxford; 2012.
56. Papisov MI, Belov VV, Gannon KS. Physiology of the Intrathecal Bolus: The Leptomeningeal Route for Macromolecule and Particle Delivery to CNS. *Mol Pharm*. 2013. Epub 2013/01/16. doi: 10.1021/mp300474m. PubMed PMID: 23316936.
57. Xie L, Kang H, Xu Q, Chen MJ, Liao Y, Thiagarajan M, et al. Sleep drives metabolite clearance from the adult brain. *Science*. 2013;342(6156):373-7. Epub 2013/10/19. doi: 10.1126/science.1241224. PubMed PMID: 24136970; PubMed Central PMCID: PMC3880190.
58. Weller RO, Djuanda E, Yow HY, Carare RO. Lymphatic drainage of the brain and the pathophysiology of neurological disease. *Acta Neuropathol*. 2009;117(1):1-14. Epub 2008/11/13. doi: 10.1007/s00401-008-0457-0. PubMed PMID: 19002474.
59. Martin BA, Kalata W, Shaffer N, Fischer P, Luciano M, Loth F. Hydrodynamic and Longitudinal Impedance Analysis of Cerebrospinal Fluid Dynamics at the Craniovertebral Junction in Type I Chiari Malformation. *Plos One*. 2013;8(10):e75335. doi: ARTN e75335 10.1371/journal.pone.0075335. PubMed PMID: WOS:000325814200011.
60. Martin BA, Yiallourou TI, Pahlavian SH, Thyagaraj S, Bunck AC, Loth F, et al. Inter-operator Reliability of Magnetic Resonance Image-Based Computational Fluid Dynamics Prediction of Cerebrospinal Fluid Motion in the Cervical Spine. *Annals of Biomedical Engineering*. 2016;Accepted.
61. Yiallourou T, Schmid Daners M, Kurtcuoglu V, Haba-Rubio J, Heinzer R, Fornari E, et al. Continuous positive airway pressure alters cranial blood flow and cerebrospinal fluid dynamics at the craniovertebral junction. *Interdisciplinary Neurosurgery: Advanced Techniques and Case Management*. 2015;2:152-9.
62. Gupta A, Church D, Barnes D, Hassan A. Cut to the chase: on the need for genotype-specific soft tissue sarcoma trials. *Annals of oncology*. 2009;20(3):399-400.
63. Gupta S, Soellinger M, Grzybowski DM, Boesiger P, Biddiscombe J, Poulikakos D, et al. Cerebrospinal fluid dynamics in the human cranial subarachnoid space: an overlooked mediator of cerebral disease. I. Computational model. *Journal of the Royal Society Interface*. 2010;7(49):1195-204.
64. Loth F, Yardimci MA, Alperin N. Hydrodynamic modeling of cerebrospinal fluid motion within the spinal cavity. *J Biomech Eng*. 2001;123(1):71-9. PubMed PMID: 11277305.
65. San O, Staples AE. An Improved Model for Reduced-Order Physiological Fluid Flows. *J Mech Med Biol*. 2012;12(3). doi: ArtN 1250052 10.1142/S0219519411004666. PubMed PMID: WOS:000310083500020.
66. Kalata W, Martin BA, Oshinski JN, Jerosch-Herold M, Royston TJ, Loth F. MR Measurement of Cerebrospinal Fluid Velocity Wave Speed in the Spinal Canal. *IEEE Trans Biomed Eng*. 2009. Epub 2009/01/29. doi: 10.1109/TBME.2008.2011647. PubMed PMID: 19174343.
67. Tangen KM, Hsu Y, Zhu DC, Linninger AA. CNS wide simulation of flow resistance and drug transport due to spinal microanatomy. *J Biomech*. 2015;48(10):2144-54. doi: 10.1016/j.jbiomech.2015.02.018. PubMed PMID: 25888012.

68. Kuttler A, Dimke T, Kern S, Helmlinger G, Stanski D, Finelli LA. Understanding pharmacokinetics using realistic computational models of fluid dynamics: biosimulation of drug distribution within the CSF space for intrathecal drugs. *Journal of pharmacokinetics and pharmacodynamics*. 2010;37(6):629-44.
69. Bertram CD. Evaluation by fluid/structure-interaction spinal-cord simulation of the effects of subarachnoid-space stenosis on an adjacent syrinx. *J Biomech Eng*. 2010;132(6):061009. doi: 10.1115/1.4001165. PubMed PMID: 20887034.
70. Elliott NS. Syrinx fluid transport: modeling pressure-wave-induced flux across the spinal pial membrane. *J Biomech Eng*. 2012;134(3):031006. Epub 2012/04/10. doi: 10.1115/1.4005849. PubMed PMID: 22482686.
71. Cirovic S, Kim M. A one-dimensional model of the spinal cerebrospinal-fluid compartment. *J Biomech Eng*. 2012;134(2):021005. doi: 10.1115/1.4005853. PubMed PMID: 22482672.
72. Lockey P, Poots G, Williams B. Theoretical aspects of the attenuation of pressure pulses within cerebrospinal-fluid pathways. *Med Biol Eng*. 1975;13(6):861-9. PubMed PMID: 1195879.
73. Yiallourou TI, Kroger JR, Stergiopoulos N, Maintz D, Martin BA, Bunck AC. Comparison of 4D phase-contrast MRI flow measurements to computational fluid dynamics simulations of cerebrospinal fluid motion in the cervical spine. *PLoS One*. 2012;7(12):e52284. doi: 10.1371/journal.pone.0052284. PubMed PMID: 23284970; PubMed Central PMCID: PMC3528759.
74. Heidari Pahlavian S, Bunck AC, Loth F, Shane Tubbs R, Yiallourou T, Kroeger JR, et al. Characterization of the discrepancies between four-dimensional phase-contrast magnetic resonance imaging and in-silico simulations of cerebrospinal fluid dynamics. *J Biomech Eng*. 2015;137(5):051002. doi: 10.1115/1.4029699. PubMed PMID: 25647090; PubMed Central PMCID: PMC3528759.
75. Pahlavian SH, Bunck AC, Thyagaraj S, Giese D, Loth F, Hedderich DM, et al. Accuracy of 4D Flow measurement of cerebrospinal fluid dynamics in the cervical spine: An in vitro verification against numerical simulation. *Ann Biomed Eng*. 2016;In Press.
76. Heidari Pahlavian S, Yiallourou T, Tubbs RS, Bunck AC, Loth F, Goodin M, et al. The impact of spinal cord nerve roots and denticulate ligaments on cerebrospinal fluid dynamics in the cervical spine. *Plos One*. 2014;9(4):e91888. doi: 10.1371/journal.pone.0091888. PubMed PMID: 24710111; PubMed Central PMCID: PMC3977950.
77. Sigmund EE, Suero GA, Hu C, McGorty K, Sodickson DK, Wiggins GC, et al. High-resolution human cervical spinal cord imaging at 7 T. *NMR Biomed*. 2012;25(7):891-9. Epub 2011/12/21. doi: 10.1002/nbm.1809. PubMed PMID: 22183956; PubMed Central PMCID: PMC3377161.
78. Helgeland A, Mardal KA, Haughton V, Reif BA. Numerical simulations of the pulsating flow of cerebrospinal fluid flow in the cervical spinal canal of a Chiari patient. *J Biomech*. 2014;47(5):1082-90. doi: 10.1016/j.jbiomech.2013.12.023. PubMed PMID: 24529910.
79. Sweetman B, Linninger AA. Cerebrospinal fluid flow dynamics in the central nervous system. *Ann Biomed Eng*. 2011;39(1):484-96. doi: 10.1007/s10439-010-0141-0. PubMed PMID: 20737291.
80. Martin BA, Reymond P, Novy J, Baledent O, Stergiopoulos N. A coupled hydrodynamic model of the cardiovascular and cerebrospinal fluid system. *Am J Physiol Heart Circ Physiol*. 2012;302(7):H1492-509. doi: 10.1152/ajpheart.00658.2011. PubMed PMID: 22268106.
81. Elliott NSJ, Bertram CD, Martin BA, Brodbelt AR. Syringomyelia: A review of the biomechanics. *Journal of Fluids and Structures*. 2013;40:1-24. doi: Doi 10.1016/J.jfluidstructs.2013.01.010. PubMed PMID: ISI:000322050600001.
82. Lawrence BJ, Luciano M, Tew J, Ellenbogen RG, Oshinski JN, Loth F, et al. Cardiac-Related Spinal Cord Tissue Motion at the Foramen Magnum is Increased in Patients with Type I Chiari Malformation and Decreases Postdecompression Surgery. *World Neurosurg*. 2018;116:e298-e307.

Epub 2018/05/08. doi: 10.1016/j.wneu.2018.04.191. PubMed PMID: 29733988; PubMed Central PMCID: PMC6063776.

83. Bert RJ, Hayek SM, Yaksh TL. Modeling Spinal Intrathecal Drug Distribution: The Challenge of Defining and Predicting Cerebrospinal Fluid Dynamics. *Anesth Analg*. 2017;124(5):1403-6. doi: 10.1213/ANE.0000000000002071. PubMed PMID: 28426585.

84. Brinker T, Stopa E, Morrison J, Klinge PJF, *CNS Bot*. A new look at cerebrospinal fluid circulation. 2014;11(1):10. doi: 10.1186/2045-8118-11-10.

85. Enzmann DR, Pelc NJ. Normal flow patterns of intracranial and spinal cerebrospinal fluid defined with phase-contrast cine MR imaging. *Radiology*. 1991;178(2):467-74. Epub 1991/02/01. doi: 10.1148/radiology.178.2.1987610. PubMed PMID: 1987610.

86. Schroth G, Klose U. Cerebrospinal-Fluid Flow .2. Physiology of Respiration-Related Pulsations. *Neuroradiology*. 1992;35(1):10-5. doi: Doi 10.1007/Bf00588271. PubMed PMID: WOS:A1992KB91100002.

87. Wostyn P, Audenaert K, De Deyn PP. More advanced Alzheimer's disease may be associated with a decrease in cerebrospinal fluid pressure. *Cerebrospinal Fluid Res*. 2009;6:14. doi: 10.1186/1743-8454-6-14. PubMed PMID: 19917128; PubMed Central PMCID: PMC2780980.

88. Bunck AC, Kroeger JR, Juettner A, Brentrup A, Fiedler B, Crelier GR, et al. Magnetic resonance 4D flow analysis of cerebrospinal fluid dynamics in Chiari I malformation with and without syringomyelia. *Eur Radiol*. 2012;22(9):1860-70. doi: 10.1007/s00330-012-2457-7. PubMed PMID: 22569996.

89. Bradley WG, Jr., Kortman KE, Burgoyne B. Flowing cerebrospinal fluid in normal and hydrocephalic states: appearance on MR images. *Radiology*. 1986;159(3):611-6. Epub 1986/06/01. PubMed PMID: 3704142.

90. Pizzichelli G, Kehlet B, Evju O, Martin BA, Rognes ME, Mardal KA, et al. Numerical study of intrathecal drug delivery to a permeable spinal cord: effect of catheter position and angle. *Comput Methods Biomech Biomed Engin*. 2017:1-10. doi: 10.1080/10255842.2017.1393805. PubMed PMID: 29119834.

91. Khani M, Xing T, Gibbs C, Oshinski JN, Stewart GR, Zeller JR, et al. Nonuniform Moving Boundary Method for Computational Fluid Dynamics Simulation of Intrathecal Cerebrospinal Flow Distribution in a Cynomolgus Monkey. *J Biomech Eng*. 2017;139(8). doi: 10.1115/1.4036608. PubMed PMID: 28462417; PubMed Central PMCID: PMC5467026.

92. Khani M, Sass L, Xing T, Sharp MK, Balédent O, Martin B. Anthropomorphic Model of Intrathecal Cerebrospinal Fluid Dynamics Within the Spinal Subarachnoid Space: Spinal Cord Nerve Roots Increase Steady-Streaming. *Journal of Biomechanical Engineering*. 2018. doi: 10.1115/1.4040401.

93. Tangen KM, Leval R, Mehta AI, Linninger AA. Computational and in vitro experimental investigation of intrathecal drug distribution: parametric study of the effect of injection volume, cerebrospinal fluid pulsatility, and drug uptake. *Anesthesia & Analgesia*. 2017;124(5):1686-96.

94. Greitz D, Hannerz J. A proposed model of cerebrospinal fluid circulation: Observations with radionuclide cisternography. *American Journal of Neuroradiology*. 1996;17(3):431-8. PubMed PMID: WOS:A1996UB13900007.

95. Puy V, Zmudka-Attier J, Capel C, Bouzerar R, Serot JM, Bourgeois AM, et al. Interactions between Flow Oscillations and Biochemical Parameters in the Cerebrospinal Fluid. *Front Aging Neurosci*. 2016;8. doi: ARTN 154

10.3389/fnagi.2016.00154. PubMed PMID: WOS:000378674100001.

96. O'Donnell J, Ding F, Nedergaard M. Distinct functional states of astrocytes during sleep and wakefulness: Is norepinephrine the master regulator? *Curr Sleep Med Rep*. 2015;1(1):1-8. doi: 10.1007/s40675-014-0004-6. PubMed PMID: 26618103; PubMed Central PMCID: PMC6063776.

97. Patel T, Zhou J, Piepmeier JM, Saltzman WM. Polymeric nanoparticles for drug delivery to the central nervous system. *Adv Drug Deliv Rev.* 2012;64(7):701-5. Epub 2012/01/03. doi: 10.1016/j.addr.2011.12.006. PubMed PMID: 22210134; PubMed Central PMCID: PMC3323692.
98. Lu CT, Zhao YZ, Wong HL, Cai J, Peng L, Tian XQ. Current approaches to enhance CNS delivery of drugs across the brain barriers. *Int J Nanomedicine.* 2014;9:2241-57. Epub 2014/05/30. doi: 10.2147/IJN.S61288. PubMed PMID: 24872687; PubMed Central PMCID: PMC34026551.
99. Watanabe Y, Kazuki Y, Kazuki K, Ebiki M, Nakanishi M, Nakamura K, et al. Use of a Human Artificial Chromosome for Delivering Trophic Factors in a Rodent Model of Amyotrophic Lateral Sclerosis. *Mol Ther Nucleic Acids.* 2015;4:e253. doi: 10.1038/mtna.2015.28. PubMed PMID: 26440597.
100. Deepa P, Shahani N, Alladi PA, Vijayalakshmi K, Sathyaprabha TN, Nalini A, et al. Down regulation of trophic factors in neonatal rat spinal cord after administration of cerebrospinal fluid from sporadic amyotrophic lateral sclerosis patients. *J Neural Transm (Vienna).* 2011;118(4):531-8. doi: 10.1007/s00702-010-0520-6. PubMed PMID: 21069391.
101. Chen BK, Staff NP, Knight AM, Nesbitt JJ, Butler GW, Padley DJ, et al. A safety study on intrathecal delivery of autologous mesenchymal stromal cells in rabbits directly supporting Phase I human trials. *Transfusion.* 2015;55(5):1013-20. doi: 10.1111/trf.12938. PubMed PMID: 25413276; PubMed Central PMCID: PMC34428970.
102. Katz N, Goode T, Hinderer C, Hordeaux J, Wilson JM. Standardized method for intra-cisterna magna delivery under fluoroscopic guidance in nonhuman primates. *Hum Gene Ther Methods.* 2018. Epub 2018/07/24. doi: 10.1089/hgtb.2018.041. PubMed PMID: 30032644.
103. Miller TM, Pestronk A, David W, Rothstein J, Simpson E, Appel SH, et al. An antisense oligonucleotide against SOD1 delivered intrathecally for patients with SOD1 familial amyotrophic lateral sclerosis: a phase 1, randomised, first-in-man study. *Lancet Neurol.* 2013;12(5):435-42. Epub 2013/04/02. doi: 10.1016/S1474-4422(13)70061-9. PubMed PMID: 23541756; PubMed Central PMCID: PMC3712285.
104. Ordia JI, Fischer E, Adamski E, Spatz EL. Chronic intrathecal delivery of baclofen by a programmable pump for the treatment of severe spasticity. *J Neurosurg.* 1996;85(3):452-7. Epub 1996/09/01. doi: 10.3171/jns.1996.85.3.0452. PubMed PMID: 8751632.
105. Claborn MK, Stevens DL, Walker CK, Gildon BL. Nusinersen: A Treatment for Spinal Muscular Atrophy. *Ann Pharmacother.* 2018;1060028018789956. Epub 2018/07/17. doi: 10.1177/1060028018789956. PubMed PMID: 30008228.
106. Yushkevich PA, Piven J, Hazlett HC, Smith RG, Ho S, Gee JC, et al. User-guided 3D active contour segmentation of anatomical structures: significantly improved efficiency and reliability. *Neuroimage.* 2006;31(3):1116-28. doi: 10.1016/j.neuroimage.2006.01.015. PubMed PMID: 16545965.
107. Martin BA, Yiallourou TI, Pahlavian SH, Thyagaraj S, Bunck AC, Loth F, et al. Inter-operator Reliability of Magnetic Resonance Image-Based Computational Fluid Dynamics Prediction of Cerebrospinal Fluid Motion in the Cervical Spine. *Ann Biomed Eng.* 2016;44(5):1524-37. doi: 10.1007/s10439-015-1449-6. PubMed PMID: 26446009; PubMed Central PMCID: PMC34824672.
108. Jain K, Ringstad G, Eide PK, Mardal KA. Direct numerical simulation of transitional hydrodynamics of the cerebrospinal fluid in Chiari I malformation: The role of cranio-vertebral junction. *International Journal for Numerical Methods in Biomedical Engineering.* 2017;33(9). doi: ARTN e2853. PubMed PMID: WOS:000409217800007.
109. Khani M, Sass LR, Xing T, Keith Sharp M, Balédent O, Martin BA. Anthropomorphic Model of Intrathecal Cerebrospinal Fluid Dynamics Within the Spinal Subarachnoid Space: Spinal Cord Nerve Roots Increase Steady-Streaming. *Journal of Biomechanical Engineering.* 2018;140(8):081012--15. doi: 10.1115/1.4040401.

110. Cirovic S, Lloyd R, Jovanovik J, Volk HA, Rusbridge C. Computer simulation of syringomyelia in dogs. *BMC Vet Res.* 2018;14(1):82. doi: 10.1186/s12917-018-1410-7. PubMed PMID: 29523203; PubMed Central PMCID: PMC5845370.
111. Vardoulis O, Coppens E, Martin BA, Reymond P, Tozzi P, Stergiopoulos N. Impact of Aortic Grafts on Arterial Pressure: A Computational Fluid Dynamics Study. *European Journal of Vascular and Endovascular Surgery.* 2011;42(5):704-10. doi: 10.1016/J.Ejvs.2011.08.006. PubMed PMID: ISI:000297238900026.
112. Reymond P, Perren F, Lazeyras F, Stergiopoulos N. Patient-specific mean pressure drop in the systemic arterial tree, a comparison between 1-D and 3-D models. *J Biomech.* 2012;45(15):2499-505. doi: 10.1016/j.jbiomech.2012.07.020. PubMed PMID: 22884968.
113. Bilston LE, Stoodley MA, Fletcher DF. The influence of the relative timing of arterial and subarachnoid space pulse waves on spinal perivascular cerebrospinal fluid flow as a possible factor in syrinx development. *J Neurosurg.* 2010;112(4):808-13. Epub 2009/06/16. doi: 10.3171/2009.5.JNS08945. PubMed PMID: 19522574.
114. Hemley SJ, Bilston LE, Cheng S, Chan JN, Stoodley MA. Aquaporin-4 expression in post-traumatic syringomyelia. *J Neurotrauma.* 2013;30(16):1457-67. Epub 2013/02/28. doi: 10.1089/neu.2012.2614. PubMed PMID: 23441695; PubMed Central PMCID: PMC3741421.
115. Yeo J, Cheng S, Hemley S, Lee BB, Stoodley M, Bilston L. Characteristics of CSF Velocity-Time Profile in Posttraumatic Syringomyelia. *AJNR Am J Neuroradiol.* 2017. doi: 10.3174/ajnr.A5304. PubMed PMID: 28729294.
116. Gray SJ, Nagabhushan Kalburgi S, McCown TJ, Jude Samulski R. Global CNS gene delivery and evasion of anti-AAV-neutralizing antibodies by intrathecal AAV administration in non-human primates. *Gene Ther.* 2013;20(4):450-9. Epub 2013/01/11. doi: 10.1038/gt.2012.101. PubMed PMID: 23303281; PubMed Central PMCID: PMC3618620.
117. Hall JE, Guyton AC. *Guyton and Hall textbook of medical physiology.* 12th ed. Philadelphia, Pa.: Saunders/Elsevier; 2011. xix, 1091 p. p.
118. Sass LR, Khani M, Natividad GC, Tubbs RS, Baledent O, Martin BA. A 3D subject-specific model of the spinal subarachnoid space with anatomically realistic ventral and dorsal spinal cord nerve rootlets. *Fluids and Barriers of the CNS.* 2017;14(1):36. doi: 10.1186/s12987-017-0085-y.
119. Levi Chazen J, Dyke JP, Holt RW, Horky L, Pauplis RA, Hesterman JY, et al. Automated segmentation of MR imaging to determine normative central nervous system cerebrospinal fluid volumes in healthy volunteers. *Clin Imaging.* 2017;43:132-5. doi: 10.1016/j.clinimag.2017.02.007. PubMed PMID: 28314198.
120. Yildiz S, Thyagaraj S, Jin N, Zhong X, Heidari Pahlavian S, Martin BA, et al. Quantifying the influence of respiration and cardiac pulsations on cerebrospinal fluid dynamics using real-time phase-contrast MRI. *J Magn Reson Imaging.* 2017;46(2):431-9. doi: 10.1002/jmri.25591. PubMed PMID: 28152239.
121. Chen L, Beckett A, Verma A, Feinberg DA. Dynamics of respiratory and cardiac CSF motion revealed with real-time simultaneous multi-slice EPI velocity phase contrast imaging. *Neuroimage.* 2015;122:281-7. doi: 10.1016/j.neuroimage.2015.07.073. PubMed PMID: 26241682; PubMed Central PMCID: PMC4716739.
122. Baledent O, Henry-Feugeas MC, Idy-Peretti I. Cerebrospinal fluid dynamics and relation with blood flow: a magnetic resonance study with semiautomated cerebrospinal fluid segmentation. *Investigative radiology.* 2001;36(7):368-77. Epub 2001/08/10. PubMed PMID: 11496092.
123. Wostyn P, Audenaert K, De Deyn PP. More advanced Alzheimer's disease may be associated with a decrease in cerebrospinal fluid pressure. *Cerebrospinal fluid research.* 2009;6(1):1-4.
124. Takizawa K, Matsumae M, Hayashi N, Hirayama A, Yatsushiro S, Kuroda K. Hyperdynamic CSF motion profiles found in idiopathic normal pressure hydrocephalus and Alzheimer's disease assessed by fluid mechanics derived from magnetic resonance images. *Fluids Barriers Cns.*

2017;14(1):2-9. doi: 10.1186/s12987-017-0077-y. PubMed PMID: 29047355; PubMed Central PMCID: PMC5648475.

125. Yeo J, Cheng S, Hemley S, Lee BB, Stoodley M, Bilston L. Characteristics of CSF Velocity-Time Profile in Posttraumatic Syringomyelia. *AJNR American journal of neuroradiology*. 2017;38(9):1839-44. doi: 10.3174/ajnr.A5304. PubMed PMID: 28729294.

126. Zhang LF, Hargens AR. Intraocular/Intracranial Pressure Mismatch Hypothesis for Visual Impairment Syndrome in Space. *Aviat Space Envir Md*. 2014;85(1):78-80. doi: 10.3357/Asem.3789.2014. PubMed PMID: WOS:000332996900016.

127. Tangen K, Narasimhan NS, Sierzega K, Preden T, Alaraj A, Linninger AA. Clearance of Subarachnoid Hemorrhage from the Cerebrospinal Fluid in Computational and In Vitro Models. *Ann Biomed Eng*. 2016;44(12):3478-94. doi: 10.1007/s10439-016-1681-8. PubMed PMID: 27384938.

128. Khani M, Xing T, Gibbs C, Oshinski JN, Stewart GR, Zeller JR, et al. Nonuniform Moving Boundary Method for Computational Fluid Dynamics Simulation of Intrathecal Cerebrospinal Flow Distribution in a Cynomolgus Monkey. *J Biomech Eng*. 2017;139(8):081005. doi: 10.1115/1.4036608. PubMed PMID: 28462417; PubMed Central PMCID: PMC5467026.

129. Hsu Y, Harris TJ, Hettiarachchi HDM, Penn R, Linninger AA. Three Dimensional Simulation and Experimental Investigation of Intrathecal Drug Delivery in the Spinal Canal and the Brain. *Comput-Aided Chem En*. 2011;29:1525-9. PubMed PMID: WOS:000294218900305.

130. Hsu Y, Hettiarachchi HD, Zhu DC, Linninger AA. The frequency and magnitude of cerebrospinal fluid pulsations influence intrathecal drug distribution: key factors for interpatient variability. *Anesth Analg*. 2012;115(2):386-94. doi: 10.1213/ANE.0b013e3182536211. PubMed PMID: 22523420.

131. Cheng S, Fletcher D, Hemley S, Stoodley M, Bilston L. Effects of fluid structure interaction in a three dimensional model of the spinal subarachnoid space. *J Biomech*. 2014;47(11):2826-30. Epub 2014/07/10. doi: 10.1016/j.jbiomech.2014.04.027. PubMed PMID: 25005435.

132. Tangen KM, Leval R, Mehta AI, Linninger AA. Computational and In Vitro Experimental Investigation of Intrathecal Drug Distribution: Parametric Study of the Effect of Injection Volume, Cerebrospinal Fluid Pulsatility, and Drug Uptake. *Anesthesia and analgesia*. 2017;124(5):1686-96. doi: 10.1213/ANE.0000000000002011. PubMed PMID: 28431428.

133. Kuttler A, Dimke T, Kern S, Helmlinger G, Stanski D, Finelli LA. Understanding pharmacokinetics using realistic computational models of fluid dynamics: biosimulation of drug distribution within the CSF space for intrathecal drugs. *J Pharmacokinet Phar*. 2010;37(6):629-44. doi: 10.1007/s10928-010-9184-y. PubMed PMID: 21132572; PubMed Central PMCID: PMC3005107.

134. Pizzichelli G, Kehlet G, Evju Ø, Martin BA, Rognes ME, Mardal KA, et al. Numerical study of intrathecal drug delivery to a permeable spinal cord: effect of catheter position and angle. *Computer Methods in Biomechanics and Biomedical Engineering*. 2017;20(15):1599-608.

135. Haga PT, Pizzichelli G, Mortensen M, Kuchta M, Pahlavian SH, Sinibaldi E, et al. A numerical investigation of intrathecal isobaric drug dispersion within the cervical subarachnoid space. *Plos One*. 2017;12(3):e0173680. doi: 10.1371/journal.pone.0173680. PubMed PMID: 28296953; PubMed Central PMCID: PMC5351861.

136. Bertram CD, Brodbelt AR, Stoodley MA. The origins of syringomyelia: numerical models of fluid/structure interactions in the spinal cord. *J Biomech Eng*. 2005;127(7):1099-109. Epub 2006/03/01. PubMed PMID: 16502652.

137. Bertram C, Bilston L, Stoodley M. Tensile radial stress in the spinal cord related to arachnoiditis or tethering: a numerical model. *Medical & biological engineering & computing*. 2008;46(7):701-7.

138. Elliott NSJ, Lucey AD, Lockerby DA, Brodbelt AR. Fluid-structure interactions in a cylindrical layered wave guide with application in the spinal column to syringomyelia. *J Fluid Struct.* 2017;70:464-99. doi: 10.1016/j.jfluidstructs.2016.11.007. PubMed PMID: WOS:000399625700026.
139. Jain K, Ringstad G, Eide PK, Mardal KA. Direct numerical simulation of transitional hydrodynamics of the cerebrospinal fluid in Chiari I malformation: The role of cranio-vertebral junction. *Int J Numer Method Biomed Eng.* 2017;33(9). doi: 10.1002/cnm.2853. PubMed PMID: 27863152.
140. Cheng S, Stoodley MA, Wong J, Hemley S, Fletcher DF, Bilston LE. The presence of arachnoiditis affects the characteristics of CSF flow in the spinal subarachnoid space: a modelling study. *J Biomech.* 2012;45(7):1186-91. Epub 2012/03/06. doi: 10.1016/j.jbiomech.2012.01.050. PubMed PMID: 22386041.
141. Rutkowska G, Haughton V, Linge S, Mardal KA. Patient-specific 3D simulation of cyclic CSF flow at the craniocervical region. *AJNR American journal of neuroradiology.* 2012;33(9):1756-62. Epub 2012/04/21. doi: 10.3174/ajnr.A3047. PubMed PMID: 22517282.
142. Clarke EC, Stoodley MA, Bilston LE. Changes in temporal flow characteristics of CSF in Chiari malformation Type I with and without syringomyelia: implications for theory of syrinx development. *J Neurosurg.* 2013;118(5):1135-40. doi: 10.3171/2013.2.JNS12759. PubMed PMID: 23495878.
143. Shaffer N, Martin BA, Rocque B, Madura C, Wieben O, Iskandar BJ, et al. Cerebrospinal fluid flow impedance is elevated in Type I Chiari malformation. *J Biomech Eng.* 2014;136(2):021012. Epub 2013/12/24. doi: 10.1115/1.4026316. PubMed PMID: 24362680; PubMed Central PMCID: PMC4023655.
144. Roldan A, Wieben O, Haughton V, Osswald T, Chesler N. Characterization of CSF hydrodynamics in the presence and absence of tonsillar ectopia by means of computational flow analysis. *AJNR American journal of neuroradiology.* 2009;30(5):941-6. doi: 10.3174/ajnr.A1489. PubMed PMID: 19299486.
145. Linge SO, Mardal K-A, Helgeland A, Heiss JD, Haughton V. Effect of craniovertebral decompression on CSF dynamics in Chiari malformation type I studied with computational fluid dynamics: Laboratory investigation. *Journal of neurosurgery Spine.* 2014;21(4):559.
146. Linge SO, Haughton V, Lovgren AE, Mardal KA, Helgeland A, Langtangen HP. Effect of tonsillar herniation on cyclic CSF flow studied with computational flow analysis. *AJNR American journal of neuroradiology.* 2011;32(8):1474-81. Epub 2011/05/21. doi: 10.3174/ajnr.A2496. PubMed PMID: 21596806.
147. Linge S, Mardal K-A, Haughton V, Helgeland A. Simulating CSF flow dynamics in the normal and the Chiari I subarachnoid space during rest and exertion. *American Journal of Neuroradiology.* 2013;34(1):41-5.
148. Bilston LE, Fletcher DF, Stoodley MA. Focal spinal arachnoiditis increases subarachnoid space pressure: a computational study. *Clin Biomech (Bristol, Avon).* 2006;21(6):579-84. doi: 10.1016/j.clinbiomech.2006.01.009. PubMed PMID: 16530899.
149. Gupta S, Soellinger M, Grzybowski DM, Boesiger P, Biddiscombe J, Poulikakos D, et al. Cerebrospinal fluid dynamics in the human cranial subarachnoid space: an overlooked mediator of cerebral disease. I. Computational model. *J R Soc Interface.* 2010;7(49):1195-204. doi: 10.1098/rsif.2010.0033. PubMed PMID: 20236960; PubMed Central PMCID: PMC2894877.
150. Sass LR, Khani M, Natividad GC, Tubbs RS, Baledent O, Martin BA. A 3D subject-specific model of the spinal subarachnoid space with anatomically realistic ventral and dorsal spinal cord nerve rootlets. *Fluids Barriers CNS.* 2017;14(1):36. doi: 10.1186/s12987-017-0085-y. PubMed PMID: 29258534; PubMed Central PMCID: PMC45738087.
151. Xing T, Stern F. Factors of Safety for Richardson Extrapolation. *J Fluid Eng-T Asme.* 2010;132(6):061403. doi: Artn 061403-1

- 10.1115/1.4001771. PubMed PMID: WOS:000279117300012.
152. Xing T, Stern F. Closure to "Discussion of 'Factors of Safety for Richardson Extrapolation'" (2011, ASME J. Fluids Eng., 133, p. 115501). *J Fluid Eng-T Asme*. 2011;133(11):115502. doi: Artn 115502
Doi 10.1115/1.4005030. PubMed PMID: WOS:000297932200022.
153. Phillips TS, Roy CJ. Richardson extrapolation-based discretization uncertainty estimation for computational fluid dynamics. *Journal of Fluids Engineering*. 2014;136(12):121401.
154. Kurtcuoglu V, Soellinger M, Summers P, Poulikakos D, Boesiger P. Mixing and modes of mass transfer in the third cerebral ventricle: a computational analysis. *J Biomech Eng*. 2007;129(5):695-702. doi: 10.1115/1.2768376. PubMed PMID: 17887895.
155. Kurtcuoglu V, Soellinger M, Summers P, Boomsma K, Poulikakos D, Boesiger P, et al. Computational investigation of subject-specific cerebrospinal fluid flow in the third ventricle and aqueduct of Sylvius. *J Biomech*. 2007;40(6):1235-45. doi: 10.1016/j.jbiomech.2006.05.031. PubMed PMID: 16904117.
156. Wilson RV, Stern F, Coleman HW, Paterson EG. Comprehensive Approach to Verification and Validation of CFD Simulations—Part 2: Application for Rans Simulation of a Cargo/Container Ship. *Journal of Fluids Engineering*. 2001;123(4):803. doi: 10.1115/1.1412236.
157. Honji H. Streaked Flow around an Oscillating Circular-Cylinder. *J Fluid Mech*. 1981;107(Jun):509-20. doi: Doi 10.1017/S0022112081001894. PubMed PMID: WOS:A1981LY59100024.
158. Hall P. On the Stability of the Unsteady Boundary-Layer on a Cylinder Oscillating Transversely in a Viscous-Fluid. *J Fluid Mech*. 1984;146(Sep):347-67. doi: Doi 10.1017/S0022112084001907. PubMed PMID: WOS:A1984TP55600017.
159. Hino M, Sawamoto M, Takasu S. Experiments on Transition to Turbulence in an Oscillatory Pipe-Flow. *J Fluid Mech*. 1976;75(May27):193-207. doi: Doi 10.1017/S0022112076000177. PubMed PMID: WOS:A1976BZ28400001.
160. Sanchez AL, Martinez-Bazan C, Gutierrez-Montes C, Criado-Hidalgo E, Pawlak G, Bradley W, et al. On the bulk motion of the cerebrospinal fluid in the spinal canal. *Journal of Fluid Mechanics*. 2018;841:203-27. doi: 10.1017/jfm.2018.67. PubMed PMID: WOS:000428370900004.
161. Clarke EC, Fletcher DF, Stoodley MA, Bilston LE. Computational fluid dynamics modelling of cerebrospinal fluid pressure in Chiari malformation and syringomyelia. *J Biomech*. 2013;46(11):1801-9. Epub 2013/06/19. doi: 10.1016/j.jbiomech.2013.05.013. PubMed PMID: 23769174.
162. Linninger AA, Tsakiris C, Zhu DC, Xenos M, Roycewicz P, Danziger Z, et al. Pulsatile cerebrospinal fluid dynamics in the human brain. *IEEE transactions on bio-medical engineering*. 2005;52(4):557-65. doi: 10.1109/TBME.2005.844021. PubMed PMID: 15825857.
163. Greitz D. Cerebrospinal fluid circulation and associated intracranial dynamics. A radiologic investigation using MR imaging and radionuclide cisternography. *Acta Radiol Suppl*. 1993;386:1-23. PubMed PMID: 8517189.
164. Greitz D, Franck A, Nordell B. On the pulsatile nature of intracranial and spinal CSF-circulation demonstrated by MR imaging. *Acta Radiol*. 1993;34(4):321-8. PubMed PMID: 8318291.
165. Bunck AC, Kroger JR, Juttner A, Brentrup A, Fiedler B, Schaarschmidt F, et al. Magnetic resonance 4D flow characteristics of cerebrospinal fluid at the craniocervical junction and the cervical spinal canal. *Eur Radiol*. 2011;21(8):1788-96. doi: 10.1007/s00330-011-2105-7. PubMed PMID: 21404133.
166. Ahmed SA, Giddens DP. Pulsatile poststenotic flow studies with laser Doppler anemometry. *J Biomech*. 1984;17(9):695-705. PubMed PMID: 6238968.
167. Valen-Sendstad K, Steinman DA. Mind the gap: impact of computational fluid dynamics solution strategy on prediction of intracranial aneurysm hemodynamics and rupture status indicators.

- AJNR American journal of neuroradiology. 2014;35(3):536-43. doi: 10.3174/ajnr.A3793. PubMed PMID: 24231854.
168. Valen-Sendstad K, Mardal KA, Mortensen M, Reif BA, Langtangen HP. Direct numerical simulation of transitional flow in a patient-specific intracranial aneurysm. *J Biomech.* 2011;44(16):2826-32. doi: 10.1016/j.jbiomech.2011.08.015. PubMed PMID: 21924724.
169. Tagliabue A, Dede L, Quarteroni A. Complex blood flow patterns in an idealized left ventricle: A numerical study. *Chaos.* 2017;27(9):093939. doi: 10.1063/1.5002120. PubMed PMID: 28964151.
170. Jain K, Universität Siegen. universi - Universitätsverlag Siegen. Transition to turbulence in physiological flows: direct numerical simulation of hemodynamics in intracranial aneurysms and cerebrospinal fluid hydrodynamics in the spinal canal. 1st edition ed. Siegen: universi - Universitätsverlag Siegen; 2016. xx, 241 Seiten p.
171. An HW, Cheng LA, Zhao M. Direct numerical simulation of oscillatory flow around a circular cylinder at low Keulegan-Carpenter number. *J Fluid Mech.* 2011;666:77-103. doi: 10.1017/S0022112010003691. PubMed PMID: WOS:000287053100004.
172. Kin E, Sakajo T. Efficient topological chaos embedded in the blinking vortex system. *Chaos.* 2005;15(2):23111. doi: 10.1063/1.1923207. PubMed PMID: 16035887.
173. Aref H. The development of chaotic advection. *Phys Fluids.* 2002;14(4):1315-25. doi: 10.1063/1.1458932. PubMed PMID: WOS:000174319200005.
174. Daitche A, Tel T. Dynamics of blinking vortices. *Phys Rev E.* 2009;79(1 Pt 2):016210. doi: 10.1103/PhysRevE.79.016210. PubMed PMID: 19257125.
175. Lantigua H, Ortega-Gutierrez S, Schmidt JM, Lee K, Badjatia N, Agarwal S, et al. Subarachnoid hemorrhage: who dies, and why? *Critical Care.* 2015;19. doi: ARTN 309 10.1186/s13054-015-1036-0. PubMed PMID: WOS:000360334900001.
176. Lee KH, Lukovits T, Friedman JA. "Triple-H" therapy for cerebral vasospasm following subarachnoid hemorrhage. *Neurocrit Care.* 2006;4(1):68-76. doi: 10.1385/NCC:4:1:068. PubMed PMID: 16498198.
177. Bardutzky J, Witsch J, Juttler E, Schwab S, Vajkoczy P, Wolf S. EARLYDRAIN- outcome after early lumbar CSF-drainage in aneurysmal subarachnoid hemorrhage: study protocol for a randomized controlled trial. *Trials.* 2011;12. doi: Artn 203 10.1186/1745-6215-12-203. PubMed PMID: WOS:000295368400001.
178. Demirgil BT, Tugcu B, Postalci L, Guclu G, Dalgic A, Oral Z. Factors leading to hydrocephalus after aneurysmal subarachnoid hemorrhage. *Minimally Invasive Neurosurgery.* 2003;46(6):344-8. doi: 10.1055/s-2003-812500. PubMed PMID: WOS:000189387900007.
179. Graffradford NR, Torner J, Adams HP, Kassell NF. Factors Associated with Hydrocephalus after Subarachnoid Hemorrhage - a Report of the Cooperative Aneurysm Study. *Archives of Neurology.* 1989;46(7):744-52. doi: DOI 10.1001/archneur.1989.00520430038014. PubMed PMID: WOS:A1989AF66000012.
180. Hasan D, Vermeulen M, Wijdicks EFM, Hijdra A, Vangijn J. Management Problems in Acute Hydrocephalus after Subarachnoid Hemorrhage. *Stroke.* 1989;20(6):747-53. doi: Doi 10.1161/01.Str.20.6.747. PubMed PMID: WOS:A1989AB31000007.
181. Chen S, Luo JQ, Reis C, Manaenko A, Zhang JM. Hydrocephalus after Subarachnoid Hemorrhage: Pathophysiology, Diagnosis, and Treatment. *Biomed Research International.* 2017. doi: Artn 8584753 10.1155/2017/8584753. PubMed PMID: WOS:000398689500001.
182. Inagawa T, Kamiya K, Matsuda Y. Effect of Continuous Cisternal Drainage on Cerebral Vasospasm. *Acta Neurochir.* 1991;112(1-2):28-36. doi: Doi 10.1007/Bf01402451. PubMed PMID: WOS:A1991GP73800006.

183. Kawakami Y, Shimamura Y. Cisternal drainage after early operation of ruptured intracranial aneurysm. *Neurosurgery*. 1987;20(1):8-14. doi: Doi 10.1227/00006123-198701000-00003. PubMed PMID: 3808282.
184. Kodama N, Sasaki T, Kawakami M, Sato M, Asari J. Cisternal irrigation therapy with urokinase and ascorbic acid for prevention of vasospasm after aneurysmal subarachnoid hemorrhage outcome in 217 patients. *Surgical Neurology*. 2000;53(2):110-7. doi: Doi 10.1016/S0090-3019(99)00183-4. PubMed PMID: WOS:000085796300008.
185. Kodama N, Sasaki T, Yamanobe K, Sato M, Kawakami M. Prevention of Cerebral Vasospasm - Cisternal Irrigation Therapy with Urokinase and Ascorbic-Acid. *New Trends in Management of Cerebro-Vascular Malformations*. 1994:113-20. PubMed PMID: WOS:A1994BA77C00020.
186. Al-Tamimi YZ, Bhargava D, Feltbower RG, Hall G, Goddard AJP, Quinn AC, et al. Lumbar Drainage of Cerebrospinal Fluid After Aneurysmal Subarachnoid Hemorrhage A Prospective, Randomized, Controlled Trial (LUMAS). *Stroke*. 2012;43(3):677-+. doi: 10.1161/Strokeaha.111.625731. PubMed PMID: WOS:000300639400019.
187. Borkar SA. Spinal Cerebrospinal Fluid Drainage for Prevention of Vasospasm in Aneurysmal Subarachnoid Haemorrhage: A Prospective Randomized Controlled Study. *Neurosurgery*. 2013;60:180-1. doi: DOI 10.1227/01.neu.0000432773.35977.df. PubMed PMID: WOS:000330482600109.
188. Hoekema D, Schmidt RH, Ross I. Lumbar drainage for subarachnoid hemorrhage: technical considerations and safety analysis. *Neurocritical Care*. 2007;7(1):3-9. doi: 10.1007/s12028-007-0047-3. PubMed PMID: WOS:000248746800002.
189. Klimo P, Kestle JRW, MacDonald JD, Schmidt RH. Marked reduction of cerebral vasospasm with lumbar drainage of cerebrospinal fluid after subarachnoid hemorrhage. *Journal of Neurosurgery*. 2004;100(2):215-24. doi: DOI 10.3171/jns.2004.100.2.0215. PubMed PMID: WOS:000188551700006.
190. Kwon OY, Kim YJ, Kim YJ, Cho CS, Lee SK, Cho MK. The utility and benefits of external lumbar CSF drainage after endovascular coiling on aneurysmal subarachnoid hemorrhage. *Journal of Korean Neurosurgical Society*. 2008;43(6):281-7. doi: 10.3340/jkns.2008.43.6.281. PubMed PMID: WOS:000258240800005.
191. Maeda Y, Shirao S, Yoneda H, Ishihara H, Shinoyama M, Oka F, et al. Comparison of lumbar drainage and external ventricular drainage for clearance of subarachnoid clots after Guglielmi detachable coil embolization for aneurysmal subarachnoid hemorrhage. *Clinical Neurology and Neurosurgery*. 2013;115(7):965-70. doi: 10.1016/j.clineuro.2012.10.001. PubMed PMID: WOS:000321403000023.
192. Ormond DR, Dressler A, Kim S, Ronecker J, Murali R. Lumbar drains may reduce the need for permanent CSF diversion in spontaneous subarachnoid haemorrhage. *British Journal of Neurosurgery*. 2013;27(2):171-4. doi: 10.3109/02688697.2012.743971. PubMed PMID: WOS:000316954700007.
193. Park S, Yang N, Seo E. The effectiveness of lumbar cerebrospinal fluid drainage to reduce the cerebral vasospasm after surgical clipping for aneurysmal subarachnoid hemorrhage. *J Korean Neurosurg Soc*. 2015;57(3):167-73. doi: 10.3340/jkns.2015.57.3.167. PubMed PMID: 25810855; PubMed Central PMCID: PMC4373044.
194. Hirashima Y, Kurimoto M, Hayashi N, Umemura K, Hori E, Origasa H, et al. Duration of cerebrospinal fluid drainage in patients with aneurysmal subarachnoid hemorrhage for prevention of symptomatic vasospasm and late hydrocephalus. *Neurol Med-Chir*. 2005;45(4):177-82. doi: DOI 10.2176/nmc.45.177. PubMed PMID: WOS:000228441900001.
195. Kasuya H, Shimizu T, Kagawa M. The Effect of Continuous Drainage of Cerebrospinal-Fluid in Patients with Subarachnoid Hemorrhage - a Retrospective Analysis of 108 Patients. *Neurosurgery*.

- 1991;28(1):56-9. doi: Doi 10.1227/00006123-199101000-00009. PubMed PMID: WOS:A1991EP13700009.
196. Findlay JM, Kassell NF, Weir BKA, Haley EC, Kongable G, Germanson T, et al. A Randomized Trial of Intraoperative, Intracisternal Tissue-Plasminogen Activator for the Prevention of Vasospasm. *Neurosurgery*. 1995;37(1):168-76. doi: Doi 10.1227/00006123-199507000-00041. PubMed PMID: WOS:A1995RE54500085.
197. Kramer AH, Fletcher JJ. Locally-administered Intrathecal Thrombolytics Following Aneurysmal Subarachnoid Hemorrhage: A Systematic Review and Meta-analysis. *Neurocritical Care*. 2011;14(3):489-99. doi: 10.1007/s12028-010-9429-z. PubMed PMID: WOS:000290226800027.
198. Mizoi K, Yoshimoto T, Takahashi A, Fujiwara S, Kosu K, Sugawara T. Prospective-Study on the Prevention of Cerebral Vasospasm by Intrathecal Fibrinolytic Therapy with Tissue-Type Plasminogen-Activator. *Journal of Neurosurgery*. 1993;78(3):430-7. doi: DOI 10.3171/jns.1993.78.3.0430. PubMed PMID: WOS:A1993KN93600009.
199. Seifert V, Stolke D, Zimmermann M, Feldges A. Prevention of Delayed Ischemic Deficits after Aneurysmal Subarachnoid Hemorrhage by Intrathecal Bolus Injection of Tissue-Plasminogen Activator (Rtpa) - a Prospective-Study. *Acta Neurochirurgica*. 1994;128(1-4):137-43. doi: Doi 10.1007/Bf01400664. PubMed PMID: WOS:A1994NV07800020.
200. Hanggi D, Liersch J, Turowski B, Yong M, Steiger HJ. The effect of lumboventricular lavage and simultaneous low-frequency head-motion therapy after severe subarachnoid hemorrhage: results of a single center prospective Phase II trial. *Journal of Neurosurgery*. 2008;108(6):1192-9. doi: 10.3171/Jns/2008/108/6/1192. PubMed PMID: WOS:000256245300033.
201. Kawamoto S, Tsutsumi K, Yoshikawa G, Shinozaki MH, Yako K, Nagata K, et al. Effectiveness of the head-shaking method combined with cisternal irrigation with urokinase in preventing cerebral vasospasm after subarachnoid hemorrhage. *J Neurosurg*. 2004;100(2):236-43. doi: DOI 10.3171/jns.2004.100.2.0236. PubMed PMID: WOS:000188551700009.
202. Kertzscher U, Schneider T, Goubergrits L, Affeld K, Hanggi D, Spuler A. In Vitro Study of Cerebrospinal Fluid Dynamics in a Shaken Basal Cistern after Experimental Subarachnoid Hemorrhage. *Plos One*. 2012;7(8). doi: ARTN e41677
10.1371/journal.pone.0041677. PubMed PMID: WOS:000307212800030.
203. Blackburn SL, Swisher CB, Grande AW, Rubi A, Verbick LZ, McCabe A, et al. Novel Dual Lumen Catheter and Filtration Device for Removal of Subarachnoid hemorrhage: First Case Report. *Oper Neurosurg (Hagerstown)*. 2018. doi: 10.1093/ons/opy151. PubMed PMID: 29873785.
204. Extracorporeal Filtration of Subarachnoid Hemorrhage Via Spinal Catheter (PILLAR) 2018 [cited 2018 11/9/2018]. Available from: <https://clinicaltrials.gov/ct2/show/NCT02872636?term=pillar&cond=Subarachnoid+Hemorrhage&rank=1>.
205. Smilnak GJ, Charalambous LT, Cutshaw D, Premji AM, Giamberardino CD, Ballard CG, et al. Novel Treatment of Cryptococcal Meningitis via Neurapheresis Therapy. *J Infect Dis*. 2018;218(7):1147-54. doi: 10.1093/infdis/jiy286. PubMed PMID: 29788431; PubMed Central PMCID: PMC6107745.
206. Khani M, Lawrence BJ, Sass LR, Gibbs CP, Pluid JJ, Oshinski JN, et al. Characterization of intrathecal cerebrospinal fluid geometry and dynamics in cynomolgus monkeys (*macaca fascicularis*) by magnetic resonance imaging. *Plos One*. 2019;14(2):e0212239. doi: 10.1371/journal.pone.0212239. PubMed PMID: 30811449; PubMed Central PMCID: PMC6392269 following competing interests: This study was funded in part by Voyager Therapeutics. Author GRS is employed by Axovant and was employed by Voyager Therapeutics during the course of this study. JRZ is a fulltime employee of Northern Biomedical. BAM has received grant support from Voyager Therapeutics, Alcyone Lifesciences, Biogen, and Minnetronix Medical; BAM is a member of the Neurapheresis Research Consortium. BAM is scientific advisory board member for Alcyone Lifesciences and the Chiari and

Syringomyelia Foundation and served as a consultant to Voyager Therapeutics, SwanBio Therapeutics, Medtrac Biosystems, Neurosyntek, and Cerebral Therapeutics. There are no patents, products in development or marketed products to declare. This does not alter our adherence to all the PLOS ONE policies on sharing data and materials.

207. Bapuraj JR, Londy FJ, Delavari N, Maher CO, Garton HJL, Martin BA, et al. Cerebrospinal fluid velocity amplitudes within the cerebral aqueduct in healthy children and patients with Chiari I malformation. *J Magn Reson Imaging*. 2016;44(2):463-70. doi: 10.1002/jmri.25160. PubMed PMID: WOS:000380068100023.

208. Dolar MT, Haughton VM, Iskandar BJ, Quigley M. Effect of craniocervical decompression on peak CSF velocities in symptomatic patients with Chiari I malformation. *AJNR Am J Neuroradiol*. 2004;25(1):142-5. PubMed PMID: 14729545.

209. Quigley MF, Iskandar B, Quigley ME, Nicosia M, Haughton V. Cerebrospinal fluid flow in foramen magnum: temporal and spatial patterns at MR imaging in volunteers and in patients with Chiari I malformation. *Radiology*. 2004;232(1):229-36. doi: 10.1148/radiol.2321030666. PubMed PMID: 15155896.

210. Minnetronix. FILtration of Subarachnoid Hemorrhage Via Spinal CATHeteR Extension (PILLAR-XT). 2018.

211. Jain K, Ringstad G, Eide PK, Mardal KA. Direct numerical simulation of transitional hydrodynamics of the cerebrospinal fluid in Chiari I malformation: The role of cranio-vertebral junction. *Int J Numer Method Biomed Eng*. 2016;e2853:1-15. doi: 10.1002/cnm.2853. PubMed PMID: 27863152.

212. Dreha-Kulaczewski S, Joseph AA, Merboldt KD, Ludwig HC, Gartner J, Frahm J. Inspiration is the major regulator of human CSF flow. *J Neurosci*. 2015;35(6):2485-91. doi: 10.1523/JNEUROSCI.3246-14.2015. PubMed PMID: 25673843.

213. Takizawa K, Matsumae M, Sunohara S, Yatsushiro S, Kuroda K. Characterization of cardiac- and respiratory-driven cerebrospinal fluid motion based on asynchronous phase-contrast magnetic resonance imaging in volunteers. *Fluids Barriers CNS*. 2017;14(1):25. doi: 10.1186/s12987-017-0074-1. PubMed PMID: 28950883; PubMed Central PMCID: PMC5615451.